AN INVESTIGATION OF PROGRAMMABLE COMPLIANCE DURING ROBOT/ENVIRONMENT INTERACTIONS

DARRYL SCOTT PIKE

An Investigation of Programmable Compliance During Robot/Environment Interactions

by

© Darryl Scott Pike, B.ENG.

A THESIS SUBMITTED TO THE SCHOOL OF GRADUATE STUDIES IN PARTIAL FULFILMENT OF THE REQUIREMENTS FOR THE DEGREE OF MASTER OF ENGINEERING

Faculty of Engineering and Applied Science
Memorial University of Newfoundland
St. John's, Newfoundland

June 1994

ISBN 0-612-01902-0

This thesis is dedicated to
my grandfather
John G, Pike
whose youthful endeavours
inspired my persistence

Abstract

This thesis explores the effects of changing the effective damping and stiffness coefficients on the dynamic operating characteristics of a single degree of freedom direct-drive robot during "making" contact with a rigid environment. Altering these two coefficients ultimately implies changing the compliance of the robot/environment interaction. Since the compliance is changed dynamically and in real-time, the approach is referred to as *Active Compliance*. The thesis provides insight into the fundamental contact dynamics of a single robotic link such that the results can be used to describe the dynamics of more complex multi-degree of freedom manipulator architectures.

Active compliance requires real-time control of the damping and stiffness characteristics and is fundamentally a dynamic force control scheme allowing the robot to conform to the natural constraints imposed by the environment. To investigate this interaction in this thesis a software simulation program and a single degree of freedom direct-drive robot arm are developed. The thesis also clearly defines five distinct phases associated with the process of making contact. These contact phases are generic and apply to both mobile and fixed robots.

This study highlighted the following conclusions (1) Both mobile and fixed robots can benefit from controlled active compliance, (2) Altering these coefficients in real-time during the contact process is achievable, (3) The distance from the environment is not a necessary piece of information for contact under a force controlled contact scheme, (4) Compliance can be implemented based on a force constraint imposed upon the robot and the environment, (5) Sensors provide control information and must be strategically selected and mounted, (6) Ideal Damping and Stiffness laws are developed and proven functional, (7) Friction is a significant impedance factor which effects all aspects of the contact cycle.

Acknowledgement

This thesis was supported and made possible through a myriad of resources. Beyond personal motivation, my supervisors, Dr. Stuart Inkpen and Dr. Michael Hinchey, were instrumental in helping me achieve my objectives. Through financial support, enthusiasm and most importantly their clear innovative ideas, they both proved to be a prudent asset.

I also express my appreciation to Dr. Quaicoe, Dr. Moloney, Dr. Booton, Dr. Venkatesan and Dr. Dempster for their sincere interest in academic achievement. Their assistance during various stages of the software and hardware aspects of the direct-drive robot arm development were nothing less than milestones.

I also thank Lloyd Little for his assistance during the development of the real-time control program, the Keithley 575 interface software and also the printing of this thesis. Don Guy, Tom Pike and Dennis Johnson for their many trips to the electrical supply room and their endless stories about life. Richard Newman for the loan of all those power operational amplifiers - some of which were returned in a condition - well just returned. Tony Galway, David Press and Val Fortier of CAE for their patience during the production of this thesis. Derm Chafe and Dr. Bajzak for their help in obtaining the digital photographs of the Direct-Drive Robot Arm. Bruce Colbourne of I.M.D. for the use of the car batteries.

I don't believe I have left any technician resident of the S. J. Carew building unscarred by my presence. There are simply too many persons to mention. Thank you once again.

Table of Contents

List of Illustrations

List of Tables

Chapter 1

1.0 Introduction

Compliance has been one of the main topics of robotic research during the past decade. Investigating compliance has been important because mechanical structures, such as robots, inherently possess this attribute and more importantly there are benefits associated with adding controlled compliance to the robotic architecture. Daniel et al., 1985, pondered the question whether or not compliance was a "Bug or a Feature". They argue "it can be a virtue" and concluded the benefits of compliance far out-weigh the disadvantages and it is an important feature necessary for environment interaction: the essence of the robotic industry.

Industrial and special application robots are fundamentally designed to perform one particular task. All aspects of the robot's environment, work envelope, joint space singularities and load capabilities, to name a few, are incorporated into the initial hardware and software design. Even more attention is given to the end-effector of fixed and mobile robots. This dedication directly influences the cost of each robot and significantly reduces the ability of a particular robot to function effectively in

other task domains. This dedication is ultimately a limitation and it reflects the end-effector's degree of flexibility.

In terms of industrial robotic applications(fixed), there is a need to increase the flexibility of end-effector technology: the desirable level of flexibility of industrial robots has not been reached yet (Warnecke, 1985). Robots used in manufacturing are dedicated and thus designed to perform tasks of similar nature. The single most important and complex mechanism for this particular application is the end-effector. It represents the interface between the robot and work environment. The end-effector is a committed interface tool designed to grasp an object of specific identity. Clearly, a robotic manipulator capable of performing multiple operations in terms of grasping and handling objects of different shapes and material properties would significantly enhance its usefulness. This enhancement could be facilitated by incorporating programmable compliance into the end-effector architecture.

In terms of special application robots(mobile), such as those required for space and under water exploration, flexibility enhancement refers to the ability of the robot to explore uncharted areas without the need of human intervention - autonomous operation. This type of operation cannot be completely preprogrammed because the uncertainties inherent in the uncharted domains in which the robot will venture. A key aspect in realizing this type of operation lies in the ability of each appendage to independently cope with unstable irregular terrain. Compliance would facilitate this ability. Luk et al. (1991) state that a great benefit of compliant controlled robot appendages is that the robot can accommodate mechanical imperfections both in itself or on the surface it is contacting. In essence, legs provide an active suspension that decouples the path of the body from the path of the feet (Raibert, 1986). Programmable compliance will play a very important role in the development of this technology.

In summary, fine manipulators, both of articulated end-effectors and legged

systems, which are currently available are limited to the tasks they can perform (all papers). Increasing the flexibility of these manipulators would increase the performance and diversity of a particular robot and inherently reduce the cost associated with its operation. More specifically and importantly, this flexibility would allow the robot to couple its end-effector with the environment faster and in a more stable manner. One of the more significant methods of adding flexibility is by incorporating a method of implementing controllable compliance into the initial design stages of new manipulators and end-effectors.

1.1 Compliance

Compliance is the tendency or ability of a structure to translate, rotate or deform under the influence of applied forces. The term structure refers to robotic constituents, such as, links, joints and end-effectors, and actuators or could be used to reference the object which is to be manipulated. The forces applied to the robotic structures can be classified as either internal or external. Both forces will impart either purely translational motion, purely rotational motion or some combination.

1.1.1 Types of Compliance

In robotics, compliance is classified as either passive, semi-active or active. These compliant effects can be found to some degree on all robotic structures and/or applications and can be either intentional or unintentional. Unintentional compliance arises from the robot structure, for example, manipulator links bend under loads, belt slippage, motor shaft couples and gear slippage. Intentional compliance arises from the use of a physical device or software control strategies. This thesis is concerned

with intentional compliance. *Passive compliance* refers to the tendency of a structure to displace due to the effects of externally or internally applied forces. They are specifically designed for the application and the degree of compliance is preadjusted. A classical example of this type of device is Remote Centre Compliance(RCC) device. This device is mounted on the robot's wrist and allows the robot wrist to deform during the contact process. *Active compliance* refers to the *controlled* deformations of a structure in response to externally or internally induced forces. Sensors actively measure and facilitate error correction between the actual and desired response; position control and/or force control. The externally and internally induced forces are either torsional, translational or some combination. *Semi-active compliance* is a proportionate of the two extremes.

There are four axes of compliance: lateral, angular, axial and compressive. *Lateral compliance* is the ability or tendency of a member to move slightly from side to side while maintaining a parallel relationship with its initial position. *Angular compliance* is the ability or tendency of a member to pivot from side to side. This motion is similar to that associated with wrist action (YAW). *Axial compliance* is the ability or tendency of a member to roll (CW/CCW) under the influence of a torsional force. This is sometimes referred to as *Torsional compliance*. Finally, *Compressive compliance* is the ability or tendency of a member to move in and out under the influence of a translational force - spring motion.

1.1.2 Benefits of Compliance

Compliance, when used appropriately, can significantly enhance a robot's dynamic performance. Control, stability, environment interactions, bandwidth performance, advanced manipulation, are some of the areas which benefit from adding compliance. If a robot arm is highly compliant, impacts with the arm will

cause safe deformations (Daniel et al., 1985). This concept can be extended and conclude that a compliant arm will absorb the impact forces generated during object acquisition and reduce the possibility of damaging the object. Compliance can reduce or potentially eliminate the stability problems associated with non-collocated sensors and actuators (Akella et al., 1991; Yang and Mote, 1992; Cetinkunt and Wu, 1992). Delicate instrumentation will also benefit from the energy absorbing quality of compliance (Zheng and Fan, 1991).

1.1.3 Compliance Disadvantages

There are numerous drawbacks associated with adding compliance. Fundamentally, however, it is the time frame of implementing the compliance which becomes the main issue. One of the penalties of implementing compliance is that control inevitably becomes much more difficult, and unless special measures are taken, the positioning accuracy of the arm tip will deteriorate (Daniel et al., 1985). During non-contact position controlled tasks, compliance is not advantageous. Compliance reduces system bandwidth and when not used expediently gives rise to poorer dynamic performance (Akella et al., 1991; Whitney, 1987). Finally, energy is consumed by robot drive systems where its actuators are required to support the upper link masses and the payload (Asada and Youcef-Toumi, 1987).

1.1.4 Summary

Compliance is advantageous when strategically applied during certain task phases performed by both mobile and fixed robots. It is a means by which manipulators can increase their dynamic performance and it is the current trend in

manipulator design. A task which will benefit from programmable compliance is that of making and breaking contact with the environment and that of object manipulation. Optimally, compliance should only be activated under appropriate circumstances.

1.2 Research Objectives

The main objective of this study is to investigate and control the process of contact between a robot end-effector and the environment. The investigation will be carried out both numerically and through the development of a single degree of freedom direct-drive robot manipulator. The robot in both cases will interact with a rigid environment. In general terms:

> *Investigate the effects of changing the effective damping and spring coefficients on the dynamic operating characteristics of a single degree of freedom direct-drive robotic arm during making and breaking contact with a rigid environment.*

More specifically:

1) Develop a mathematical model to accurately represent a single degree of freedom direct-drive robotic arm.

2) Derive a numerical model from the mathematical model for software implementation and analysis.

3) Divide the process of making and breaking contact with the environment into strategic phases.

4) Develop an experimental model of the robotic arm.

5) Develop an algorithm to alter the effective stiffness and damping coefficients of the robot arm such as to facilitate the contact process:

   a) Minimize the time, t_{settle}, required to dissipate the kinetic

energies associated with contact, hence, minimize the settling time between the initial contact and the steady state displacement of the actuator tip.

b) Dissipate the kinetic energy subject to the physical constraints of the manipulator/actuator assembly(stroke).

c) Limit the force, F_{robot}, transmitted throughout the kinematic robotic chain.

d) Limit the force, F_{object}, transmitted to the object\environment being manipulated.

e) Keep contact between the robotic manipulator and the environment continuous (no bounce).

f) Dissipate the energy generated by impact and other environmental interactive disturbances adhering to constraints 1, 2, 3, 4 and 5.

g) Store impact energy for retrieval. This will be situation dependent, for example, during running gaits of future mobile robots.

h) The distance between the actuator and environment should not have to be known prior to impact.

6) The model design should be generic such that the results can be generalized to include both mobile and fixed robot structures.

Chapter 2

2.0 Previous Work

In the literature survey, several papers were identified as key reference material. Chapter 7.0 contains a listing of these principal papers. The following paragraphs highlight specific details from the cited papers pertinent to the thesis discussion. Also indicated are the positive and negative aspects of each article in terms of the presented thesis objectives.

It is well documented that Post-Contact requires some degree of compliance. Eppinger and Steering (1986) mathematically investigate post-contact stability of a robot model, coupled to the work environment through a compliant sensor, using proportional force control. Their analysis uses ideal linear lumped parameter models, both rigid and first vibrational modes to describe the robot and both rigid and compliant models to describe the environment. They conclude that when higher order robot dynamics are included in the model, contact with the environment, either rigid or compliant, under a force control regime is conditionally stable. This is because the feedback control loop is regulating the contact force through a dynamic robotic

system. Kazerooni et al. (1990) investigated the contact stability of a robot during constrained maneuvers. They verified both numerically and experimentally that the stability criteria (Small Gain Theorem and Nyquist Criterion) necessitate either some initial compliancy in the robot or in the environment. Changing the compliancy of the robot and/or the environment leads to a narrower, decrease in sensitivity, or wider, increase in sensitivity, stability range. The stability criterion also reveals that no compensator can be developed to stabilize the interaction between a very rigid robot and an infinitely rigid environment.

The transition between Pre-Contact and Post-Contact also requires some degree of compliance to exist either in the robot or environment. The dynamic forces generated during this transition (impact) can be highly impulsive with peaks large enough to damage an object if the contact velocity is sufficiently large (Parker and Paul, 1987). These impulsive forces are also transmitted through the kinematic chain of the robotic assembly and can damage it as well as the delicate sensors attached to the manipulator. Impact can be defined as, "any sudden, discontinuous, or aperiodic loading of a mechanical system (Burton, 1968, p109)".

The quantification and control of interactive impulsive forces generated by robots manipulating their environment have been the subject of several papers. Parker and Paul (1987) attempted to experimentally verify Johnson's (1958) equations which were developed for estimating impact forces. They conducted several impact tests between arious object materials (Rubber, Nylon and Brass) and fingertip materials (Polyurethane and Aluminum). The mass of the fingertip was 0.9kg and the object mass was 0.45kg and 7.7kg. With impact velocities maintained at approximately 1.225 m/sec, peak impact forces generated were on the order of 150N for the softer compliant combinations of the mentioned materials and approximately 2300N for the harder combinations. Using the greater mass for the object approximately doubled the peak impulse forces. They concluded that peak impact forces are a function of the following factors: fingertip mass and stiffness, object

mass and stiffness and finger impact velocity. Therefore, reducing either of these parameters alone or in some combination will reduce the forces generated upon contact. The key point here is that altering the stiffness coefficient of either the fingertip or environment will affect the magnitude of the force generated during impact.

During assembly operations one of the main problems preventing successful parts mating arises from resolution discrepancies between the robot and that required by the task, for example, peg in the hole type operations. Paul and Shimano (1976) investigated this problem. The positional tolerances of most parts mating tasks are on the order of thousandths of an inch, while manipulator resolutions are on the order of tenths of an inch. Increasing the positional accuracy of the manipulator is one solution to the problem. This will, however, require slow moving, heavy and extremely rigid robots which is not the current trend in the robotics industry. Another solution is to provide the manipulator with force sensors and allow it to comply with the natural constraints imposed by the task. In other words, add compliance into the manipulator architecture. Compliance will shadow positional inaccuracies and allow lower resolution manipulators to perform high resolution tasks.

It is clear from the above articles that compliance is essential during the transition from non-contact to contact, it is required during contact and is also beneficial during parts mating. Recent developments in the area of active and semi-active compliance are investigated in the following paragraphs.

Luk et al. (1991) designed an intelligent wall climbing robot: Robug II. It is an agile four legged mobile robot capable of vertical ascents. Manipulator actuation is pneumatic. Each articulated leg consists of two links and has three double acting pneumatic cylinders. Sensors provide joint angle measurements and force measurements. Each joint can be operated in two modes: position mode or compliant mode. The latter is of interest. When the robot legs are negotiating obstacles,

climbing or walking over uneven surfaces, the compliant control mode allows the robot to adapt to its environment. Thus the compliant nature of pneumatics allows the robot to interact with its environment in a stable manner.

Liu and Goldenburg (1991) implemented a combination of Hybrid Control and Impedance Control on a two degree of freedom direct drive robot arm: Hybrid Impedance Control. A diagonal selection matrix, S, defines which degrees of freedom are controlled through position and which degrees of freedom are controlled through force. These reseachers conducted several experiments, one involved the robot's interaction with a Variable Impedance Machine(VIM) and a second experiment involved the robot's interaction with a stiff environment. A VIM allows the user to predefine the inertia, damping and stiffness of the contact environment. In the first mentioned experiment, the authors verified that their proposed hybrid impedance control method is effective in dealing with the uncertainties inherent in maintaining contact with a compliant environment. In the second experiment, the two degrees of freedom robotic arm made contact with a stiff environment, an aluminum alloy. The test results indicate that when the end-effector approaches a stiff environment, with a properly limited predetermined tip velocity, the contact is bounded and stable. This is the major limiting factor of their work. If the contact velocity must be limited below a specified value for bounded and stable contact to occur then why not approach the environment as fast as possible and immediately before contact set the velocity of the end-effector to zero. Zero velocity implies stability. Also, their experiment based theory, when applied to mobile robots, could not hold in practice. Limiting the contact velocity of a mobile robot engaged in a trotting gait over uneven terrain is impossible.

Akella et al. (1991) are currently developing a semi-active Soft Fingertip using *electro-rheological*(ER) fluids. Their objective is to control manipulator contact interaction through contact force control by varying the damping properties of ER fluids. These fluids change their phase, and consequently their rheological properties,

based on the electric potential applied across them. Thus depending on the finger tips impact velocity the contact impulse forces can be dissipated through a properly applied electric potential. Their experimental results show that maximum energy removal is achieved when the force being exerted on the damper is equal to the maximum force allowed by the sensor and the object. Another important result was that maximizing energy removal is not the desired response because the final position of the finger is typically not at equilibrium. Finally, critical damping achieved the fastest settling time. These results suggest a solution for describing the desired properties of the optimal ER fluid which minimized contact settling time and energy absorbtion. They do not investigate the effects of varying the stiffness of the contact interaction because their setup does not include a means of varying the stiffness. The finger tip design does however include an elastic second membrane which provides a restoring force.

A limitation of the Soft Finger tip design is that it would not be durable enough to be used directly on the interface of mobile robots. Considering that mobile/walking robots are on the order of several hundred pounds, walking over rough terrain (concrete, mountain terrain) would inevitable destroy them. Incorporating the compliant behaviour into the actuators themselves would clearly be more general and is believed to be a better approach.

Laurin-Kovitz et al. (1991) are actively involved with the research and development of two mechanical devices: a binary damper and a tuneable spring. Proposed is a non-backdrivable actuator with the mechanical elements mounted between the actuator driver and the end effector. During interactive tasks the mechanical elements can be adjusted to respond to a variety of tasks or react to sense forces, positions and velocities. Still in the preliminary design stages of development their future work involves prototype adjustment, single link manipulator construction for passive impedance verification and high speed assembly evaluation. The development of working *Programmable Passive Impedance* components opens the

door to all kinds of interesting research.

In summary, active compliance is a current area of research. Compliance can be incorporated into a robot structure in three ways: compliant kinematic links, compliant actuation and compliant "skin". The choice depends on the application and bandwidth requirements; however, each choice ultimately provides the ability to couple, in a stable manner, the end-effector with its environment. Compliance is required during all phases of the contact process. It absorbs the energy associated with contact impulse forces, it prevents sensor and robot damage and stability is enhanced during environment interactions. Two situations where assembly robots require compliance is during object acquisition and parts mating. For mobile robots compliance is required during making contact with the terrain upon which it navigates. Mobile robots are still in their infancy relative to their fixed assembly counterparts. Several devices have been proposed and designed to investigate compliance, some of which are active and some semi-active.

Chapter 3

3.0 Experiment Models and Research Facilities

Chapter 3 focuses on the research facilities and other pertinent concepts developed specifically for the investigation of the benefits of incorporating programmable compliance into manipulator architectures. Initially the process of contact is divided into strategic time frames. These time windows provide the foundation for the dynamic approach taken in this thesis to controlling compliance during the contact process. The numerical model and software program of the single degree of freedom direct-drive robot are developed followed by its physical counterpart. Finally the numerical simulation software model is compared to the experiment setup.

3.1 Environment Interaction Phases

Environment interaction is fundamental to the robot industry's existence.

Physically implementing and achieving this interaction is complex. However, the process of contact can be clearly separated into three distinct main categories: *Pre-Contact Phase*, *Transitional Phase* and *Post-Contact Phase*. Both Pre-contact and Post-contact phases have received considerable attention since the beginning of the robot era in the early 1960s (An and Hollerbach, 1987; Colgate and Hogan, 1989; Kazerooni, 1987; Mason, 1981; Eppinger and Seering, 1992; Mills, 1990). The *Transitional Phase*, however, has not been examined in great detail (Mills and Nguyen, 1992).

Literature does not indicate a standard for referencing the various phases of the contact process. Mills (1990) refers to the process of making and breaking contact as *non-contact motion* and *contact motion* but does not uniquely identify the process of making and breaking contact, however, refers to making contact as, "begins with a transition" , breaking contact with, "terminates with a transition" or simply states, "transition". Akella et al. (1991) refer to these phases as: *Pre-contact*, *Middle*, and *Post-contact* phases. Another term used in literature to describe the contact process is, " ...the phase of the physical contact...(Zheng and Fan, 1991). Mills and Nguyen in 1992 still refer to this process as, " ..the robot transition to and from contact with the work environment...". It is recognised that these authors were not involved with the approach taken in this thesis and thus specific definitions were not required.

Coupling a robot to its environment occurs during the *Transitional Phase* and presents a relatively unexplored domain (Mills and Nguyen, 1992 and Zheng and Fan, 1991). As mentioned, Akella et al. (1991) refer to this phase as the *middle-phase* and further state that an issue of concern during this phase is the need to make smooth transitions from position control(pre-contact) to force control(post-contact). The *Transitional Phase* can be subdivided into two distinct intervals: *Impact Phase* and *Recovery Phase*. These two phases are inclusive and based on the assumption that contact between the robotic manipulator and the environment is continuous. The

described contact phases are applicable to both legged and assembly type robots.

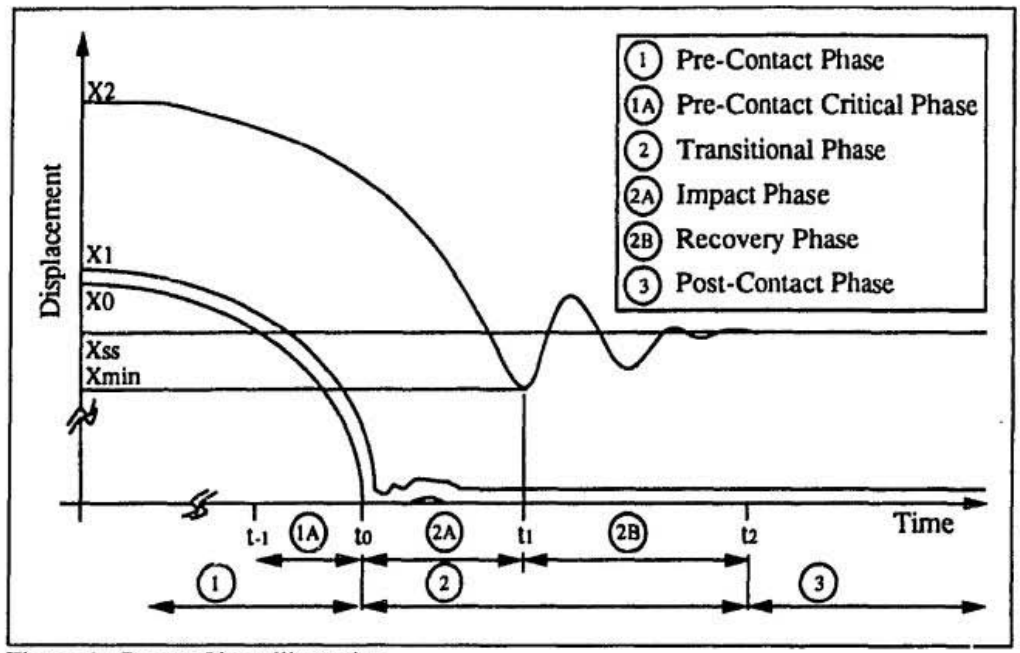

Figure 1: Contact Phase illustration.

Figure 1 illustrates the phases associated with contact. The actuator is described by three displacement state variables *X2*, *X1*,and *X0* which are symbolic of the actuator's length and represent a single link. The steady state actuator displacement is represented by X_{ss}. The described actuator is functionally generic and further explained in section 3.2.1.. During *Pre-Contact* the actuator is stable and maintains a prescribed "natural" length indicative of the task at hand. As the tip of the actuator approaches the environment *Pre-Contact Critical Phase* is entered. During this phase contact is pending and preliminary calculations, for example, kinetic energy and impact forces, will accommodate a smoother transition into *Impact Phase*. The distance from the robot manipulator and the object at which *Pre-Contact Critical Phase* is entered depends upon the bandwidth of the complete robotic system. Entering into this phase does not imply contact is eminent, however, it implies that contact is pending. The *Transitional Phase* occurs between times t_o and t_2. At t_o, the

actuator makes contact with the environment and is the beginning of *Impact Phase*. Contact with the environment is represented by zero displacement. The *Impact Phase* dissipates the energy associated with contact which is due predominantly to inertial forces and impact forces. It represents a period of maximum deformation, X_{min}. The *Recovery Phase* occurs between t_1 and t_2. This part of the transient response associated with contact is defined from the maximum compression(X_{min}) of the actuator, which is actually a minimum relative to zero displacement, to the steady state displacement, X_{ss}. Note that this phase represents a period of restoration. When the transient behaviour of *Recovery Phase* becomes manageably stable, *Post-Contact Phase* is entered. Post-contact is defined for t greater than t_2 and is characterized by stable continuous contact with the environment/object. Defining the onset of this phase is arbitrary and is based upon the manipulative abilities of robot. Classical transient-response specifications include a $\pm 2\%$ and $\pm 5\%$ tolerance band which corresponds to a specific settling time. This settling time will be defined as t_2. *Post-Contact Phase* is terminated by the robot's instruction to execute another task, hence, the domain of Pre-Contact is entered and the cycle continues.

3.2 Mathematical Model

A lumped parameter model representing a single degree of freedom direct-drive robot manipulator was designed to facilitate a detailed investigation of the contact process. For the derivation of this model and its equations several limitations were imposed. Typically, the dynamic characteristics of any real world model are never totally accounted. This is not to say that a complete model is not desired, the problem is that it is very difficult to model and/or predict every dynamic characteristic, for example, impact forces. From this perspective it is appropriate to make several assumptions which will reduce the analytical complexity while still maintaining the significant/dominant characteristics of the system. Thus the system parameters can be analyzed individually and recorded with a reasonable amount of confidence.

Of the three main types of frictional forces present in a mechanical system, Viscous friction(B_v), Static friction(B_s) and Kinetic friction(B_k), only B_v is used in the model. This is justified in the following arguments. First of all, the programmable damping effects are completely viscous and will be constantly varied to values far exceeding the magnitude of B_k. Second of all, kinetic friction effects are scalar and can be subtracted from the generated forces if required. Finally, even though the effects of B_s will ultimately impose an impulse force spike immediately after impact, this can be accounted for in software if necessary. A reasonably accurate model of the actuator can therefore be obtained by concentrating on viscous friction alone.

One of the numerical simulation's main objectives is centred around investigating forces generated on the robot, F_{robot}, during environment interactions. The extreme case, in terms of generating forces during impact, is to have two rigid colliding bodies. In terms of the simulation analysis the two colliding bodies are the robot tip and the environment. Since the robot model can be programmed to exhibit

any degree of compliance the environment should be modelled as a rigid body. A compliant environment will facilitate the contact process. The objectives of this thesis are focused on the actuator facilitating the contact process completely. Hence, making the environment model rigid ultimately places the environment interaction demands upon the actuator.

The complete actuator model is illustrated in Figure 2. It consists of two coupled single degree of freedom linear second order lumped parameter models, the actuator itself and a rubber tip.

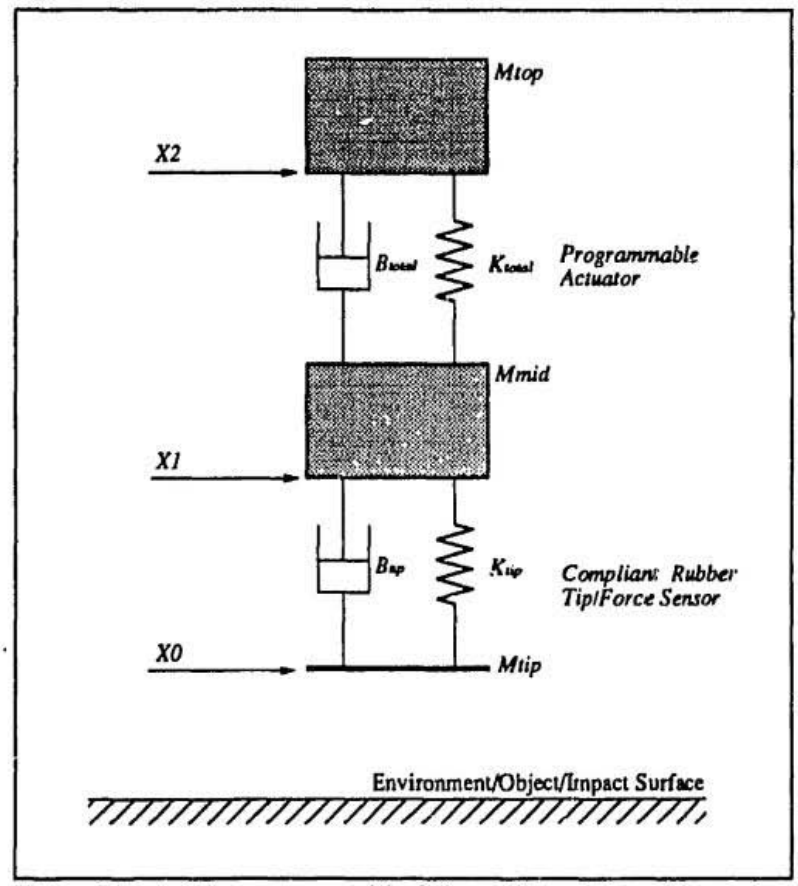

Figure 2: Lumped parameter model of direct-drive robot model.

The dynamics of the complete robotic arm model are mathematically described by summing the forces at each node:

From node II:

$$M_{top}\frac{d^2X_2}{dt^2}+B_{total}\frac{d(X_2-X_1)}{dt}+K_{total}(X_2-X_1-lo_{spring})=M_{top}\cdot g \quad (1)$$

From node I:

$$M_{mid}\frac{d^2X_1}{dt^2}+F_{B_{tip}}+F_{K_{tip}}-B_{total}\frac{d(X_2-X_1)}{dt}-K_{total}(X_2-X_1-lo_{spring})=M_{mid}\cdot g \quad (2)$$

From node 0:

$$M_{tip}\frac{d^2X_0}{dt^2}-F_{B_{tip}}-F_{K_{tip}}=M_{tip}\cdot g \quad (3)$$

The term B_{total} represents the effective damping force(s) imparted on the system. It consists of the experiment's constant viscous coefficient, B_v = 0.115Ns/m, the motor viscous damping, B_m = 0.01Ns/m (refer to Appendix A, Section A.9) plus the programmed viscous damping coefficient, B_p. The term K_{total} represents the effective spring force(s) imparted on the system. It consists of the physical spring constant, K_c = 18.33N/m (refer to Appendix A, Section A.6) plus the programmed spring coefficient, K_p. F_{Ktip} is the nonlinear force generated by the rubber tip and F_{Btip} is the tip damping force, both are described in Section 3.2.2.

3.2.1 Actuator Model

The actuator model is representative of many situations applicable to the robotics industry. Its translational nature lends itself for direct comparison with single axis linear hydraulic, pneumatic and electric drives used in prismatic and revolute actuation. Specific locations could include actuation both in closed and open kinematic chain configurations as well as end-effector applications, for example, active RCC devices or a single finger/digit manipulator.

The actuator model contains several parameters which are representative of a typical robot structure. Mass M_{top} represents the effective mass of the robot's lower kinematic chain. For a fixed robot application this is the linkage portion towards the base mount. In a mobile robot, quadruped/hexaped etc, it is representative of the payload mass and the robot itself. Representing the robot as a lumped rigid mass places all the responsibility of controlling the contact process on the actuator. Mass M_{mid} represents the effective mass of the robot's upper kinematic chain. For both fixed and mobile robot applications this is that portion of the kinematic chain located on the manipulator/ interface side. Mass M_{tip} represents the mass of the force sensor/rubber tip interface.

The actuator's ability to implement programmable damping and stiffness is represented by B_p and K_p. The translational nature of the model implies that both B_p and K_p will take the form of *Compressive Compliance*.

It should be noted that even though the model is translational in nature its dynamical behaviour is also applicable to rotational configurations and the experimental results of the actuator model can be generalized to include not only articulated hand implementation of fixed industrial robot manipulators but also one-legged and multi-legged mobile robots.

3.2.2 Interactive Tip Model

The Actuator model incorporates a compliant interactive tip. It can represent a rubber sheath or a force sensor, see Figure 2. The tip model is dynamically characterised by a second order mass/spring/dashpot system and helps the actuator interact with its environment while providing the capability of maintaining contact stability. The tip does not replace the programmable actuator's functionality; it

simply allows the actuator to couple with the environment while partially absorbing the initial impulsive forces generated during impact. It also allows time for a real programmable actuator, which is bandlimited, to respond to the impact. Another significant feature of the interactive tip is based upon the problem that the impact velocity is not necessarily adjusted to accommodate the transition between *Pre-Contact Phase* and *Post-Contact Phase*. In a free falling situation, for example, running gaits of a quadruped, modifications and adjustments to the impact velocity are virtually impossible, therefore, to accommodate for the impact force(s) generated during contact with non-compliant surfaces a compliant interface is necessary. This compliant interface is provided by the rubber tip. In high bandwidth robotic applications where actuation is applied through back drivable techniques, situations may arise where the interface velocity cannot be sufficiently reduced. In such cases a compliant rubber tip is necessary. Also, in applications involving non-backdrivable actuation (high impedance kinematic chain) a compliant tip interface would mask the resolution discrepancies between the robot and the task.

3.2.2.1 Tip Characteristics

Realizing a model for the actuator tip spring centred on developing a mathematical non-linear approximations, for K_{tip} and B_{tip}, which would characterize the behaviour of rubber. The optimal response for K_{tip} would allow extremely low linear reactive forces to be generated during initial displacements and extremely high reactive forces for larger displacements. Damping would ideally take into account hysteresis effects. Overall, the dynamic response should exhibit overdamped behaviour.

3.2.2.1.1 Spring Considerations

The desired response for K_{tip} is characteristic of the material properties exhibited by a large class of polymer materials [Billmeyer, Textbook of Polymer Science]. These materials produce extremely low linear reactive forces during displacements less that 50% to 60% from equilibrium and extremely high reactive forces for displacements greater than 50% to 60%. Natural rubber impregnated with circular air pockets was chosen as the material for the tip.

Figure 3 describes the relationship between applied pressure and percent compression of natural rubber impregnated with bubbles. The Figure has been reproduced from Appendix B for convenience and the material and compression curve were obtained from INSTRUMAR Limited (1992). There are two separable phases exhibited which are distinguishable around 55% compression. Up to 55% compression the data point trend is approximately linear. Above 55% the pressure required to compress the rubber increases exponentially. This transition is called void fraction and occurs when the impregnated bubbles have collapsed.

Mathematically the rubber's compressive behaviour is represented by the Equation 4 and graphically illustrated in Figure 3.

$$F_{K_{tip}} = K \times \ln\left[\frac{1+Max\left(\frac{X_1 - X_0 - lo_{tip}}{lo_{tip}}\right)}{1-Max\left(\frac{X_1 - X_0 - lo_{tip}}{lo_{tip}}\right)}\right] \qquad (4)$$

where K = Spring constant scalar = 2.0

Max = tension/compression scaler = 1.525

lo_{tip} = Natural rubber tip length = 0.3175cm

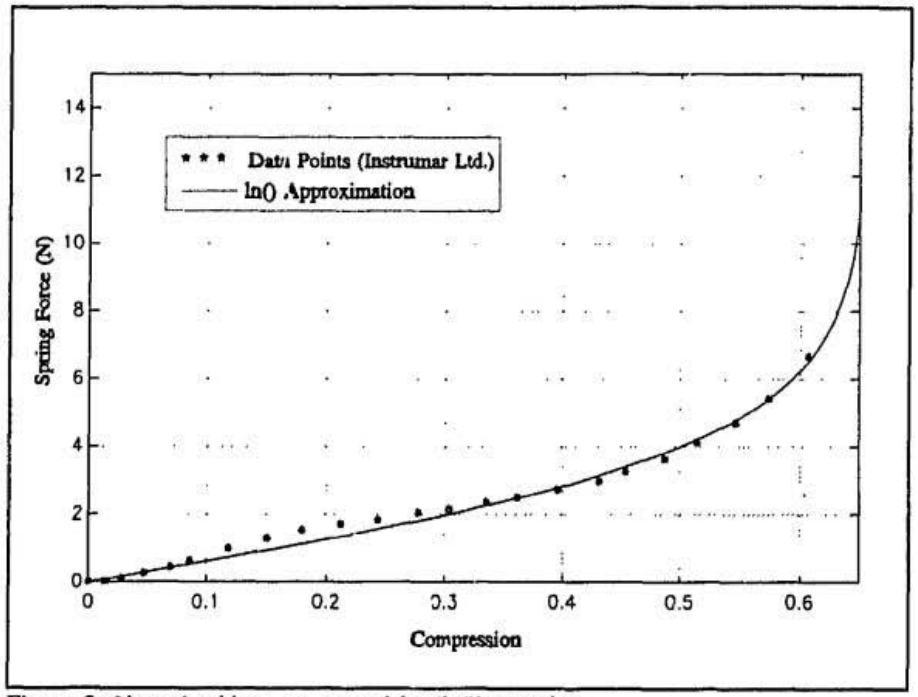

Figure 3: Natural rubber -vs- natural log(ln()) mapping.

The singular points occur at approximately $\pm 65.5\%$ compression. Details of the derivation are contained in Appendix B.

During contact the rubber tip will be in compression. The only possible situation when tension may exist is during non-contact situations when the tip is returning to its natural length. Since the characteristic response is overdamped tension will never occur. Therefore, the tension quadrant equation was made identical to compression and one equation will suffice. Natural rubber was used in the actual experiment tip interface.

3.2.2.1.2 Damping Considerations

Newtonian fluid characteristics are used in the development of the rubber tip dynamics. The only critical decision, since the effective spring behaviour is non-linear, is to ensure overdamped behaviour over a reasonable compression range. Hysteresis effects were not obtained from the natural rubber samples, therefore, a constant viscous coefficient for the frictional effects is used. Its value was determined based upon the effective spring graph, Figure B5, Appendix B. At the singular points K_{tip} equals infinity which will never occur during the simulation. An arbitrary reasonable limit was imposed upon K_{tip}: $K_{tip} \leq 10000$, which translates into a rounded off value for B_{tip} of 1.0Ns/m. This value for B_{tip} allows the spring to compress up to $\approx 60\%$ and still maintain overdamped behaviour.

3.2.3 Numerical Simulation Model

The complex non-linear nature of the programmable damping, B_p, and programmable spring, K_p, coefficients demanded during the discussed contact phases present a very challenging endeavour in terms of analyzing their potential in facilitating contact. Mathematically, there is no explicit closed form analytical solution. The model equations, 1, 2 and 3, are highly non-linear not only as a result of variable damping and spring coefficients but also due to the uncertainties inherent in the environment itself. Therefore, solving the equations is left to numerical integration. Using Euler integration, equations 1, 2, and 3 are written as:
Upper Platform:

$$V2_{new} = V2_{old} + \Delta t \times \frac{[F_{K_{total}} + F_{B_{total}} + M_{top} \times g]}{M_{top}} \qquad (5)$$

$$X2_{new}=X2_{old}+\Delta t\times V2_{old} \tag{6}$$

where $V2_{old}(t=0) = 0.0\text{m/s}$
$X2_{old}(t=0) = X1_{old}(t=0) + lo_{spring}$

Middle Platform:

$$V1_{new}=V1_{old}+\Delta t\times\frac{[FK_{tip}+FB_{tip}-F_{K_{total}}-F_{B_{total}}+M_{mid}\times g]}{M_{mid}} \tag{7}$$

$$X1_{new}=X1_{old}+\Delta t\times V1_{old} \tag{8}$$

where $V1_{old}(t=0) = 0.0\text{m/s}$
$X1_{old}(t=0) = X0_{old}(t=0) + lo_{tip}$

Force Sensor/Finger Tip:

$$V0_{new}=V0_{old}+\Delta t\times\frac{[-FK_{tip}-FB_{tip}+M_{tip}\times g]}{M_{tip}} \tag{9}$$

$$X0_{new}=X0_{old}+\Delta t\times V0_{old} \tag{10}$$

where $V0_{old}(t=0) = 0.0\text{m/s}$
$X0_{old}(t=0) = X_{init}$

The displacement initial condition $X0_{old}(t=0) = X_{init}$ refers to the user defined height at which the robotic tip is dropped from. X_{init} is sometimes referred to as the release height. All other displacement initial conditions are derived from this.

Euler's method of integration provided an effective means of solving the dynamic robot model presented by equations 1, 2 and 3. One of the major drawbacks of this integration method is that it is typically inadequate, in terms of accuracy, for

most applications. It is argued below, however, that this integration method is sufficiently accurate for deriving all relevant information required by the experiment.

Limiting the numerical integration technique to Euler's is a result of several factors. Implementing Euler's integration method is extremely easy. Secondly, the bandwidth demands of the dynamic variables is relatively small. Finally, the simulation duration is short. These factors maintained the errors associated with Euler's method at an acceptable level which is illustrated in the following discussion.

The number of iterations during a typical simulation experiment does not exceed 400500 steps. Four strategic reference points are compared to illustrate the integration method's accuracy and its implications with respect to modelling the single degree of freedom robot. These reference points are strategic in the sense that obtaining an exact value for the identified reference points is mathematically easy and they are points of interest which occur during the contact process.

The four reference points are as follows: 1) the time to impact for a free falling body dropped from a height of 1.5cm under the influence of gravity is approximately:

$$t_{impact}=\sqrt{\frac{2\times(-0.015m)}{-9.81m/s^2}}\approx 0.05530s \tag{11}$$

2) The impact velocity is approximately:

$$V_{impact}=g\times t_{impact}\approx -0.54249m/s \tag{12}$$

3) The steady state spring deflection is given by:

$$X_{ss}=lo_{spring}-\frac{M_{top}\times g}{K_c}=0.096m-\frac{0.02485Kg\times -9.81m/s^2}{18.33N/m}\approx 0.0827m \tag{13}$$

4) Under the influence of gravity the steady state force imparted on the robot, F_{robot}, is

given by:

$$F_{robot}ss=M_{top}\times g=0.02485Kg\times -9.81m/s^2\approx 0.293868N \quad (14)$$

Table I summarizes the accuracy of the Euler integration method verses the four identified strategic reference points.

Table I: Numerical simulation accuracy.

Reference points	Exact	Simulation	Percent Error (%)	#integrations $t=t_{impact}$	#integrations t = 0.5s
t_{impact} (sec)	0.0553001	0.05529963	0.000849	44,295	N/A
V_{impact} (m/s)	-0.542494	-0.542501	-0.00129	44,295	N/A
X_{ss} (m)	0.0827023	0.0827018	0.0060	N/A	400,500
$F_{robot}ss$ (N)	0.293868	0.293859	0.0030	N/A	400,500

The percent error increases as the numerical simulation evolves. After 400500 integration steps, the percent error is extremely small. Since, the simulation does not exceed 0.5s, local truncation, global truncation and round off errors are kept at a tolerable level and are essentially negligible. Also, the spectral content of the state variables and the other parameters during the contact process peak at around 100Hz. Hence, the signals are extremely bandlimited and the demands upon the integration technique are small. In conclusion, Euler's method of integration does not significantly affect the simulation accuracy.

3.3 Generated Forces

Observing equation 1 or 3, it is clear that the forces being generated during both static and dynamic states are due to the system's mass, damping and spring attributes. Gravity also affects the system under certain circumstances. Using a Free

Body Diagram, these forces can be individually accounted for: Gravitational Force (F_g), Inertial Force (F_i), Damping Force (F_d) and Spring Force (F_s). These generated forces are summed at the node interface and rearranged to give:

$$F_{generated}=Fi+Fg=Fd+Fs \tag{15}$$

which results in two distinct equations, equal in magnitude and opposite in direction. The model described represents the simplest form of a robotic member and illustrates the forces being generated and transmitted through the robot, F_{robot}, and the environment during contact, F_{object}. Thus:

$$F_{generated}=F_{robot}=F_{object} \tag{16}$$

Limiting the transmitted force can be achieved through controlling either the mass, damping or spring constant independently or in some combination. As long as the generated force is less than the critical force, damage to the robot and the manipulated object will be avoided:

$$F_{generated}\leq F_{crit} \tag{17}$$

F_{crit} is the maximum force which is allowed to be transmitted through the robotic kinematic chain and/or the manipulated object. Its value is limited and determined by the physical structure of the robot and the breakage threshold of the object being manipulated. Thus two force thresholds can be defined: F_{crit_Robot} and F_{crit_Object}. Consideration also must be given to actuator limitations; however, in the present study actuator limitations are not considered.

Consider equation $F_{generated} = F_i + F_g$. It would be extremely difficult under practical conditions to alter the effective mass of the system under any control strategy. Even though hydraulic actuators, if used, affect system mass, achieving zero or even pseudo negative mass is virtually impossible, thus, this variable is assumed constant. Gravitational effects are completely uncontrollable. Since acceleration is a function of the systems state and not a primary variable this equation

is not the best choice for force control. The equation is fundamentally a dependant representation of the system's instantaneous state, exemplifying consequential second order effects.

Consider equation $F_{generated} = F_d + F_s$. It consists of the two state variables, position and velocity, from which the original equation was developed, and also damping and stiffness coefficients. From a practical perspective, damping and stiffness coefficients are controllable quantities. In contrast, this equation is more primary and the prudent choice in describing and manipulating the forces generated during the contact cycle.

3.3.1 Ideal Damping and Stiffness Laws

Altering the generated forces during the various phases of contact, as mentioned, can be achieved by changing the damping and spring coefficients of the system. From the equation: $F_{generated} = F_d + F_s \leq F_{crit}$, *Ideal Damping* and *Ideal Stiffness* laws can be derived. These equations are ideal because they represent solutions to the programmable compliant interaction strategy under force constraint. Both are conceptual and have no upper or lower limits. Thus, ideal damping and ideal stiffness theoretically are able to behave in a continuous fashion between negative infinity and positive infinity with infinite bandwidth. Each equation is completely capable of independently facilitating contact while limiting $F_{generated}$ below F_{crit_robot} and F_{crit_object}.

Programmable damping, based on the described model, is mathematically depicted by the relationship:

$$Bp \leq \frac{F_{crit} - K_{total} * X}{\dot{X}} - Bv \qquad (18)$$

and represents the *Ideal Damping Law* for a single degree of freedom second order nonlinear mass/spring/dashpot system for a single kinematic link under the constraint of force limitation. The term, K_{total} * X, represents the effective spring force(s) imparted on the system. Force contribution occurs only when the spring is displaced from the spring's natural equilibrium position. And, of course, the magnitude and force direction depends on the spring characteristics and whether or not the spring is in compression or tension.

Programmable stiffness, based on the described model, is mathematically depicted by the relationship:

$$Kp \leq \frac{F_{crit} - B_{total} * V}{X} - Kc \qquad (19)$$

and represents the *Ideal Stiffness law* for a single degree of freedom second order nonlinear mass/spring/dashpot system for a single kinematic link under the constraint of force limitation. The term, B_{total} * V, represents the effective damping force(s) imparted on the system. Force contribution occurs only when the system is in motion. And, of course, the magnitude and direction of force depend on the velocity.

Note that these equations are not independent: K_{total} is a function of K_p and B_{total} is a function of B_p. Also, both equations are inequalities. At the force boundary, when F_{crit} is being generated, both damping and spring coefficients are at their limit. In this case $B_p = B_{crit}$ and $K_p = K_{crit}$.

3.3.2 Force Control Strategy

Altering the effective spring parameter, K_{total}, alone during the contact process does not lend itself to complete controllability. Increasing the spring constant increases the natural undamped frequency of the system and directly facilitates unstable oscillatory behaviour. It increases the transmitted force and also decreases the separation of X_{ss} with respect to the spring's natural length which reduces the ability for the manipulator to maintain contact. Decreasing this parameter provides increased stability and a reduction in the transmitted force, $F_{generated}$, but at the expense of necessary contact retarding forces, required during *Impact Phase*, and the necessary recovery energy/force required to facilitate optimal recovery performance during *Recovery Phase*. In contrast, varying the damping parameter to facilitate contact fundamentally provides a more stable transition. A low damping coefficient (could be negative) limits the transmitted force during contact which not only lends itself to contact controllability but increasing this parameter can also provide maximum energy dissipation control under a force control contact strategy. However, it should be noted that negative damping also facilitates unstable behaviour.

In essence, an effective and adaptive control strategy will provide real-time adjustments to both the stiffness and damping coefficients during each of the contact phases while conforming to the task constraints. The proposed force control strategy is a combination of proportional and differential control.

3.4 Experiment Model

Confirmation of the numerical simulation results was accomplished through the development of a single degree of freedom direct-drive robotic arm. High bandwidth and component availability, both electrical and mechanical, were two of the main design criteria along with maintaining the model at a simplistic level without compromising system performance. Figure 4 illustrates the overall experiment setup (see Appendix C). Data acquisition and system interface was provided by a Keithley 575 measurement and control system. Several electrical sub-systems were developed which provided sensor interfacing and signal conditioning, a solenoid driver for initiating the experiment and also a voltage controlled current source to generate the desired force. The sensors were sampled through a multiplexed 16 bit A/D converter and the motor was controlled through a 12 bit D/A converter. Software control was provided by a 33MHz DELL computer and a real-time interrupt driven interface program.

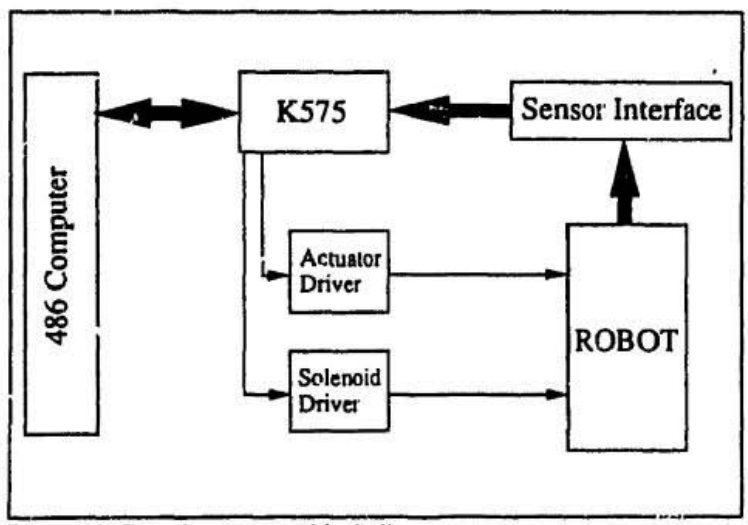

Figure 4: Experiment setup block diagram.

3.4.1 Direct-Drive Arm

The robot arm is designed to facilitate real-time manipulation of the compliant damping and spring variables during the described phases of contact. It represents a single link/digit which would be typically located on the end-effector of either a mobile or fixed robot. Figure 5 illustrates the complete final design concept. The robotic arm is coupled directly to the actuator shaft and is held suspended off the impact surface by a solenoid release mechanism. Upon release, the arm descends toward the impact surface under the influence of gravity, contacts the impact surface and eventually comes to rest.

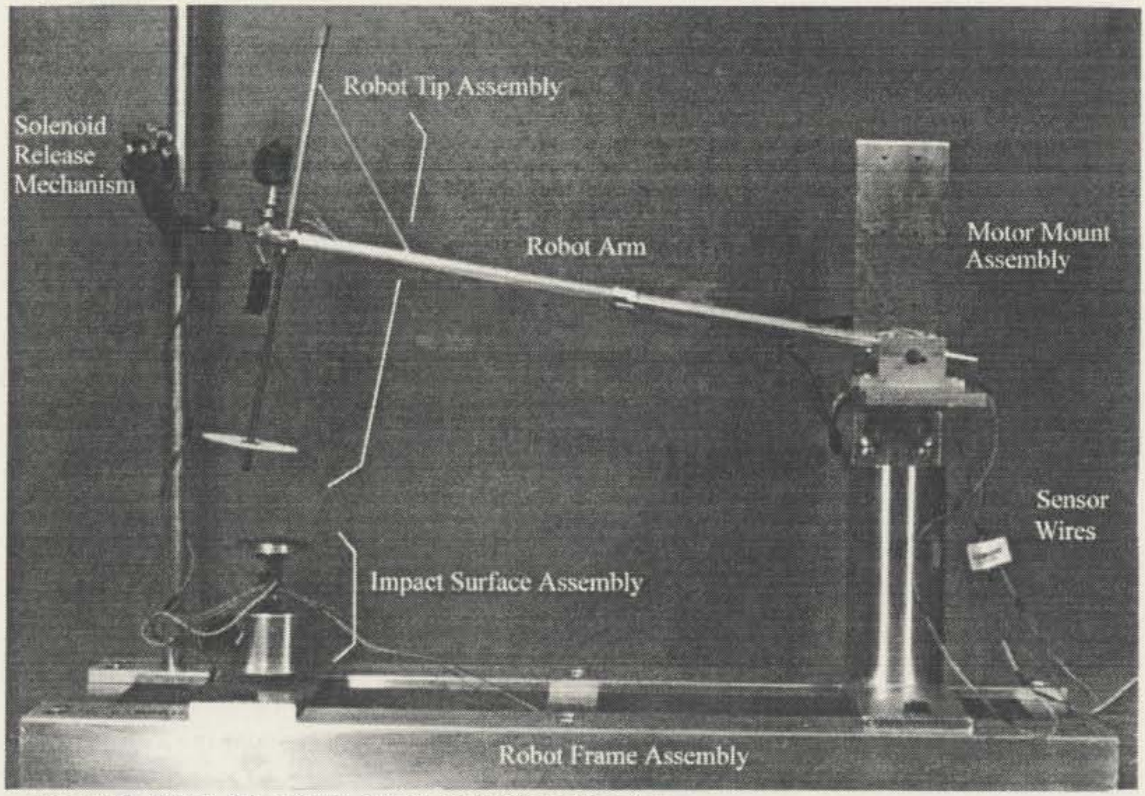

Figure 5: Direct-drive single degree of freedom robot arm.

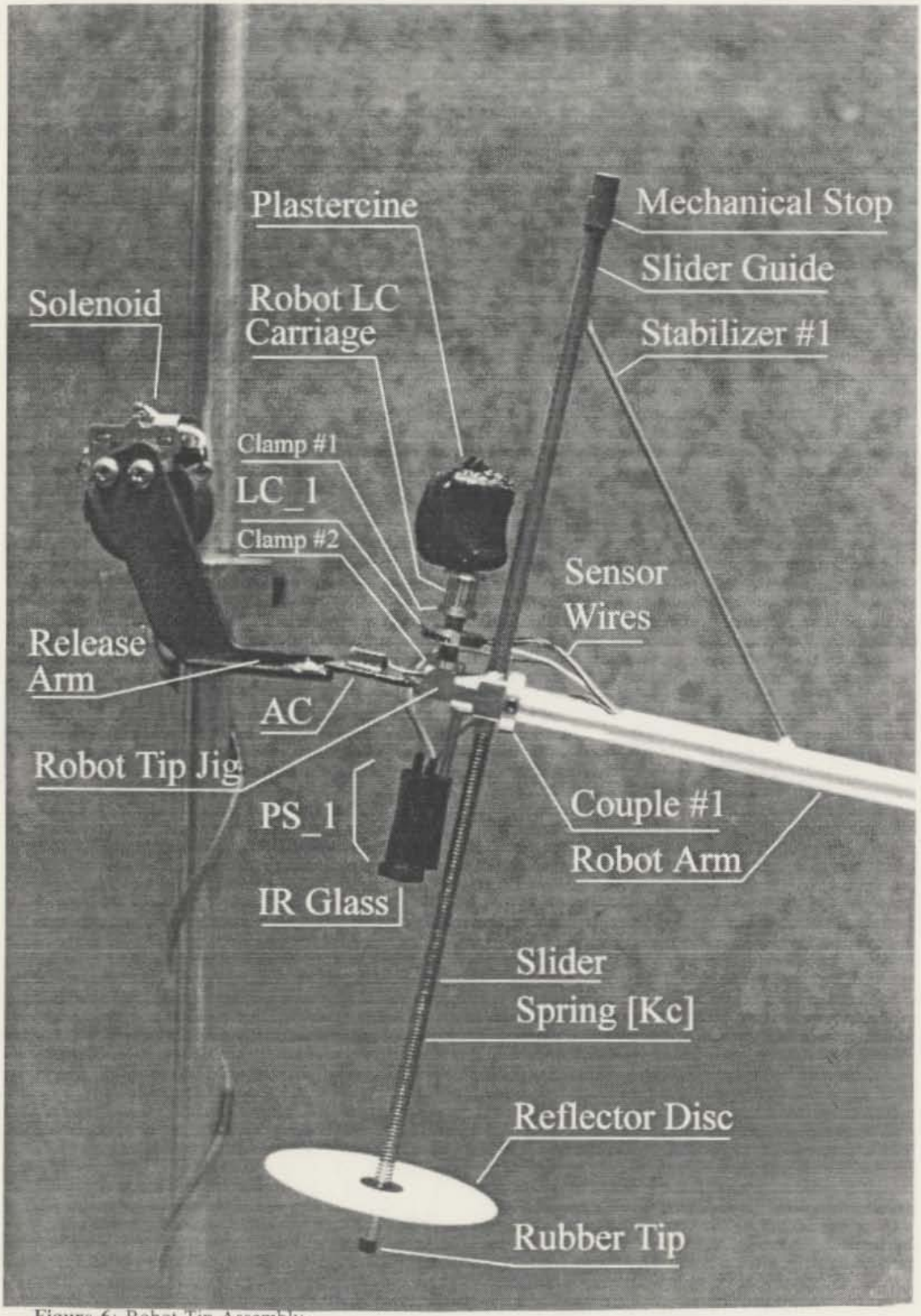

Figure 6: Robot Tip Assembly.

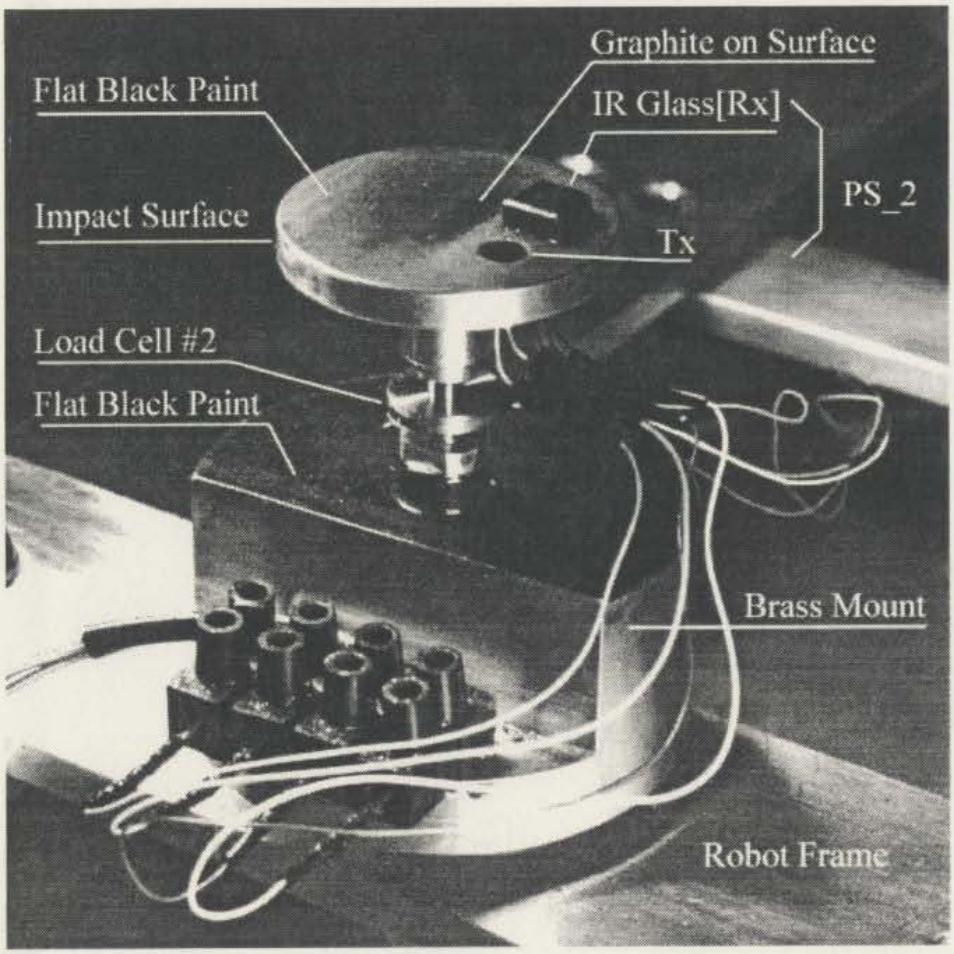

Figure 7: Impact Surface Assembly.

Materials used for constructing the robot arm include tape, epoxy, rubber support pads, flat black paint, heat shrink, aluminum, brass and plastercine. The main objective focused on keeping the overall mass of the robot components at a minimum. All critical mass components, which refers to the components located on the *Robot Tip Assembly* (Figure 6), were manufactured from stock aluminum or aluminum tubing. The *Reflector Disc Tip* and the *Robot Tip Jig*, see Figure 6, components are hollow in an effort to reduce the robot's overall mass. A complete

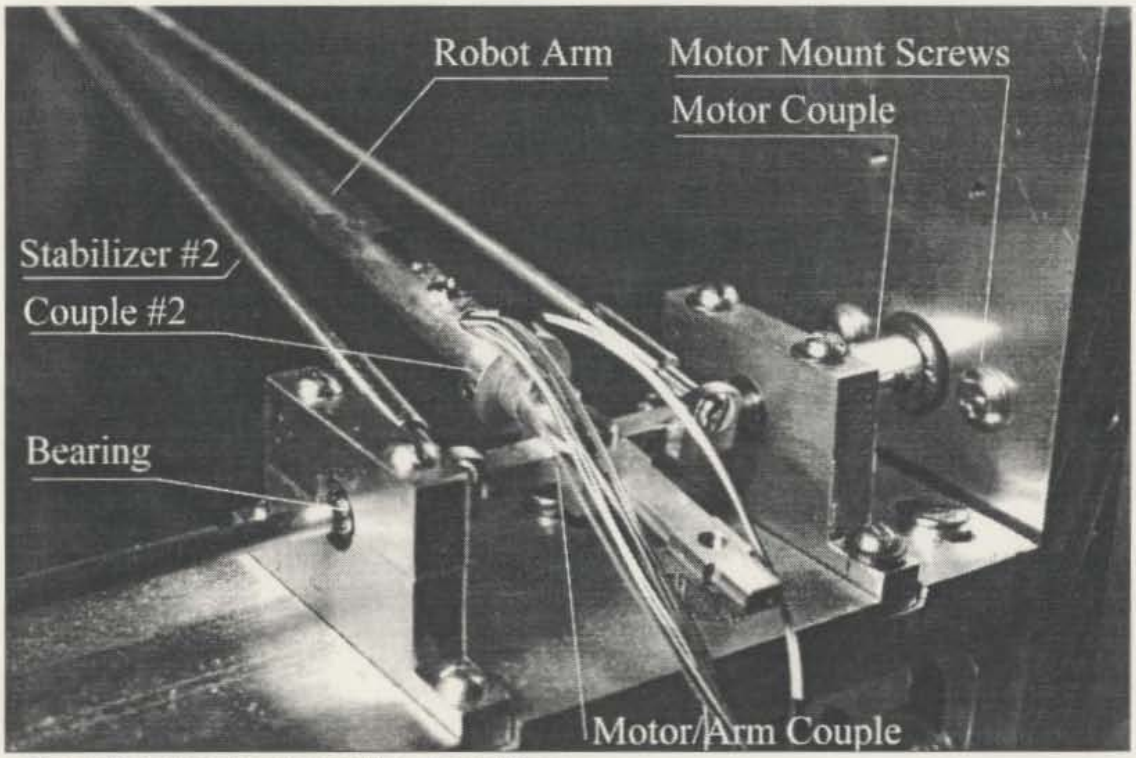

Figure 8: Motor Mount Assembly - Angle View.

list of the component masses and important dimensions are listed in Appendix A.

Figures 6, 7, 8 and 9 highlight the robot arm's three major sub-components. In each figure a name description of the individual components is given. Referring to Figure 6, upon contact with the *Impact Surface* the *slider* moves vertically through the *slider guide* and in the process compresses the spring. Mounted on top of the *slider* is a *Mechanical Stop*. It was manufactured out of heat shrink and prevents the *Reflector Disc Assembly Unit* from falling through the *slider guide* and also prevents the spring from entering into tension. Notice the location of Proximity Sensor #1, Load Cell #1 and the accelerometer sensors. Sensor details are contained in Appendix C. The sensor wires are bussed through the *Robot Arm*.

Figure 7 illustrate the *Impact Surface Assembly* components. All flat surfaces

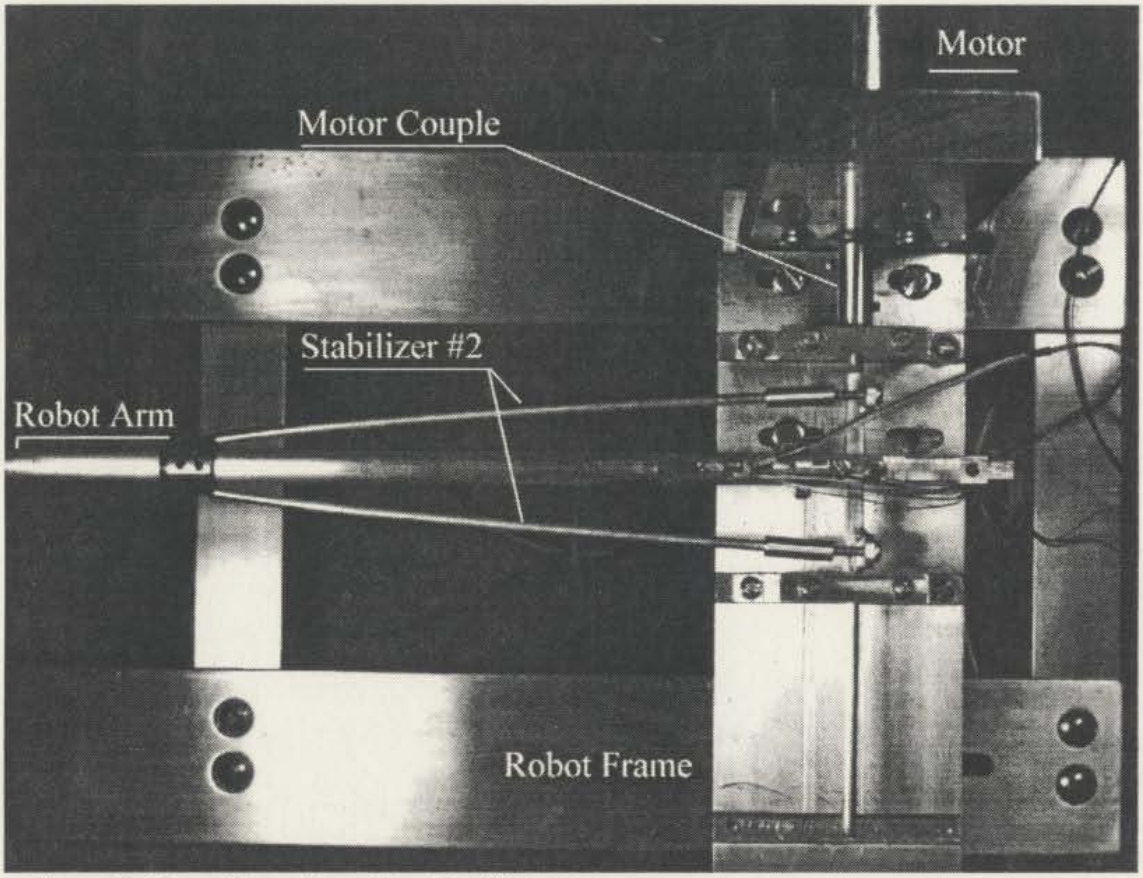

Figure 9: Motor Mount Assembly - Top View.

facing the *Robot Tip Assembly* are painted flat black. This reduced the ambient light interference from overhead incandescent lighting and also reduced unwanted emissions from the Proximity sensors. Note the location of Load Cell #2 and Proximity Sensor #2.

The *Motor Mount Assembly* is illustrated in Figures 8 and 9. Stabilizer #2 reduces the lateral motion of the motor/arm couple. By adjusting the tension screws the desired amount of lateral stiffness can be applied. Note the sensor wires and the motor location.

3.4.1.1 Actuator Details

The actuator used in the robot arm is an armature controlled permanent magnet DC motor. This provides a means of force control based on the torque equation: $T = K_m I_a$. Due to the motor's small rotor diameter(19.66mm) and small mass(37.33grams), its inertia effects are negligible compared to the robot arm. The mass moment of inertial of the rotor is $I_{rotor} \approx 0.000001803 kgm^2$ and the mass moment of inertia of the robot arm referenced to the motor shaft is $I_{robot} \approx 0.003246 kgm^2$. Since I_{robot} is ≈ 1800 times greater than I_{rotor}, we can neglect the rotor's effect on the overall system dynamics (see Appendix A, Section A.3 and Section A.8).

Typically, internal feedback of an armature excited DC motor is generated by back e.m.f. Because the maximum release height of the robot, during experimentation, is restricted to 2.5cm, the maximum drop angle is 4.53 degrees: 1.26% of a revolution. Upon impact, the maximum angular velocity is extremely small ($V_{tangential} \approx -0.7 m/s$). Based on this height restriction the velocity related back e.m.f effects can be ignored. Through the same reasoning the rotor effects discussed in the previous paragraph, which are based on I_{rotor} and angular acceleration, are clearly negligible.

Limitations imposed on the release height make the dynamic related terms in the DC motor feedback loop negligible. Essentially, the motor's operation can be considered static. As a result, the mechanical time constant is negligible and the motor bandwidth is limited by its electrical time constant: $\tau_e \approx 486. \mu sec => BW \approx 327.5 Hz$. Refer to Appendix A, Section A.7 for motor inductance and resistance measurements.

The only dominant effect the motor imposed upon the direct drive robot during the contact process is the retarding characteristics of the permanent magnet/armature core field interaction, B_m. Ultimately, this adds a damping effect which opposes the robot motion during each phase of the contact process. Modelling B_m can be achieved

by referencing its effects to the shaft of the motor, thereby retaining the motor as an ideal force controller. Appendix A, Section A.9 contains the results of two experiments: contact process with the motor installed and contact with the motor removed. The time taken between release and contact with the impact surface is longer with the motor installed. This time difference is a measure of the motor's viscous damping coefficient B_m. Evaluating the time difference is, however, difficult because the measurement accuracy is impeded by the sampling frequency. By measuring the magnitude difference between the output of LC_1, F_{robot}, an approximation of B_m can be obtained. The effective viscous damping effect resulting from the field interaction and referenced to the shaft of the motor is $\approx$0.00325Ns/rad. This translates into a retarding force of $\approx$0.01057Ns/m referenced to the composite centre of gravity(CG_{total}= 0.3077m). Thus, $B_m \approx$ 0.0106Ns/m. The numerical simulation includes B_m as a constant viscous force opposing the motion of the upper mass, M_{top}. Thus, $B_{total} = B_p + B_v + B_m$. Changing the motor will affect the analysis.

3.4.1.2 Sensor Details

Five sensors provide feedback and capture the essential dynamics associated with contact: an accelerometer(AC), Load Cell #1(LC_1), Load Cell #2(LC_2), Proximity Sensor #1(PS_1) and Proximity sensor #2(PS_2). Load Cell #1 measures the forces being experienced by the robot, F_{robot}, and LC_2 measures the forces experienced by the object, F_{object}. Proximity Sensor #1 measures spring deflection and PS_2 measures the distance between the reflector tip assembly and the impact surface. Both load cells are 5N tension/compression devices, the accelerometer is rated at $\pm$ 5g's, and the proximity sensors were designed using spectrally and mechanically matched Infrared transmitter/receiver pairs. Sensor details are contained in Appendix C and the sensor mount locations are illustrated in Figures 5, 6, 7, 8 and 9. These

five sensors are sufficient to identify the phases of contact and through software integration and differentiation enabled the dynamics occurring during contact to be measured.

3.4.1.3 Discussion

One of the major drawbacks of motor actuated direct-drive systems under gravitation is that the load must be borne by the motor entirely and directly (Asada and Youcef-Toumi, 1987). Not only is the motor providing joint actuation but it also provides support. This causes overheating problems and directly affects the motor dynamics, reduces the system's bandwidth and may destroy the motor. The experimental setup developed at Memorial eliminates these load/robot related problems by separating the two demands upon the motor with the use of a physical spring, K_c. Gravitational induced forces resulting from the robot mass, sensors and even the spring mass itself are completely supported by the spring leaving the motor to provide appropriate reactive contact forces. Therefore, the downward system motion, which mimics the arm approaching an object, is provided by gravity and is independent of the motor's existence. The responsibilities of the motor are decoupled to facilitate a more accurate investigation of active contact force control.

The peak power required to control the motor under the constraints of force and/or position control is high, even with the motor responsibilities divided. The total energy required, however, is small. Contact typically takes less than 0.5s which is the duration of the power consumption period. Peak motor current demands are $\approx \pm$7amps@70volts. It should be noted that the experiment setup is research based and the described power requirements exceed the power requirements of practical applications.

It is essential to evaluate the maximum payload mass the motor could handle during the contact force control strategy. This ensured that the motor would at least be capable of providing and tracking a command force. Using the motor torque equation, $T = K_m * I_a$, and the mechanical advantage associated with the robot, $T = F * L_{arm}$, the maximum force can be evaluated:

$$F_{maximum} = \frac{K_m \times Ia_{max}}{CG_{total}} = \frac{0.016 \times 5.0}{0.3077} \approx 0.26N \quad (20)$$

where K_m = Motor Constant
Ia_{max} = Max armature current(A)
CG_{total} = centre of gravity
(see Appendix A)

from which the maximum payload mass is determined, $M_{max} = F_{maximum}/gravity \approx$ 26.5 grams. Based on this target payload mass the arm components were machined. The complete and assembled robot, including sensors, were weighed, its mass determined and subtracted from the target payload mass. This difference became the mass to add to the upper section of LC_1 which represents part of the robot arm and provides a means of measuring F_{robot}. Summing components 1 through 11 and adding ½ of component 12, the total mass for $M_{top} \approx$ 17.22g (Appendix A, Table AI). The difference between M_{max} and $M_{top} \approx$ 9.28g. For simplicity and ease of modification, plastercine was used. Since the combined mass of the Robot_LS_Carriage_Mass and ½ of component 12 equalled 0.875 grams there is approximately 8.41g left. The plastercine mass was chosen to equal 6.75 grams.

The mass associated with measuring F_{robot} in the experiment and numerical simulation differ. Load Cell # 1 measures F_{robot} during the contact process and is dependant on the mass associated with: Plastercine_Mass, LC_1_Y02_Sensor_Mass Robot_LC_Couple_Clamps_Mass and the Robot_LC_Carriage_ Mass . In total, the mass supported by LC_1 equals 8.67g (see Appendix A, Section A.5). Relative to the lumped parameter arm model used in the numerical simulation, F_{robot} measures the

force generated by F_{Ktotal} and F_{Btotal} and is associated with M_{top}. The total mass associated with M_{top} = 24.8469g. These forces should be equal, however, the different masses prevent any degree of magnitude correlation. Mapping the two forces is accomplished through evaluating the mass ratio constant:

$$LC_{CF} = \frac{M_{top}(robot:NS)}{M_{top}(robot:LC)} = \frac{24.85g}{8.67g} \approx 2.87 \tag{21}$$

Therefore, to map the experiment with the numerical simulation LC_1's output must be multiplied by LC_{CF}. To map the numerical simulation to the experiment divide F_{robot}, in the numerical simulation, by LC_{CF}.

The high gains associated with the accelerometer, LC_1 and LC_2 sensors emphasize the robot arm's structural vibrations. Reducing these vibrations is accomplished through the use of six rubber discs mounted under the main support frame and two stabilizers. The six rubber discs provided isolation from external vibration sources. Both stabilizers aided in dampening internal vibrations. Stabilizer #1's location, illustrated in Figure 6, strategically forms a triangular frame support connecting the *Slider Guide* and the *Robot Arm*. During impact the bending moment effects created from the *Impact Surface-Rubber Tip* interface on the slider guide is reduced. Stabilizer #2 is illustrated in Figures 8 and 9. Beyond dampening the robot's vibrational modes its location prevents roll and yaw motions on the couple joining the *Robot Arm* to the motor shaft.

The rubber tip interface is mounted on the *Reflector Disk Assembly*. During contact, the tip experiences both axial and lateral forces which not only compresses but bends the tip. Reducing the axial play exhibited by the rubber tip during compression was accomplished by making the diameter of the tip ≈ 1.14 times greater than its length. Appendix B contains all relevant data and calculations pertaining to the rubber tip design. The mass is ≈ 0.0162 grams which is used in the numerical simulation.

Graphite was used to lubricate two sections of the direct drive arm. During compression, graphite between the spring, slider and slider guide maximized spring displacement. Contact between the rubber tip and impact surface also required lubrication. Initial tests, prior to lubrication, did not generate any spring compression and stopped the arm immediately upon impact with the impact surface. Graphite and low friction bearings provide a virtually friction free environment. The effective viscous damping was experimentally evaluated to be 0.115Ns/m through comparisons between a free fall experiment run and trial and error runs with the numerical simulation. It should be noted that after several experiments the graphite on the slider and impact surface had to be replenished.

It may be recalled that, the spring cannot go into tension due to the *Mechanical Stop* fixed to the spring slider guide.

3.4.2 Real-Time Software

Control of the direct drive arm is provided by an interrupt driven real-time DOS based program: *timer.c*. Generating the control interrupt vector by modifying the computer's *clock tick* cycle(standard 18.2ticks/sec) in conjunction with the standard C function *void interrupt far collect(void)*. This provides an accurate time stamp, Δt, which is necessary for multiplexed channel delay/signal reconstruction, integration, differentiation and feedback control.

The sampling rate is critical and chosen such that interrupt vectors do not overlap each other during both the five channel sampling sequence and control software execution. Optimization of the interrupt vector generation was based upon evaluating the time taken for one complete feedback cycle. There are nine major feedback control software components:

Table II: Direct-drive robot arm software control loop critical times.

index	Description	Time(μs)
1	Digital Filter array index offset	8.12
2	Collect Data	219.3
3	Multiplexed Channel Delay Correction	66.81
4	Digital Filtering	40.27
5	Interpret Sampled channel signals	52.31
6	Derived quantities	42.27
7	Contact phase evaluation (Varies)	5 - 35(max)
8	Derive B_p and K_p (Varies)	33.24(avg)
9	Output motor voltage	$\approx$10
total		507.32

These software routines occur consecutively and take approximately 0.507ms to execute one complete cycle. Based on this value the maximum sampling rate is $\approx$1971Hz. Since the execution time required to determine the current contact phase and evaluate B_p and K_p varies, the sample rate is chosen to be 1600Hz which allows 0.624ms-0.507ms = 0.1167ms of deviation. Due to the noninteger clock frequency, 1.1931817MHz, in conjunction with the 16 bits of counter resolution, the actual sampling rate is 1602Hz.

3.4.2.1 Multiplexed Channel Delay Correction

The numerical simulation control algorithm is based on the simultaneous sampling of all five sensors. This was also desired in the experiment. Since the K575 contains a single A/D converter chip the sampled sensors in the experimental

setup are multiplexed. Therefore, for proper control of the tip interaction it is required to reconstruct the channel signals to make not only the converter conversion time transparent but also the delay associated with channel selection.

The following three pieces of information are required for reconstructing the five channels to mimic simultaneous sampling: 1) Adjacent channel signal acquisition time delay(CH_delay), 2) Channel sampling rate(Δt), 3) Instantaneous magnitude time rate of change for each channel. Appendix D contains the details of correcting for the multiplexed channel delay.

3.4.3 Feedback Control Concept

The programmable damping, B_p, and spring, K_p, variables are implemented through a combination of hardware and software. Based on specified constraints, for example, current phase of contact, F_{robot} or the natural constraint imposed by the environment, both variables are evaluated in software and implemented by the actuator in real-time to accommodate the current task. Figure 10 illustrates the feedback control loop concept. Analog signal conditioning provides both differential inputs, sensor gains, analog filtering and signal conditioning circuitry for the five sensors. Electrical gain is depicted by G_e and is mathematically represented by ohm's law: $V_{in} = G_e I_a$. From the voltage controlled current source schematic in Appendix C, Figure C9, G_e is equal to 0.5. The direct-drive arm block contains two sub-blocks. They represent the arm's actuator and mechanical advantage, G_m. Since the motor is quasi-static its transfer function is based upon the torque equation described in Section 3.4.1.1. The gain of the robot, G_m, results from the torque equation: $T = F*L_{arm}$. Thus the desired force equation can be derived.

Software switching emphasize the option of turning on or off the force

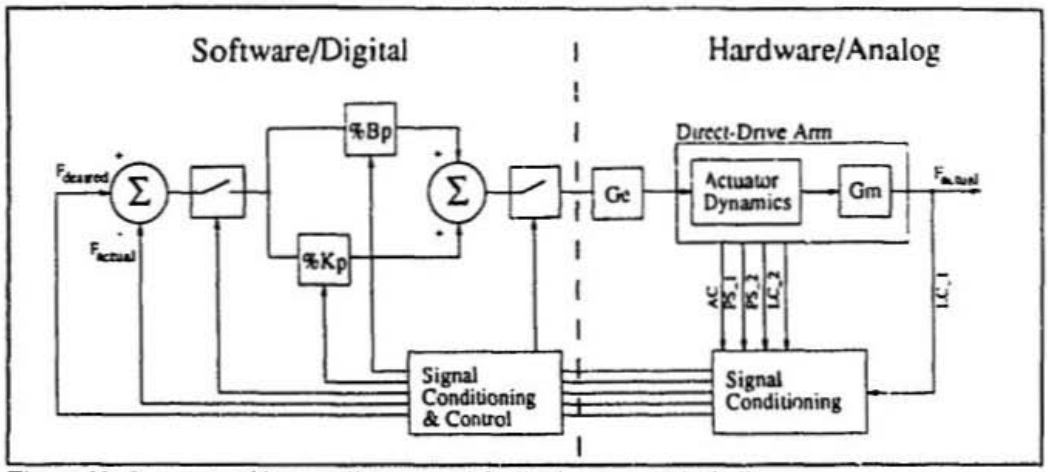

Figure 10: Programmable compliant control feedback concept block diagram.

feedback control and/or the programmable variables B_p and K_p. This allows constant coefficients for B_p and K_p to be implemented under no force constraint and opens venues for other control algorithms.

3.4.3.1 Impact and Recovery Phase flow charts

The two contact phases of interest during the investigation of the benefits of compliant environment interactions are the *Impact Phase* and the *Recovery Phase*. Figure 11 contains the software flow chart which is implemented during the Impact Phase. Figure 12 illustrates the software flow chart implemented during the Recovery Phase. These control algorithms are identical in both the numerical simulation and the direct-drive robot experiments.

Referring to Figure 11, once it has been established that the current phase of contact is Impact Phase, F_{robot} is determined. If this generated force is greater than the force limitations imposed upon the robot, F_{crit_robot}, then the correct damping and stiffness quantities are derived. These quantities are derived based upon equations 18 and 19. Both equation results are capable of preforming the contact process

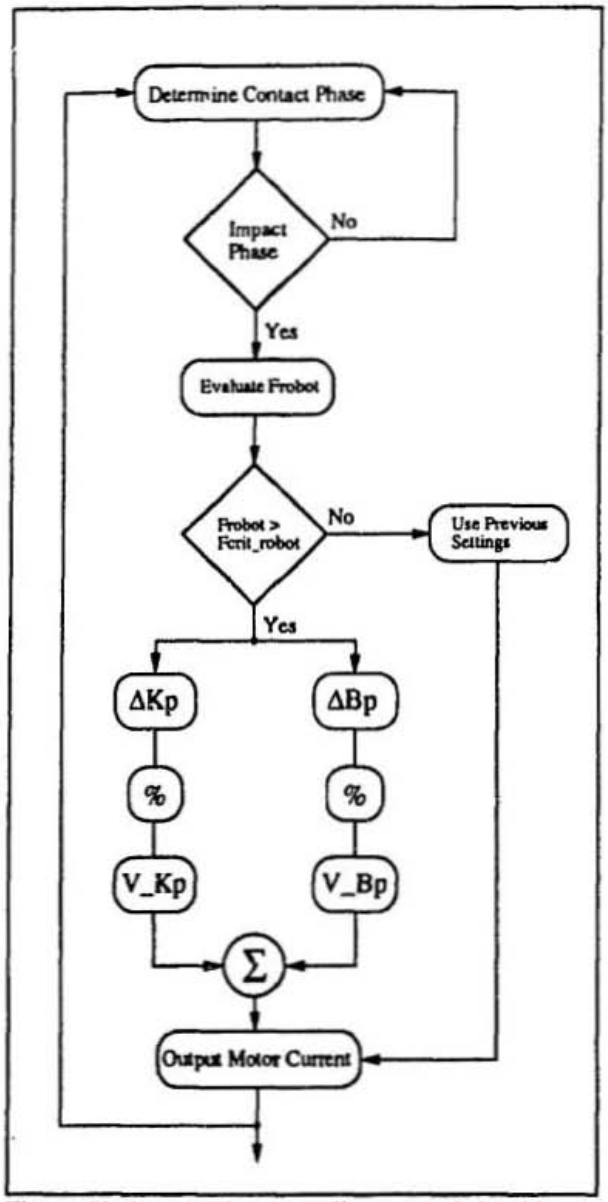

Figure 11: *Impact Phase* compliant control algorithm.

independent of the other. Since there exists current values for both these quantities from the previous integration, only the incremental amounts required to adjust the parameters to reflect the immediate demands of the contact process are determined. Based upon what percentage of damping and stiffness is desired, ΔKp and ΔBp are determined. This occurs prior to evaluating V_Kp and V_Bp. Once the desired damping and stiffness coefficients are derived they are converted in to a voltage. The voltage represents the input of the VCCS, hence the correct current is applied to reflect the contact force needs.

During the *Recovery Phase* it is desirable not only to impose the force restrictions on F_{robot} but also to minimize t_{settle} or maximize energy retrieval. The first conditional statement in Figure 12 reflects the same directives as described in the *Impact Phase* flow chart. Hence, the current discussion will focus on the implication of forcing the programmable damping coefficient to B_{crit} or using the programmable

stiffness coefficient to perform a desired task. During the compressive cycle of Impact Phase, the physical spring is a source of Potential Energy upon entering

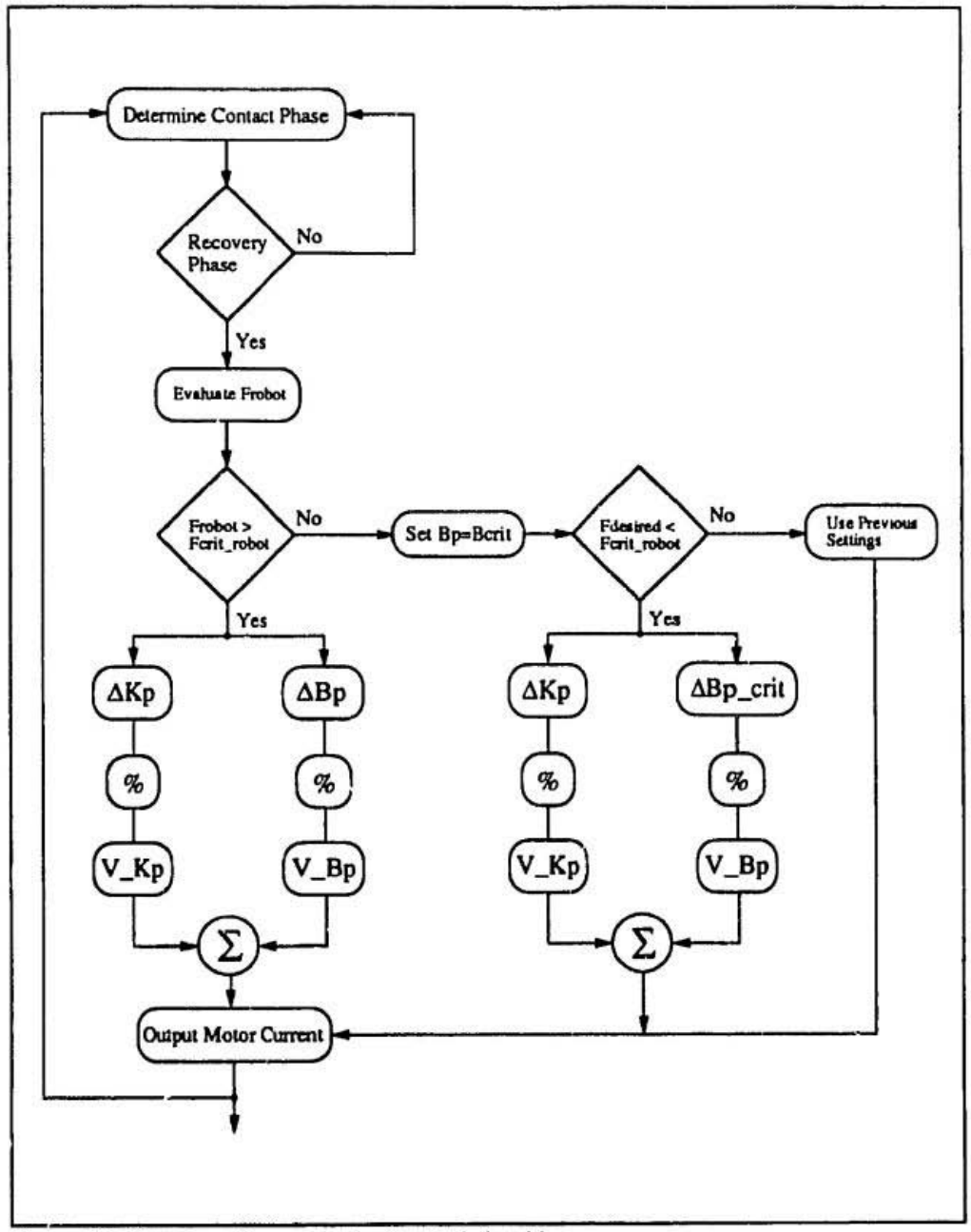

Figure 12: *Recovery Phase* compliant control algorithm.

Recovery Phase. After the force generated of the robot is under control and the first conditional statement is not violated, the robot actuator implements a desired force constraint. The programmable damping coefficient, B_p, is set to B_{crit} based upon the relationship: $B_{crit} = 2*\text{sqrt}(M_{top}*K_{total})$. Based on the instantaneous programmable

stiffness coefficient, B_{crit} can be adjusted to reflect current needs. During the transition between the first conditional statement and the second conditional statement the programmed compliant coefficients could cause a discontinuous magnitude jump. To avoid this impulse behaviour the new coefficient demands are incrementally changed based exactly on the method described in the *Impact Phase* flow chart discussion. If the desired contact process is to dissipate energy then B_{crit} is implemented. If the desire is to retrieve the potential energy then B_{crit} is turned off. Experiment I and II of Chapter 4 highlight these results.

3.5 Numerical and Experimental Model Comparison

This Section is separated into three main components: numerical simulation output, experiment output and a comparison. The goal is to familiarize the reader with the output variables of both sources of results and to illustrate the high degree of correlation between the two. The latter will help justify the confidence placed in both results when presented in Chapter 4.0.

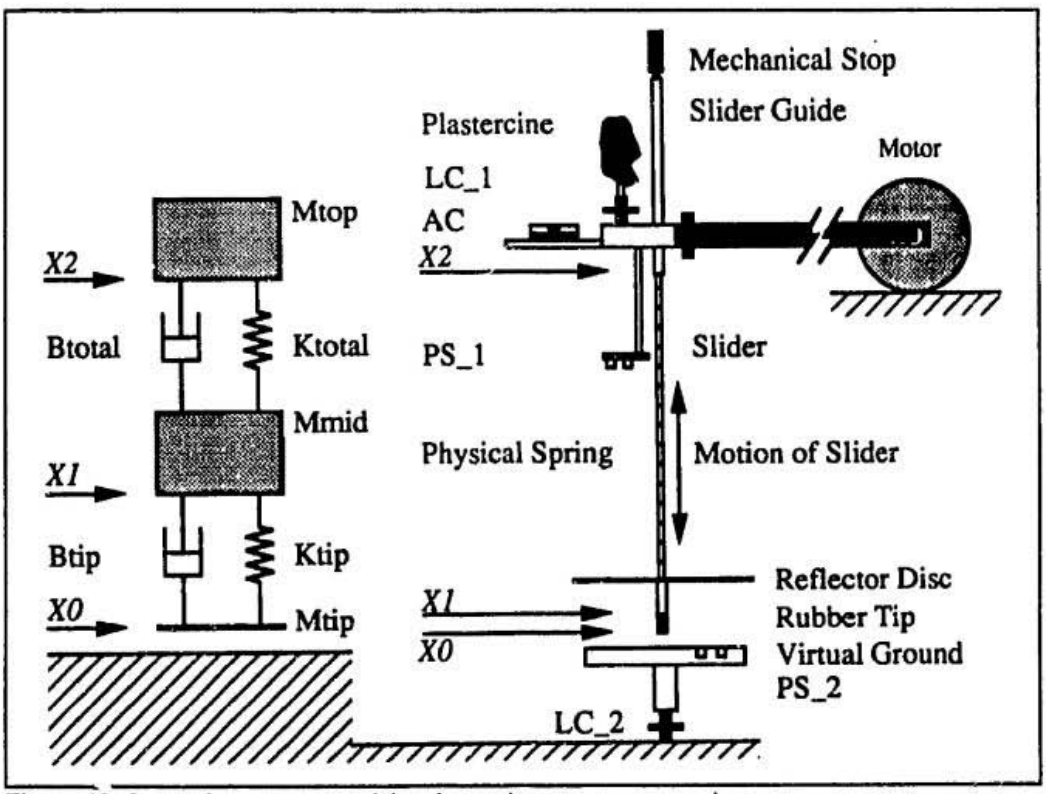

Figure 13: Lumped parameter model and experiment setup comparison.

Figure 13 illustrates and compares the robot arm experiment to the lumped parameter model used in the numerical simulation program. Correlation between each lumped mass, M_{top}, M_{mid} and M_{tip}, and the robot arm components associated with the three mass groups are described in Appendix A, Figure A1 and Table AI. State

Variables *X2*, *X1* and *X0* are mapped as indicated. Through integration and differentiation, velocity and acceleration information is realized.

For consistency, the robot is dropped from an effective height of 2.5cm in both the numerical and physical experiments. The term effective is a relative qualifier which highlights one of the most substantial differences between the numerical simulation model and the physical robot arm. Because the robot arm is a composite of displaced masses the centre of gravity is not situated directly above the robot tip (refer to Figure A2, Appendix A). Therefore, the 2.5cm drop must be relative the robot's centre of gravity and not the distance between the rubber tip and the impact surface. The derived distance that the robot arm tip must be dropped from is 2.703cm measured from the impact surface to the rubber tip. From the numerical simulation's perspective the distance is exactly 2.5cm measured from the environment interface to the rubber tip.

The experiments contained in this section contain no feedback control. The programmable damping, B_p, and spring, K_p, parameters are set to zero. The sensors and other parameters are simply measured and/or derived, under the influence of gravity, and evaluated for comparison. For the purpose of illustrating the current contact phase of the robot arm, the phases have been assigned the following numbers:

Table III: Contact Phase abstraction.

Contact Phase	abstraction
Pre-Contact Phase	0
Pre-Contact Critical	1
Impact Phase	2
Recovery Phase	3
Post-Contact Phase	4

The initial conditions are $V_o(t=0) = 0.0m/s$ and $X_o(t=0) = X_{init} = 0.025m$. During the following discussion, impact surface, environment and object are used interchangeably to refer to the surface upon which the robot arm makes contact.

3.5.1 Numerical Simulation Output

Displacement state variables *X2*, *X1* and *X0* are contained in Figure 14. Figure 15 illustrates the velocity state variables *V2*, *V1* and *V0*. Figure 16 illustrates the forces F_{robot}, and, F_{object} and Figure 17 the acceleration of M_{top}. Overlapping each plot is the instantaneous contact phase. Since the y-axis magnitude does not directly allow the Contact Phase numbering scheme of Table III to be used the scheme has been scaled, referenced at zero and are in the ascending order described.

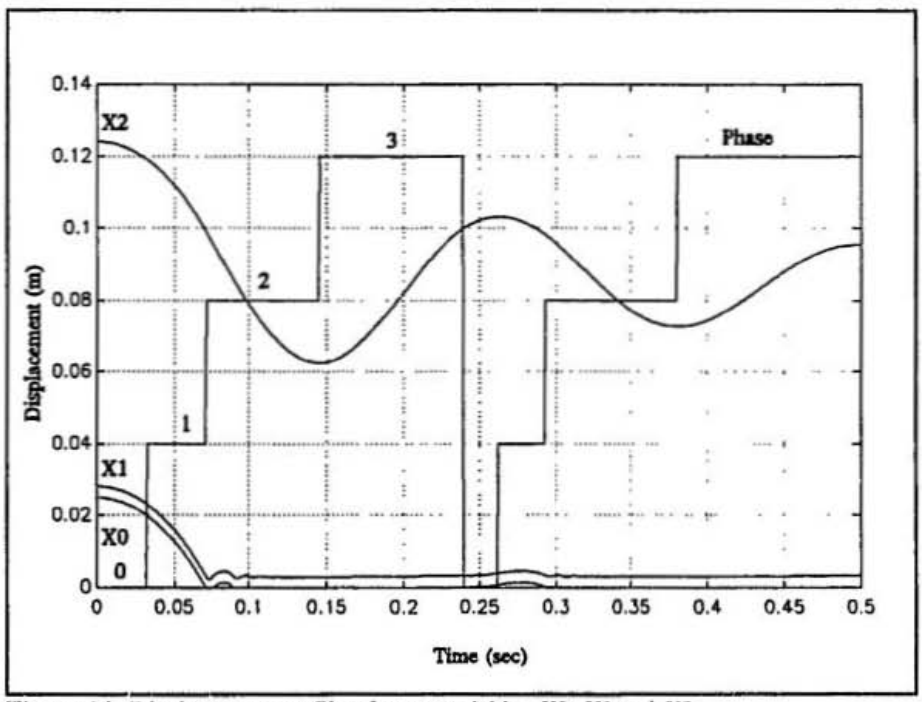

Figure 14: Displacement profile of state variables *X0*, *X1* and *X2*.

During free fall, immediately after release, the robot arm descends toward the

impact surface under the influence of gravity. The impact surface is represented by 0.0m and the current phase is Pre-Contact. From the acceleration curve a force of -1.0g is evident. Its constant magnitude results in the actuator experiencing a negative linear velocity profile. During both *Pre-Contact Phase* and *Pre-Contact Critical Phase* no external forces are imparted on the robot or the object, hence, F_{robot} and F_{object} are equal to zero. *Pre-Contact Critical Phase* is not of interest because preliminary contact calculations were not required in the experiment.

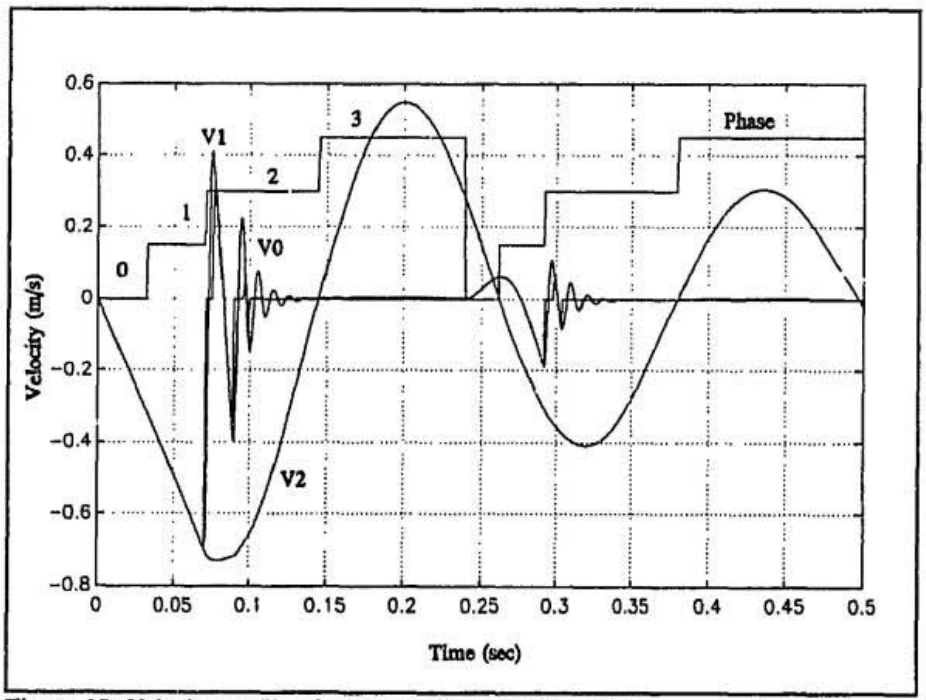

Figure 15: Velocity profile of state variables *V0*, *V1* and *V2*.

Impact occurs with the environment at $t_0 \approx 0.071392$s: *Impact Phase*. Clearly evident at this time is the Rubber tip bounce (see Figure 14) , the compression of *X2* begins and the initial impact force generated on the object, F_{object}, peaks at $\approx$ 1.908536N. The impact velocity is $\approx$ -0.700386m/s.

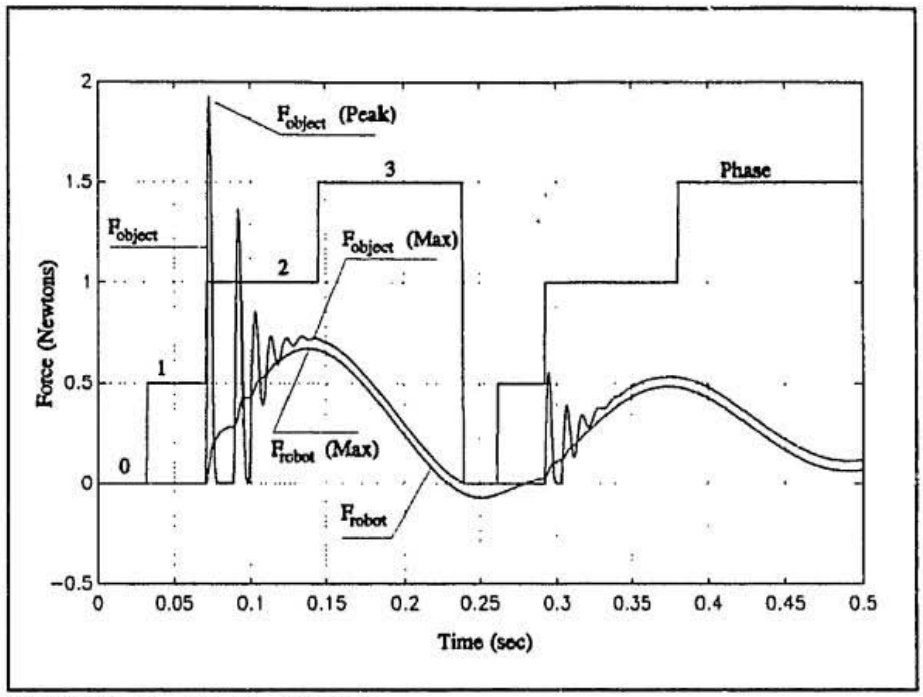

Figure 16: F_{robot} and F_{object} profiles.

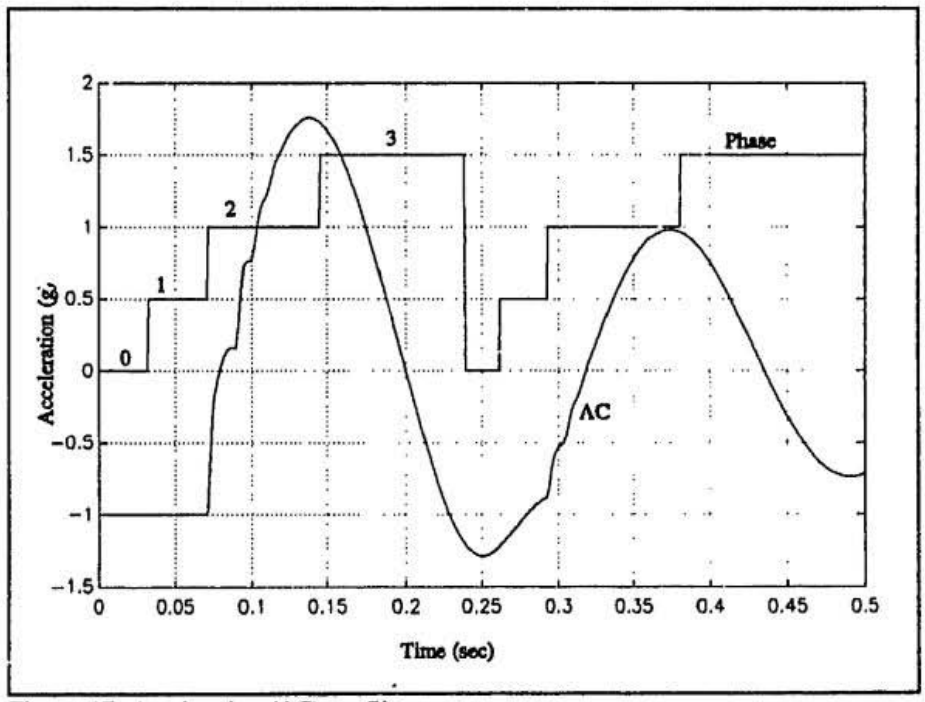

Figure 17: Acceleration (AC) profile.

At $t_1 \approx 0.14490$s, *Recovery Phase* is entered. Spring compression is maximum at this time and equals 0.059330m (0.062505m-Lo_{tip}). The rubber tip transient has decayed and the force generated on the object, F_{object}, peaks at $\approx$ 0.718073N. F_{robot} reaches at $\approx$ 0.665589N. The difference between F_{object} and F_{robot} results from the extra mass M_{mid} which the object must support.

Post-Contact Phase is never reached within the simulation time frame because of insufficient energy dissipation during the *Transitional Phases*, hence, the actuator bounces off the impact surface and re-enters *Pre-Contact Phase* ($t_b \approx 0.239418$s).

3.5.2 Experiment Output

Experiment two involves the robot arm. Figure 18 contains the output signal generated from the LC_2 and PS_2. It also contains two velocity signal representations of the *Actuator Jig Assembly*: Vtop_1 and Vtop_2. Velocity signal Vtop_1 is obtained by integrating the accelerometer signal and Vtop_2 is obtained from differentiating PS_1. Figure 19 contains the output signal generated from the accelerometer sensor(AC), LC_1 and PS_1. Proximity Sensor #1 has been shifted in magnitude such that 3.0 represents 9.6cm(lo_{spring}). Thus each increment on the y-axis scale represents 0.5cm. The Y-Axis is relative in its representation of the signal quantity. For example, in terms of signal AC the y-axis represents g's and for LC_1 it represents Newtons.

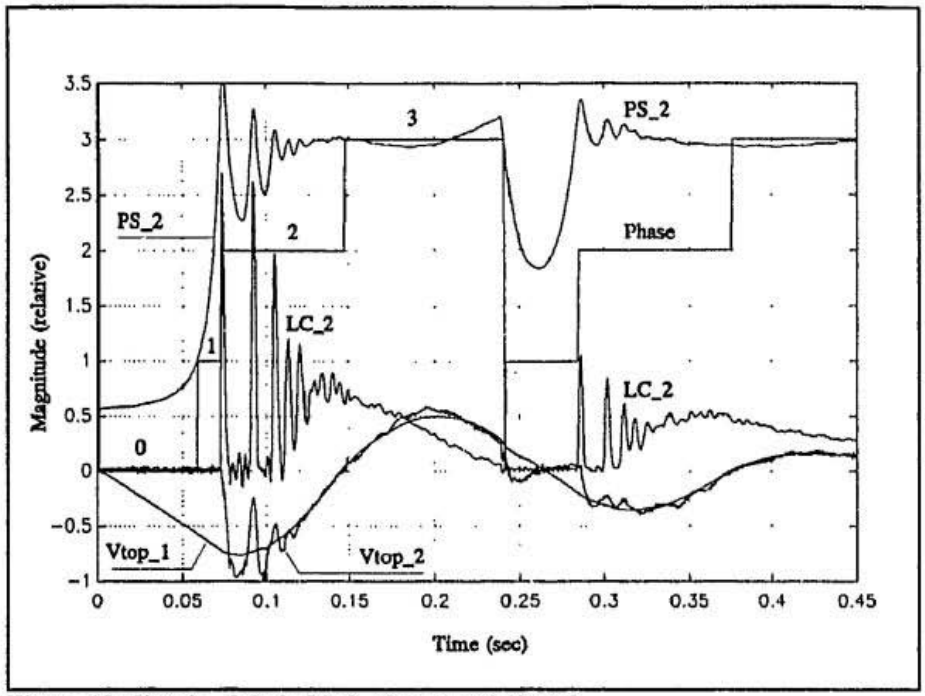

Figure 18: Signals - LC_2, PS_2, Vtop_1 and Vtop_2.

In a similar fashion, as in the numerical simulation output description, the experiment contact process is described. During free fall, the actuator descends toward the impact surface under the influence of gravity. The *Impact Surface* is represented by 0.0m and the current phase is Pre-Contact. From the acceleration curve a force of $\approx$ -1.25g's is evident. Refer to Appendix A Section A.4 for an analysis of this output. Its constant magnitude results in the actuator experiencing a linear velocity profile(see Vtop_1 in Figure 18). During both *Pre-Contact Phase* and *Pre-Contact Critical Phase* no force is imparted on the object, LC_2. The robot load cell, however, indicates a negative 0.115N force. Prior to release, the load cell output is calibrated to zero volts. Thus zero volts represents the force imparted upon the load cell by the plastercine mass and its support component masses (see Table AI in Appendix A components 12, 13 and 14). During free fall the load cell is in tension and thus the output voltage reflects this effect. Also, since the load cell supports the plastercine mass the LC_1 output is affected by tension and torsion effects. Refer to Appendix A Section A.5 for a detailed analysis of this output.

Impact occurs at $t_0 \approx 0.071473$s: *Impact Phase*. Clearly evident from PS_2 is the Rubber tip bounce (see Figure 18) , the compression of *X2* begins (PS_1 output Figure 19) and the initial impact force generated on the object, F_{object}, peaks at $\approx$ 2.79671N (see Figure 18 - LC_2). The impact velocity is $\approx$ -0.7112675m/s.

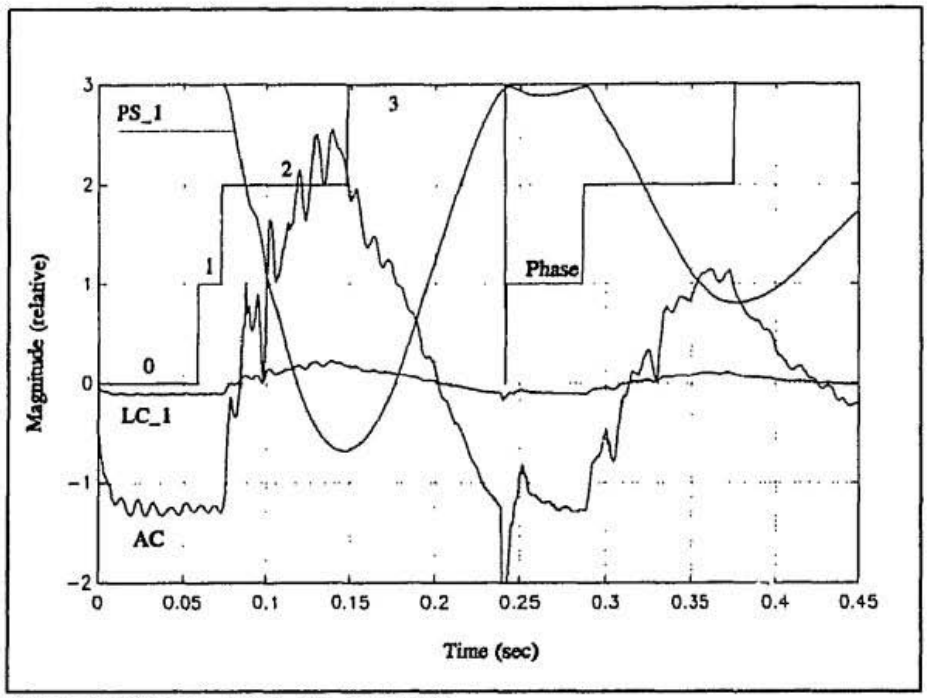

Figure 19: Signals - LC_1, PS_1 and AC.

At $t_1 \approx 0.14575$s, *Recovery Phase* is entered. Spring compression is maximum at this time and equals $\approx$ 0.735364m. The rubber tip transient has decayed and F_{object} (LC_2) peaks at $\approx$ 0.73N. F_{robot} peaks at a maximum magnitude of $\approx$ 0.6174287N (refer to equation 22).

Again, *Post-Contact Phase* is never reached within the experiment time frame because of insufficient energy dissipation during the *Transitional Phases*, hence, the actuator bounces off the impact surface and re-enters *Pre-Contact Phase* (t_b = 0.2362761s).

3.5.3 Comparison

The following five plots illustrate the high degree of correlation exhibited between the numerical simulation and the robot arm experiment. Figure 20 compares the velocity profiles of *V2*. Figure 21 compares the force generated on the robot. Figure 22 compares the acceleration profile. Figure 23 compares the force generated on the object. Figure 24 compares the displacement of the upper mass state variable, *X2*.

Table IV summarizes the results obtained from comparing critical points/parameters which were selectively picked from the five plots. The data is referenced to the direct-drive robot arm parameters and an example derivation is highlighted in Equation 23.

Table IV: Numerical simulation - direct-drive robot arm comparison.

index	Parameter Description	Numerical Simulation	Robot Arm Experiment	Percent Discrepancy
1	Impact: t_a(s)	0.071392	0.071473	0.113%
2	Recovery: t_r(s)	0.1449	0.14575	-0.583%
3	Bounce: t_b(s)	0.239418	0.2362761	-1.329%
4	Impact Velocity (m/s)	-0.700386	-0.7112675	1.529%
5	F_{robot} (Max)(N)	0.665589	0.616	-8.117%
6	F_{object} (Max)(N)	0.718073	0.73	1.634%
7	F_{object} (Peak)(N)	1.9139	2.79671	31.566%
8	G_{force} (Max)(g's)	1.730641	1.8	3.853%
9	X_{min} (normalized to lo_{spring})	0.061802	0.0735364	15.957%

Exact values for the parameters contained in the numerical simulation were obtained from the numerical simulation data files. Items 1, 2, 3 and 4 of the Robot Arm Experiment column are average values obtained from robot arm data files.

Because the sampling rate is 1602Hz, the exact values for these parameters occur between two successive samples, thus, an average magnitude is obtained and used in the data comparison table. Correlation is within ±5% for most of the parameters.

Parameter 8, G_{force}, in the robot arm column is an approximation of the exact value. Superimposed on the accelerometer signal are the vibrational modes of the robot (see Figure 19). The 1.8g value is obtained from drawing a line of best fit from an enlarged plot. A similar procedure is used to determine parameter 6.

Parameter 5, $F_{robot}(max)$, is derived from LC_1. This quantity has been corrected for free fall effects, centre of gravity/mount location effects and mass related effects . Measured from Figure 19's data file, $F_{robot}(max) \approx 0.223571$N. Using 95.96% of this magnitude (see Section A.5 of Appendix A) and correcting for the mass difference, LC_{CF} the corrected force, relative to the numerical simulation, is:

$$F_{robot}(max) = 0.223571 \times 0.9596 \times 2.87 \approx 0.616N \qquad (22)$$

which results in a discrepancy of:

$$\frac{0.616 - 0.666}{0.616} \approx -8.117\% \qquad (23)$$

The peak impact force generated on the object, parameter 6, does not show a high degree of correlation. The numerical simulation does not account for the slider guide/spring interface static friction and the rubber tip/impact surface static friction. Both of these frictions increase the impact force measured by LC_2. Also, the sampling rate is 1602Hz which may or may not sample exactly on the impact peak. Since this parameter is not directly used in the feedback algorithm, the discrepancy is acceptable. The generic, overall effects, however, show a high degree of correlation.

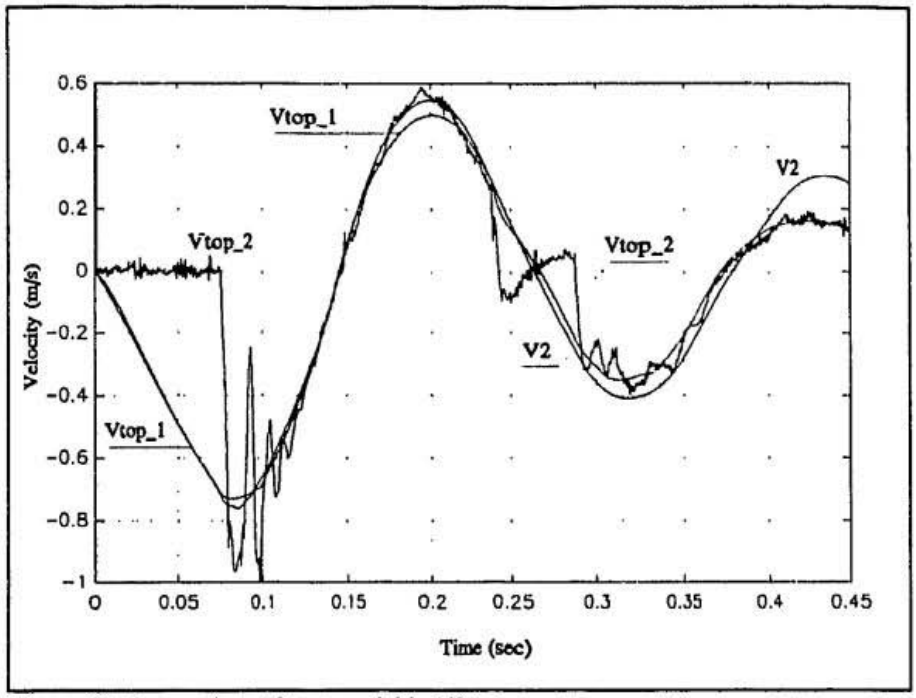

Figure 20: Comparison of state variable V2.

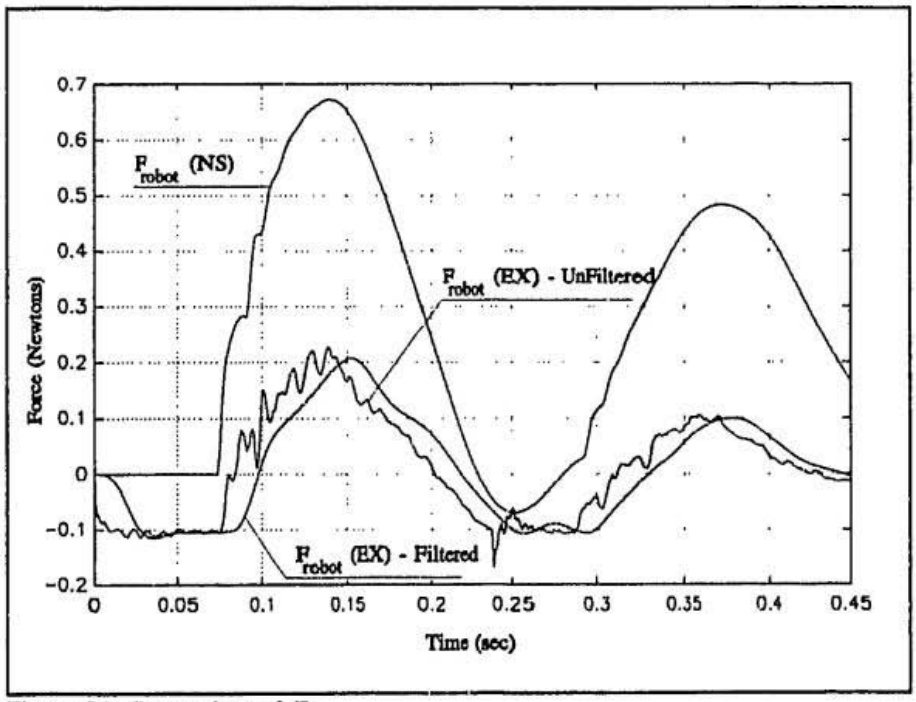

Figure 21: Comparison of F_{robot}.

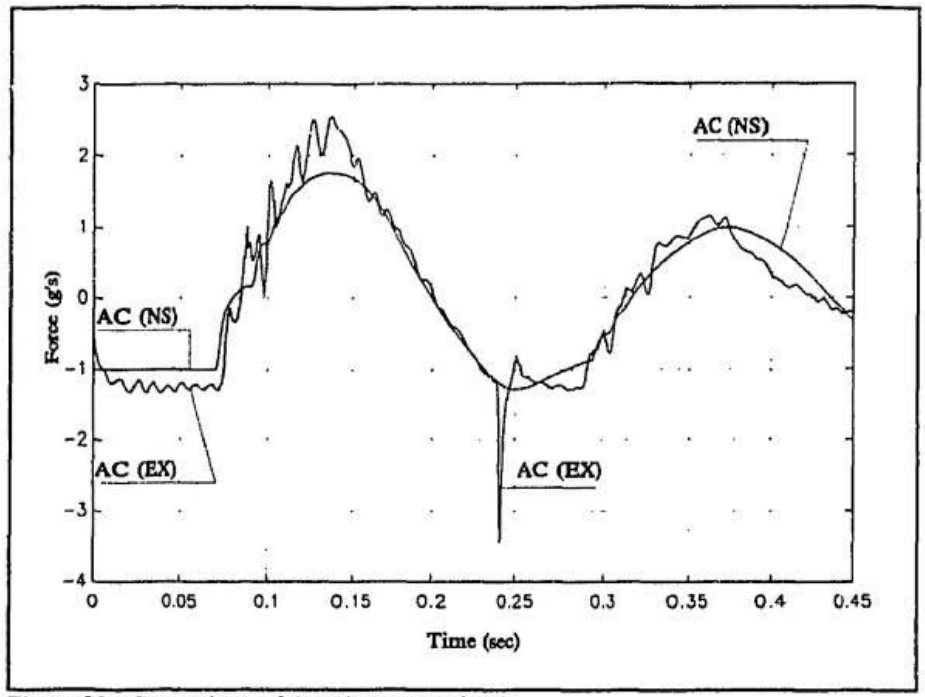

Figure 22: Comparison of Accelerometer signals.

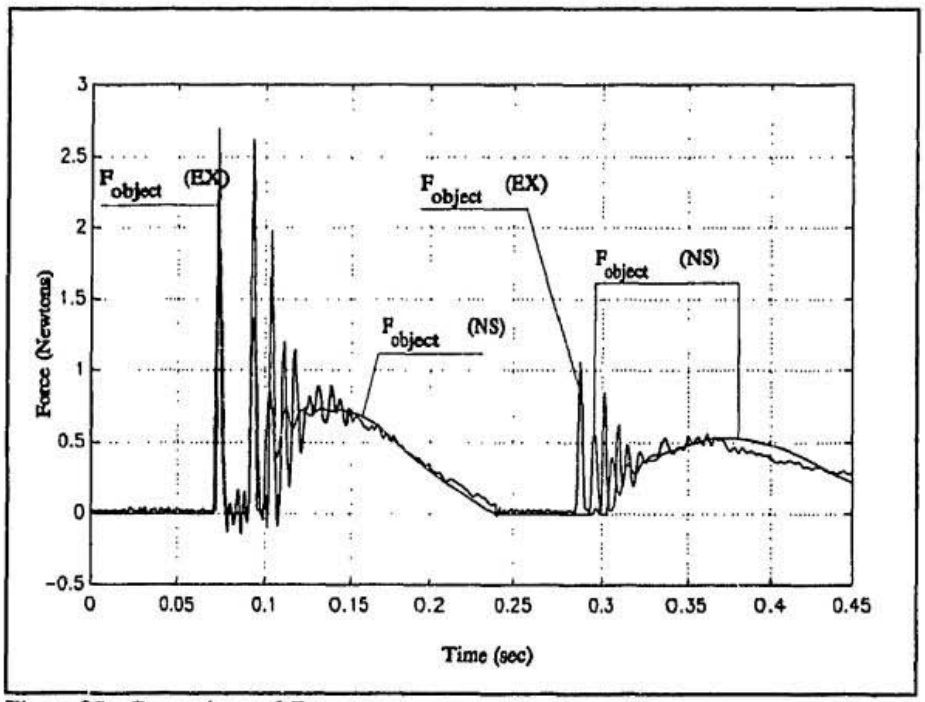

Figure 23: Comparison of F_{object}.

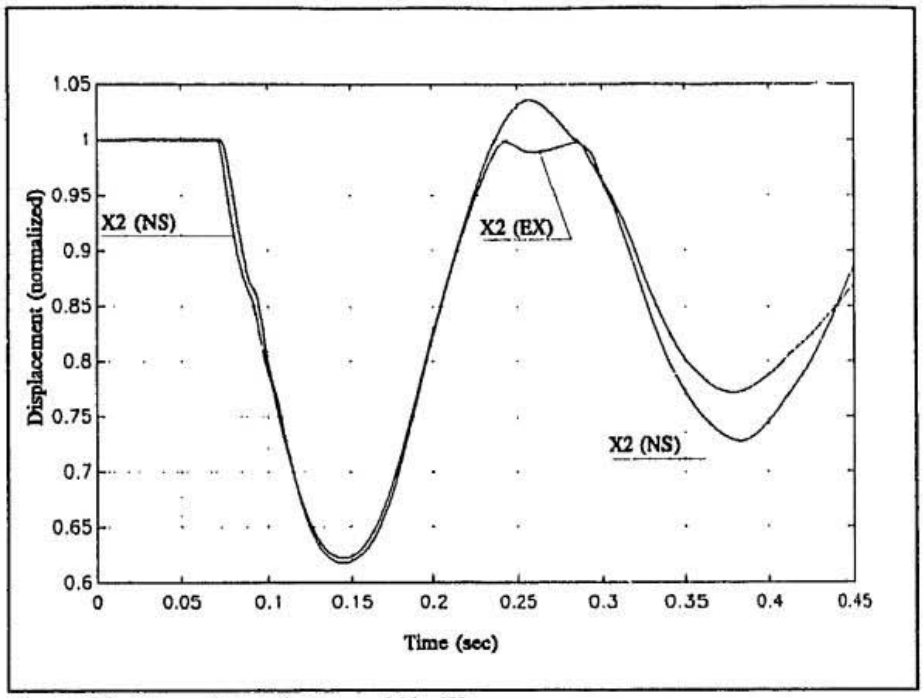

Figure 24: Comparison of state variable *X2*.

Chapter 4

4.0 Experiments

Investigating the individual and combined effects of altering the damping, B_{total}, and stiffness, K_{total}, parameters during the contact process is the focus of this chapter. The investigation is carried out on the numerical simulation setup and the robot setup. Initially, identical free fall experiments are conducted with both setups and compared. These results form a basis from which all other experiments are referenced. The second group of experiments deals with manipulating the effective damping and stiffness coefficients on the numerical simulation model and the Direct-Drive Robot(DDR_I) setup. The third group of experiments deals with manipulating the damping and stiffness coefficients on the Direct-Drive Robot(DDR_II) arm. The difference between experiments DDR_I and DDR_II is explained in the next paragraph. Finally, an advanced programmable damping equation is implemented in the numerical simulation during the *Recovery Phase*. This added damping further illustrates the benefits of strategically implementing damping and its ability to drastically minimize the contact settling time, t_{settle}.

Both Direct-Drive Robot experiments are identical, however, the power supplies used to energize the permanent magnet DC motor differ. Direct-Drive Robot

Arm Experiment I involves the use of a ±30v, ±2amp power supply. Direct-Drive Robot Arm Experiment II involves a ±60v, ±5amp power supply and F_{robot} is digitally filtered. Because the higher rated power supply is currently unavailable all final experiment results have been obtained using the lower rating supply. As a result, the newer experiments (Section 4.1) do not exhibit the expected high degree of correlation with the numerical simulation. They do however illustrate the concept. Including DDR_II results illustrate to a higher degree the potential of programmable compliance and proves that given the required power the concepts proposed by the thesis is achievable; however, one of the experiments is incomplete.

Identification of the programmable damping and programmable stiffness usage throughout the experimentation is facilitated using the nomenclature described in table V.

Table V: Experiment nomenclature.

Experiment #	Bp	Kp	Description
A	0	0	Both Bp and Kp turned off [No force constraint].
B	0	1	100% Programmable Stiffness.
C	1	0	100% Programmable Damping.
D	1	1	50% Programmable Damping and 50% Programmable Stiffness.

Throughout each experiment the same initial conditions are maintained. At t=0.0s, V_o = 0.0m/s and X_o = 1.5cm. The release height, X_o, is limited to 1.5cm because higher release heights simply impart greater demands upon the control algorithm. These higher demands do not further benefit an understanding of the contact process other than indicating that more power is required to preform the same task.

During the numerical simulation experiments F_{crit_robot} equals 0.35N and for the direct-drive robot experiments F_{crit_robot} equals 0.2N for DDR_I and 0.35N for DDR_II. The difference in the force magnitudes is based upon two reasons: power supply limitations and the measured force differences which exist between the two experiments. Section 3.4.1.3 describes the force difference of F_{robot} in more detail. In essence the LC_1 output measures the force on approximately 8.125grams whereas the numerical simulation measure the force generated by M_{top}. $M_{top} \approx 30g$, (see Table AI Appendix A). The different masses generate different forces. Thus difference is reflected in the magnitude of F_{crit_robot}.

Upon release, gravity forces the robot arm to descend towards the *Impact Surface*. Contact is eventually made and the robot comes to rest. Five variables are consistently used to describe the contact process: $X2$, $V2$, $A2$, F_{robot} and F_{object}. These variables are sufficient to describe the benefits of strategically implementing programmable compliance during the various contact phases. Plots of B_{total} and K_{total} are included where necessary.

Complete *Contact Phase* overlay plots are omitted from the experiment results. During each of the four experiments, Table V, the five contact phases, Table III, are encountered. Since the onset of each contact phase varies between the four experiment options it is extremely messy to include them.

4.1 Free Fall Experiments

As a means of comparison, free fall trial runs are included for both the numerical simulation and the robot experiment. These two free fall experiments are conducted under no contact force constraints - Experiment A(00). Therefore, B_p and K_p are turned off which implies $B_{total} = B_v + B_m$, $K_{total} = K_e$ and F_{max} = NULL.

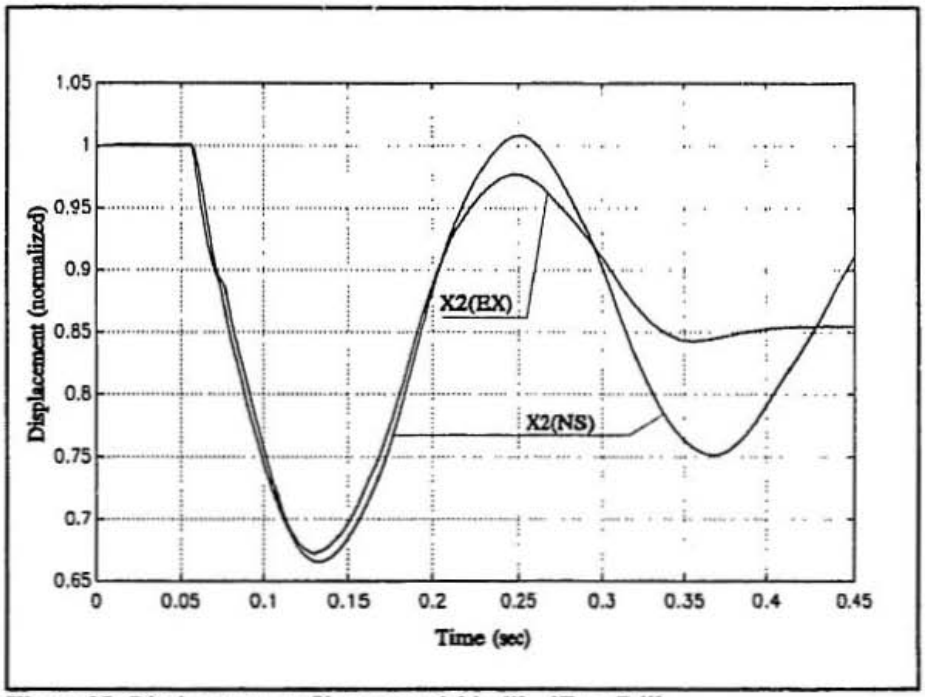

Figure 25: Displacement profile state variable *X2* - [Free Fall].

Figure 25 illustrates the displacement profile of the arm's upper platform, *X2* (see Figure 2, Section 3.2). Both signals are normalized. Signal X2(EX) represents the output of sensor PS_1 and signal X2(NS) represents the numerical simulation output. Compression begins at $\approx$ 0.054s. This represents impact between the environment and the Robot Tip. Maximum compression is $\approx$3.25cm and occurs at $\approx$0.13s. Towards the end of the experiment the numerical simulation continues oscillating whereas the direct-drive robot arm comes to rest. This highlights the

robot's friction effects which were not completely modelled in the numerical simulation. Also due to friction, X_{ss} ranges between ≈ 0.825 and ≈ 0.9(normalized) for the direct-drive arm. From the numerical simulation perspective, the upper platform will eventually come to rest at $X_{ss} \approx 0.86$(normalized).

Figure 26 illustrates the velocity profile of the upper platform, *V2*. One signal originates from the numerical simulation, *V2*, the other two are derived signals, one from integrating the accelerometer signal, Vtop_1, the other from differentiating X2(EX), Vtop_2. The process of differentiating inherently amplifies all signal dynamics. Also superimposed on Vtop_2 are the dynamics of the rubber tip bouncing off the *Impact Surface*. Upon impact Vtop_2 clearly indicates this interference. Finally, the impact velocity is $\approx$-0.54m/s.

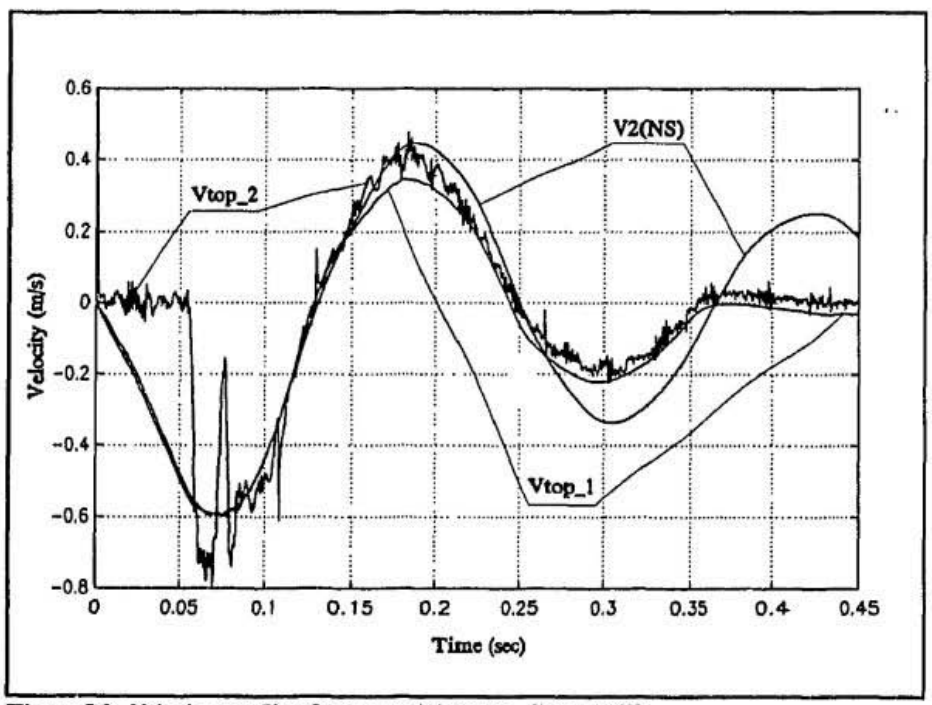

Figure 26: Velocity profile of state variable *V2* - [Free Fall].

Figure 27 illustrates the acceleration profile of the upper platform. The $\approx$ 110Hz fundamental vibrational mode of the direct-drive robot arm is clearly evident

on the accelerometer sensor signal, AC(EX). Upon impact, these modes are energized, however, as the contact process evolves the vibration decays. From the numerical simulation output, AC(NS), the rubber tip bounce upon impact is evident. This is illustrated by the rounded off step behaviour between t=0.05s and t=0.1s. During free fall, t<0.054s, the simulation robot model experiences -1g's. The direct-drive robot arm during this same window experiences ≈-1.25g's. At t>0.35s the friction associated with the physical robot forces the system to a stop.

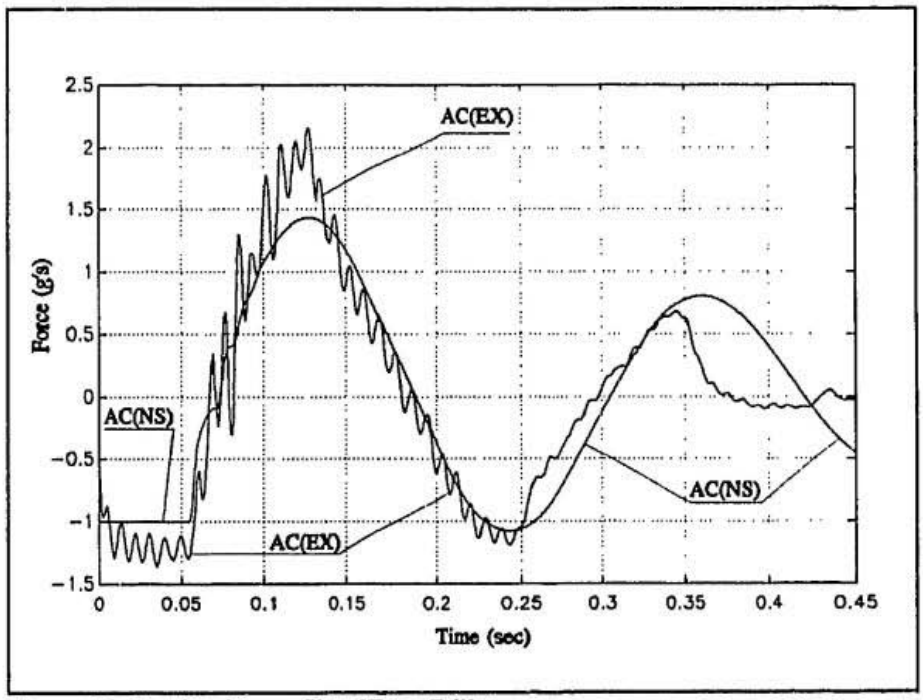

Figure 27: Acceleration profile - [Free Fall].

Figure 28 illustrates the forces generated on the robot, F_{robot}. Signal $F_{robot}(EX)$ is generated by LC_1 and has been adjusted using Equations 21 and 95.96% (see Appendix A, Section A.5). Recall from Section 3.4.1.3 that because the calibration of LC_1 is done prior to release, 0.0N represents the steady state supported mass. Upon release the load cell's output represents this mass. Consequently, a DC offset of 0.3N approximately maps $F_{robot}(EX)$ with $F_{robot}(NS)$. The vibrational modes of the robot are clearly evident on the experiment signal. As with the effects of the rubber

tip bounce superimposed on the accelerometer signal, the load cell also indicates this effect. F_{robot}(max) is $\approx$0.6 Newtons.

Finally, Figure 29 illustrates the force profile generated on both the environment and the robot tip, F_{object}. The transient magnitude spikes between t$\approx$0.054-0.0125s represent the rubber tip bounce. $F_{object}(max)$ is approximately 0.65 Newtons.

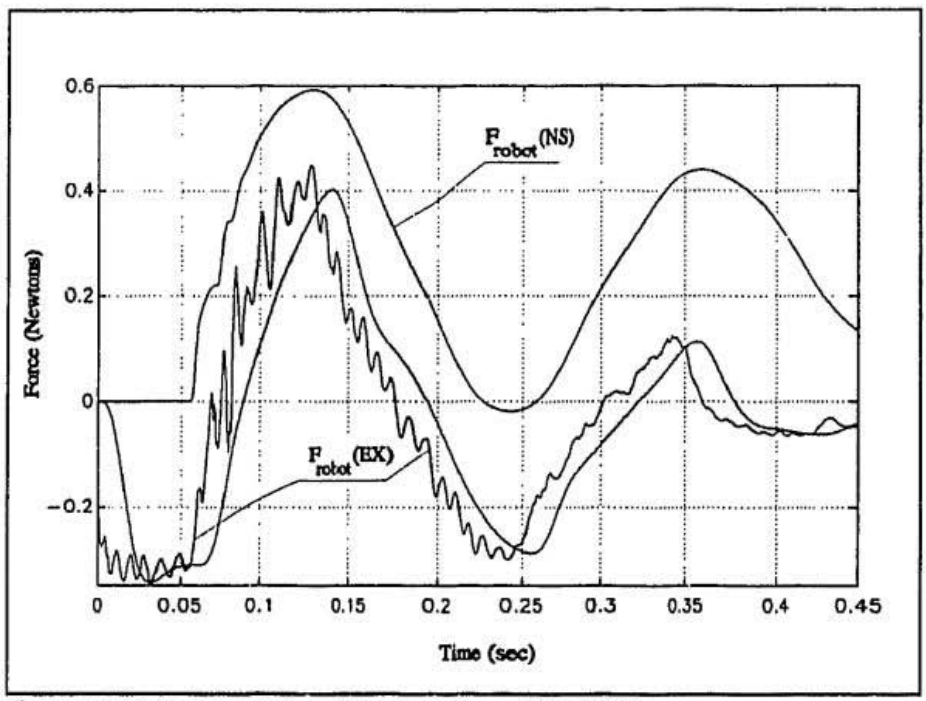

Figure 28: Force generated on the robot, F_{robot} - [Free Fall].

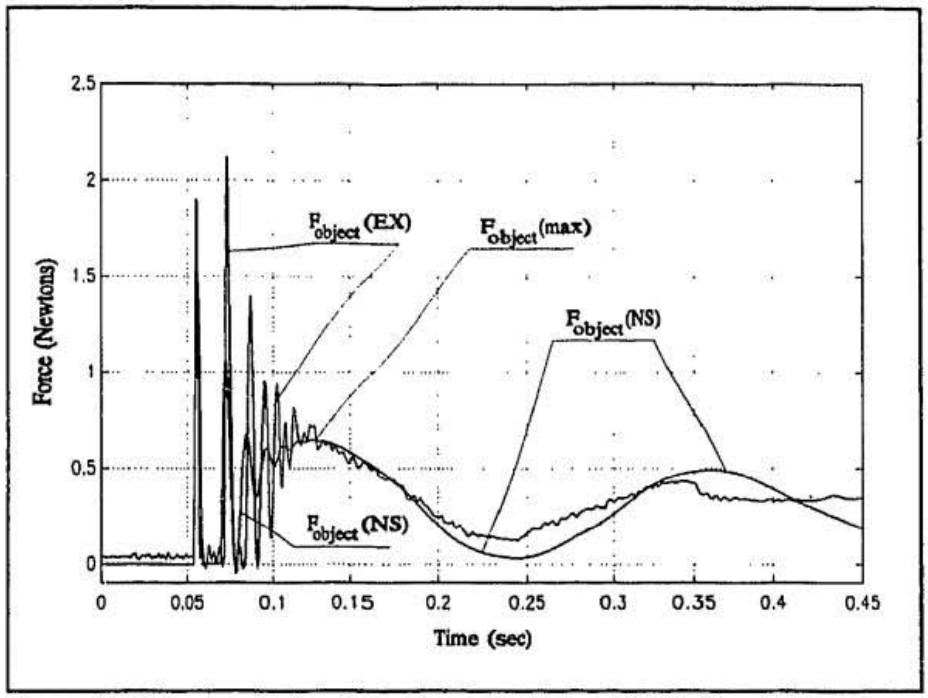

Figure 29: Force generated on the environment, F_{object} - [Free Fall].

4.2 Programmable Compliant Experiment Results

Both the numerical and robot experiments are described and compared in this section. There are four experiments conducted with each setup: Table V describes each. The four numerical simulation experiments contained in this section have been conducted under ideal conditions. The conditions are ideal in the sense that robot dynamics, external vibrations, sensor integration, sensor differentiation, power supply switching noise and incandescent light interference, to name a few, have been excluded from the simulated contact process. Based on the high degree of correlation between the free fall experiments of the numerical simulation and the robot, given in Sections 3.5.3 and 4.1, these experiments indicate what should be expected from both Direct-Drive Robot Arm experiments (DDR_I and DDR_II) under ideal conditions.

4.2.1 Experiment I

To accommodate the imposed force constraint, the physical spring is forced to compress. This is a result of two phenomena. First of all, during the compressive nature of Impact Phase F_{robot} increases. When this generated force exceeds F_{crit_robot} the effective spring constant decreases to accommodate the constraint. Consequently, the mass supported by the spring, M_{top}, forces the compression. Second of all, negative damping imparts a compressive force upon the spring. This effect is illustrated in both the numerical simulation experiments, Figure 30, and the robot experiments, Figure 31, signals X2(10), X2(01) and X2(11). With reference to the numerical simulation experiments, maximum compression is reached at ≈ 0.2 and equals ≈ 0.42. During *Recovery Phase*, experiments, X2(10) & X2(11), are forced to X_{ss}. This is a result of the programmable damping dissipating the compressed spring's stored energy. In signal X2(01) the damping effects are turned off resulting in the numerical robot model jumping off the impact surface. This is illustrated by

the normalized X2(10) signal attaining a magnitude greater than one.

The robot experiment, Figure 31, gave similar results. The differences associated with the experiments are a combination of unmodelled friction effects and inadequate motor torque(power supply related). Maximum compression is reached at ≈ 0.14s and equals ≈ 0.58. During *Recovery Phase*, experiments, X2(10) & X2(11) quickly approach X_{ss}. Again, this is a result of the programmable damping dissipating the spring's stored energy. In signal X2(01) the damping effects are turned off resulting in the robot reaching a steady state displacement of ≈ 0.88. Due to inadequate spring compression, X2(01) did not jump off the impact surface as illustrated in the numerical simulation. The inadequate spring compression is the result of power supply limitations. Toward the end of the experiment the unstable behaviour exhibited by signal X2(11) is a result of the compressed spring attempting to reach a more suitable steady state position.

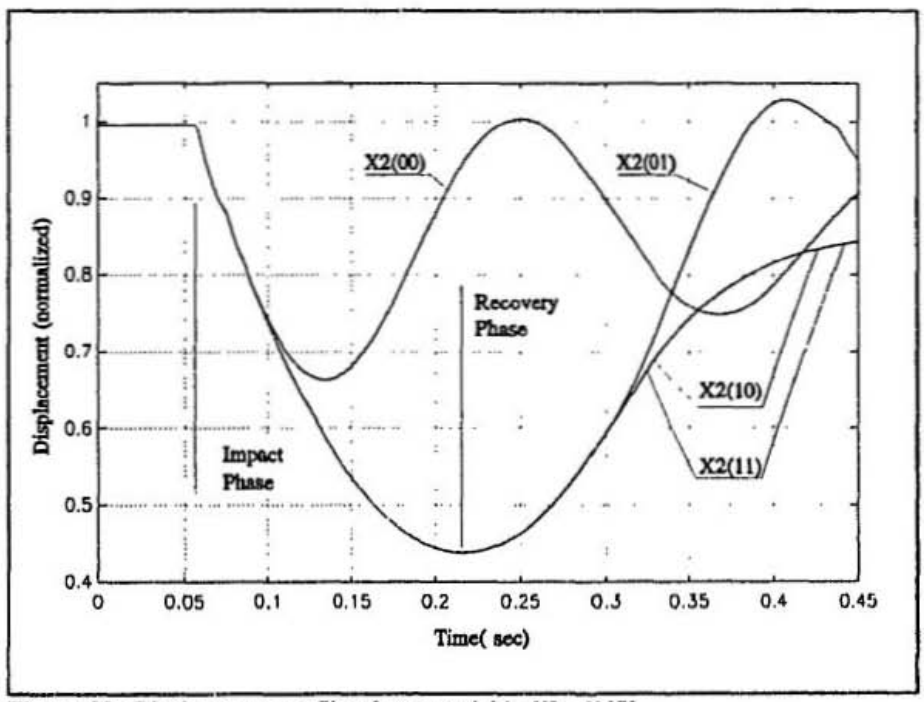

Figure 30: Displacement profile of state variable *X2* - [NS].

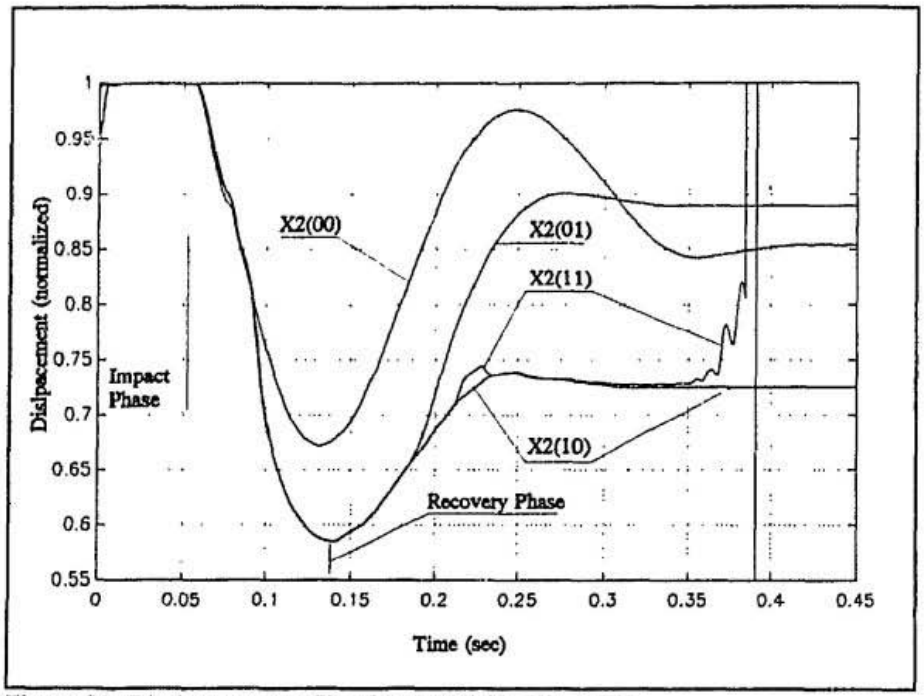

Figure 31: Displacement profile of state variable *X2* - [EX].

From the numerical simulation velocity plot of *V2*, Figure 32, it is clear that the imposed force constraint produces a linear velocity profile. Experiments V2(10) and V2(11) tend toward 0.0m/s after the robot model ceases to violate F_{max}, $t \approx 0.29$s. V2(01), however, violates the force constraint for approximately 0.05s longer. This is a result of the spring's inability to dissipate any of the impact energy.

Figures 33 and 34 illustrate Vtop_1 and Vtop_2 respectively. Because the two velocities are derived from two different sensors, the profiles are quite different. A detailed discussion of these differences is contained in Section 3.5.2 and in this Section. In comparing the three velocity plots it is clear that only the numerical simulation experiment velocity profile is linear during the violation of F_{crit_robot}. At $t \approx 0.08$s experiments (10), (01) and (11), Figure 33, indicate linearized velocity profiles. Due to motor current limitations the force constraint is acheived for approximately 0.0125s and then deteriorates due the increased demands upon the robot during contact.

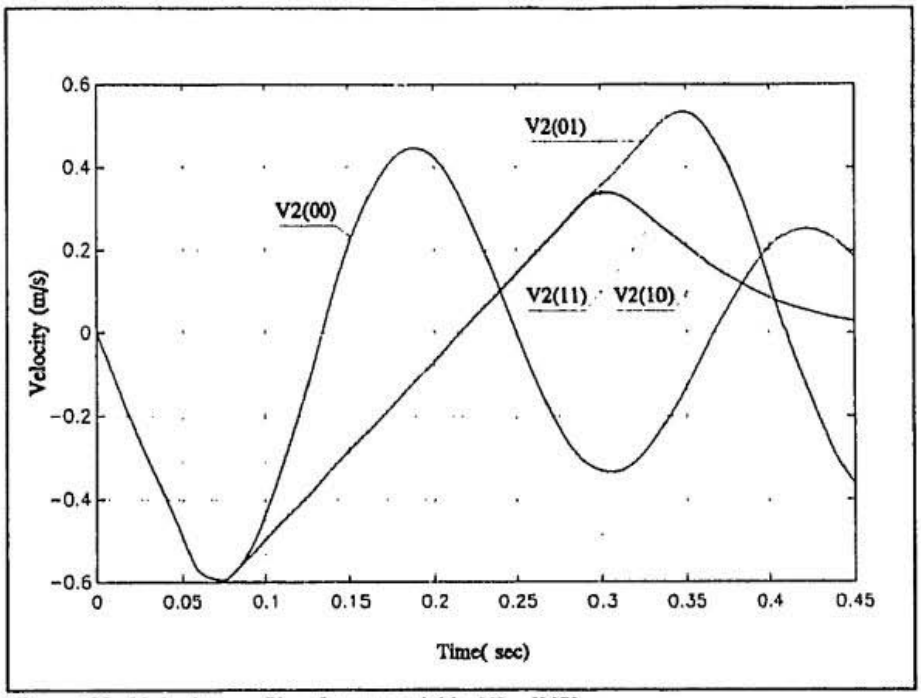

Figure 32: Velocity profile of state variable *V2* - [NS].

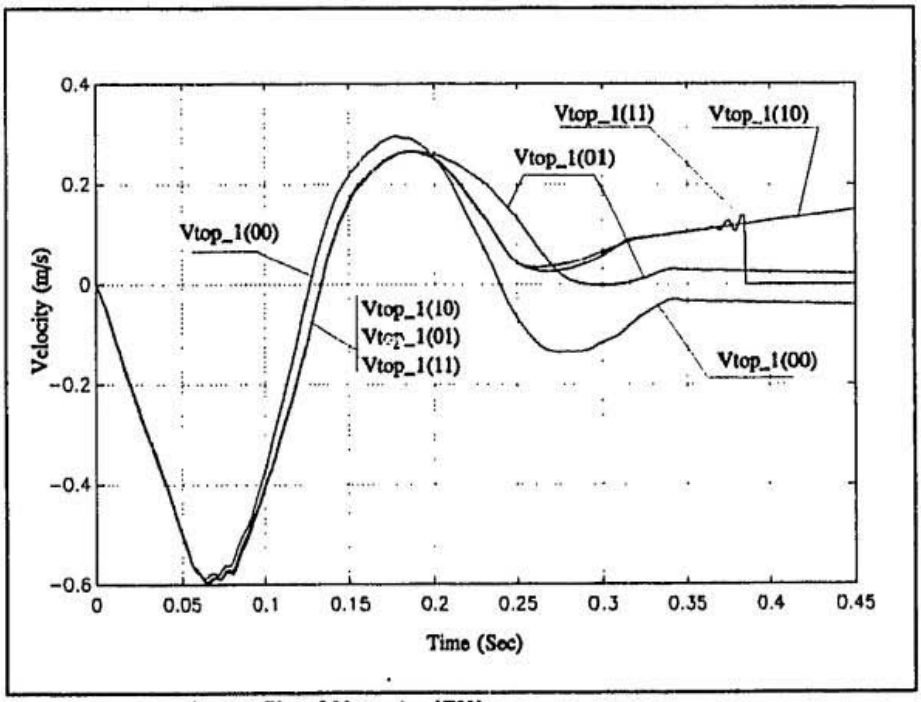

Figure 33: Velocity profile of Vtop_1 - [EX].

Consider the velocity curve generated by integrating the accelerometer signal, Vtop_1. For $t > 0.3s$ Figure 33 indicated that all four experiments have not converged to 0.0m/s even though the displacement plots indicate otherwise. Integration is a summation procedure. The accumulated error is a result of the accelerometer's orientation during free fall and a result of undersampling. As the robot arm is raised and positioned for release on the *Solenoid Release Mechanism* the accelerometer becomes tilted. Since the device is unidirectional any angle reduces the sensor output. This produces an erroneous signal which is amplified through the

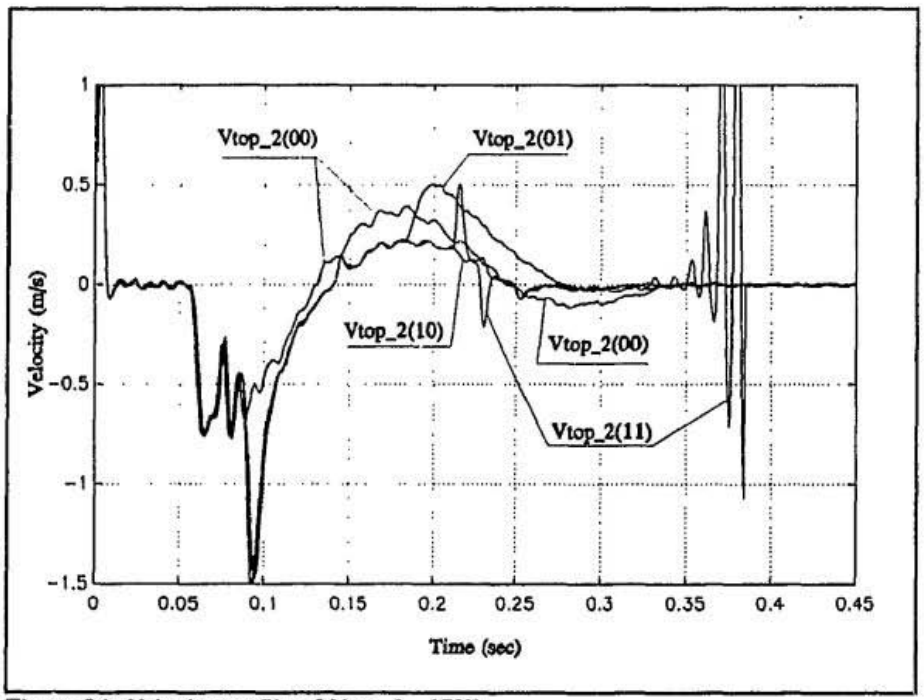

Figure 34: Velocity profile of Vtop_2 - [EX].

integration procedure. Even though the sampling rate used in the robot experiment, $fs = 1602Hz$, is adequate for the required accelerometer bandwidth, the high frequency noise generated by the motor reactive forces, the robot's modes of vibration and the impact created upon contact demand a higher sampling rate.

Consider the velocity curve generated by differentiating PS_1, Vtop_2. For

t>0.3s Figure 34 indicated that all four experiments converge at 0.0m/s. The sensor and hence the derived velocity strictly depend upon instantaneous motion. The robot is at rest after this time period which results in the indicated output.

Note the oscillatory behaviour toward the end of the experiment, t>0.32s, of velocity profiles Vtop_1 and Vtop_2. Again, as for *X2*, this behaviour is a result of the compressed spring attempting to reach X_{ss}. This unstable behaviour can be seen in all the robot experiment plots and thus will be omitted during further discussion.

Figure 35 and 36 portray the acceleration profile of the upper platform. As the force constraint is violated, t≈0.08s, the compliant control algorithms force a constant acceleration. Maintaining F_{robot} at F_{crit_robot} ultimately imposes a similar acceleration response, a constant acceleration profile. The damping effects associated with experiments (10) and (11) in both NS and EX quickly bring the accelerometer signal to zero. Based on the ideal conditions of the numerical simulation signal AC(00) continues to evolve, however, the robot experiment accelerometer signal decays. This is a result of contact friction.

Based upon the location of the accelerometer sensor and LC_1 and also because both sensors are force measuring devices their profiles should be almost identical. Thus the force generated on the robot, F_{robot}, should be a scaled version of the acceleration profile. Comparing the acceleration and F_{robot} profiles, Figures 35 and 37 and Figures 36 and 38, confirms the idea.

Referring to Figure 36, the cropped accelerometer signal, t>0.08s, is a result of the imposed force constraint. Referring to Figure 38, the cropped F_{robot} signal is well defined. Inadequate motor current prevented a more defined crop in both instances.

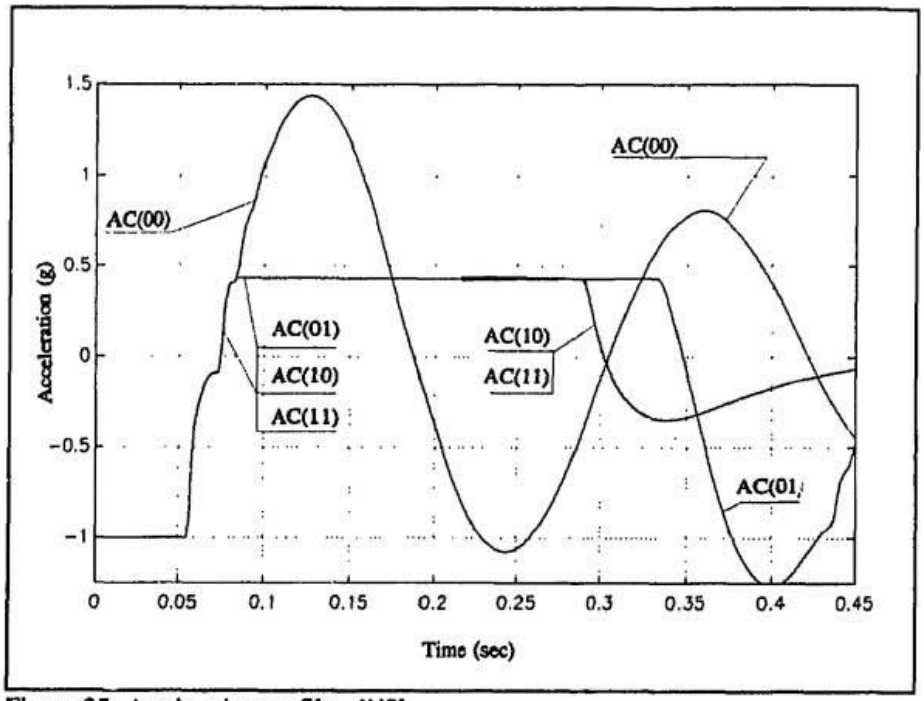

Figure 35: Acceleration profile - [NS].

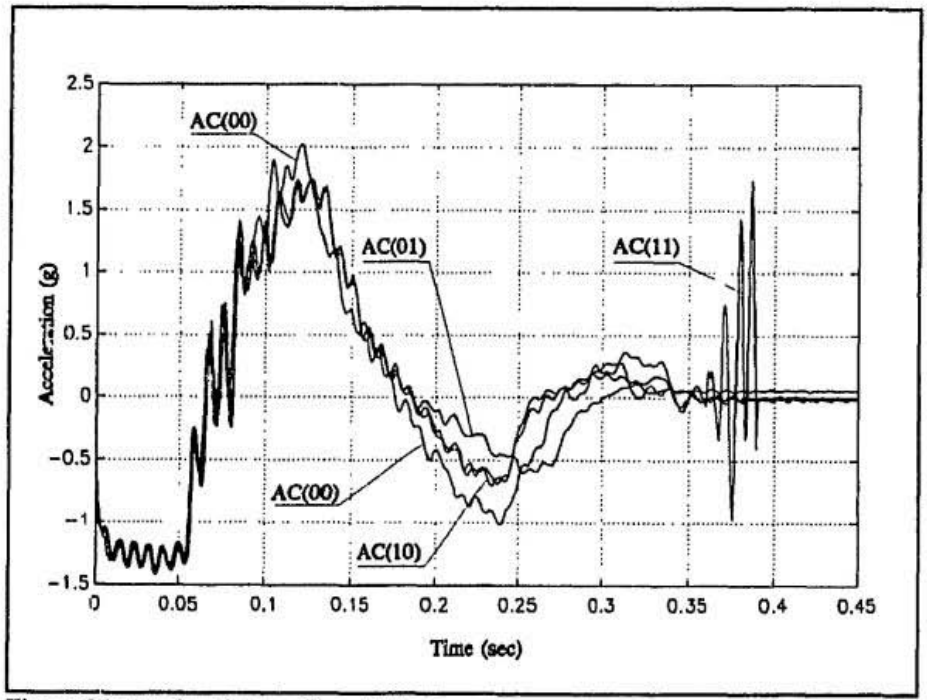

Figure 36: Acceleration profile - [EX].

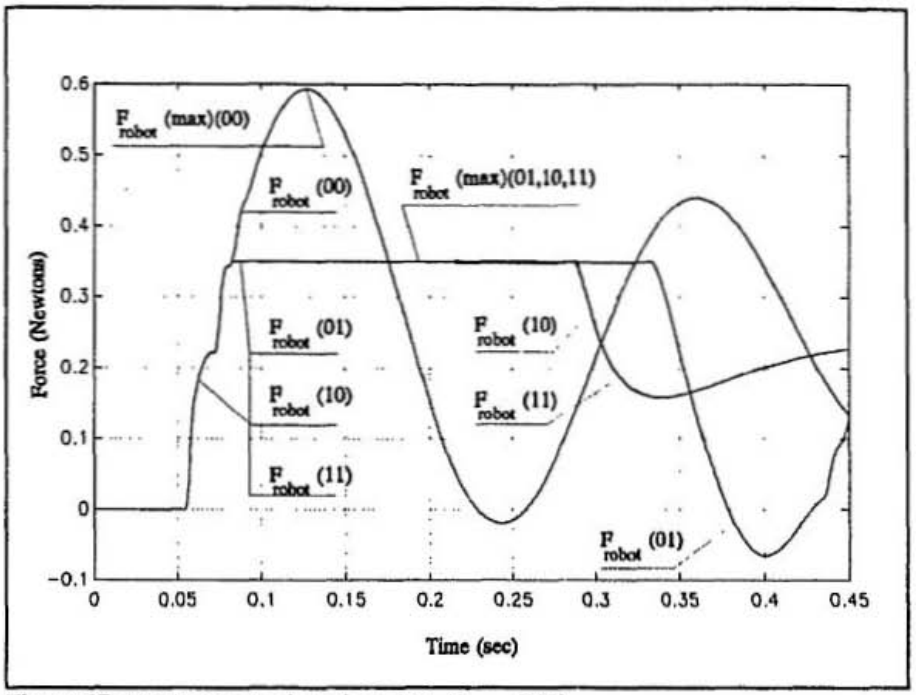

Figure 37: Force generated on the robot, F_{robot} - [NS].

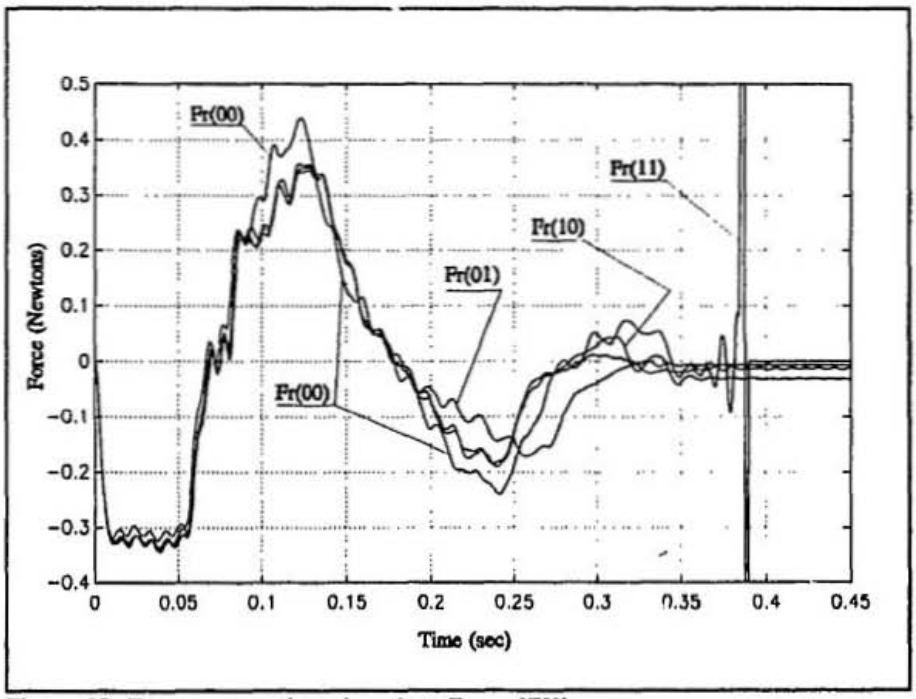

Figure 38: Force generated on the robot, F_{robot} - [EX].

The imposed force constraint also affects the force generated on the environment, F_{object}. Figure 39 illustrates F_{object} during the four numerical experiments. Upon impact, $t \approx 0.054$s, all four experiments indicate identical impulse spikes. Even though F_{object} exceeds F_{crit_robot}(0.35N) the control algorithm is responding to F_{robot} not F_{object}. Thus, F_{object} is a consequence of the force constraint imposed on F_{robot}. Once F_{crit_robot} is exceeded, F_{object} oscillates and eventually stabilizes at ≈ 0.4N. When the force constraint is removed and steady state conditions prevail, F_{object} measures the gravitational induced forces on M_{total}. It is interesting to note that at ≈ 0.358s the robot tip leaves the environment and rebounces at ≈ 0.44s.

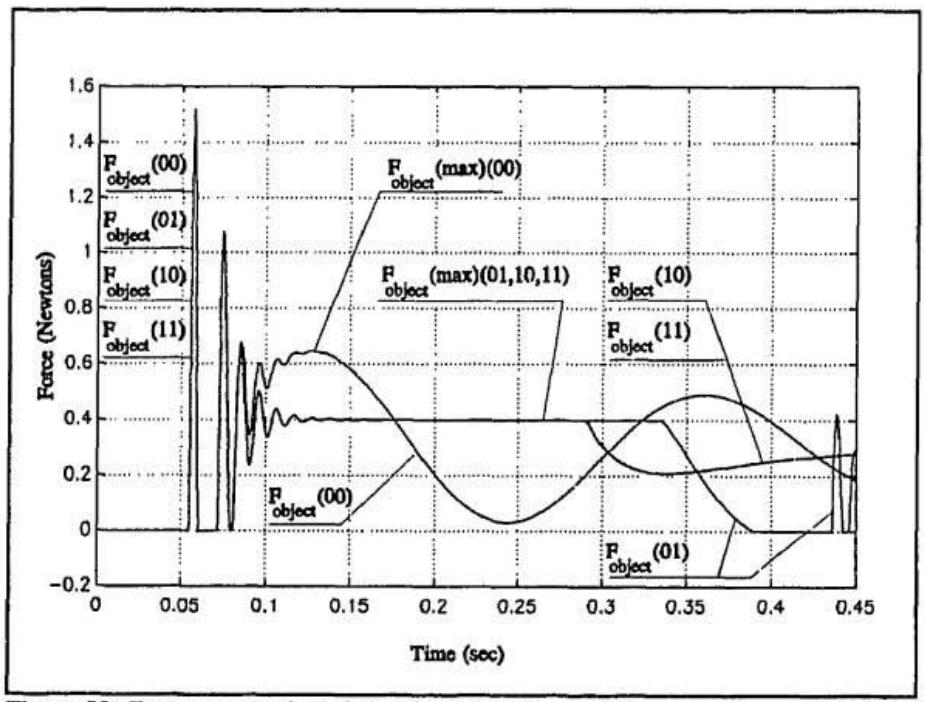

Figure 39: Force generated on the environment, F_{object} - [NS].

The robot experimental results, Figure 40, do not indicate the same response during the contact process. A close examination of the physical setup, Figures 5,6 and 7, reveals why. Force control is provided through the motor which is in turn connected to the upper platform. Only the sensors mounted here are affected by the control algorithm. Load Cell #2, F_{object}, measures the spring force during the contact process. The physical spring constant, K_c, does not change from LC_2's perspective but in a pseudo fashion changes from the robot's perspective. This is why, LC_2's output is actually greater than the free fall maximum force.

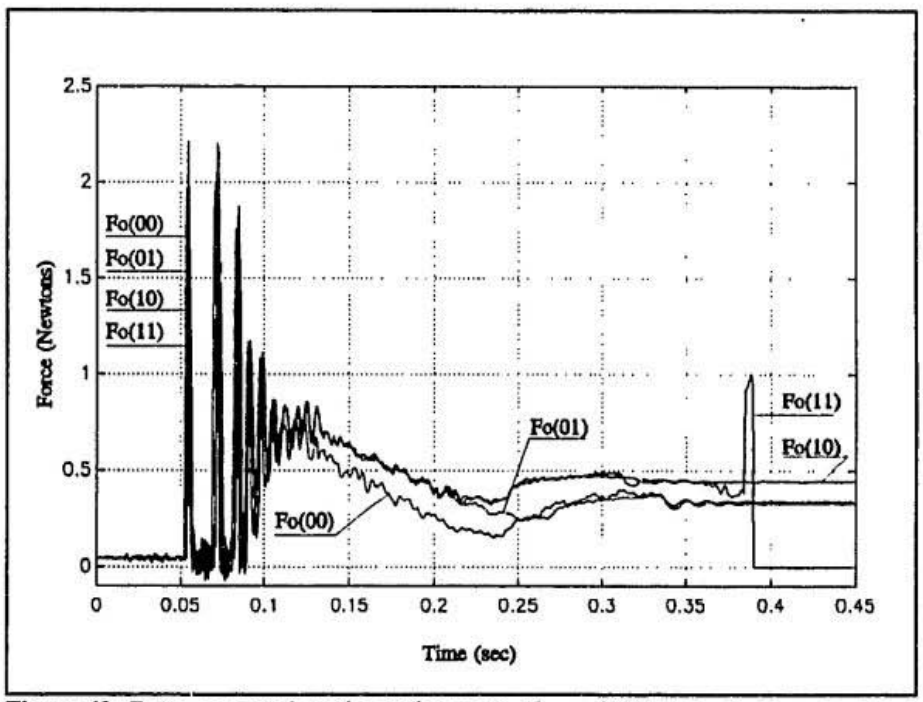

Figure 40: Force generated on the environment, F_{object} - [EX].

Figures 41 and 43 illustrate the influence of programmable damping and stiffness coefficients in the numerical experiment. Figures 42 and 44 illustrate the influence of programmable damping and stiffness coefficients in the robot experiment. For experiment one, in each caes, B(00) and K(00), B_p and K_p were set to zero. Therefore, $B_{total} = B_v + B_m = 0.125$Ns/m and $K_{total} = K_c = 18.33$N/m.

Referring to the numerical simulation experiments, when the force constraint is accommodated by either B_p or K_p independently, there is a greater demand on each parameter (see experiments B(10) and K(01)). Using both together, B(11) and K(11), the demand is clearly reduced. During *Recovery Phase* B_{total} is set to critical damping consequently its magnitude becomes ≈ 1.4Ns/m. A singularity occurs at approximately 0.22s. During the transition between *Impact Phase* and *Recovery Phase* the spring compression is maximum. Hence, its velocity is zero and Equation 18 becomes singular.

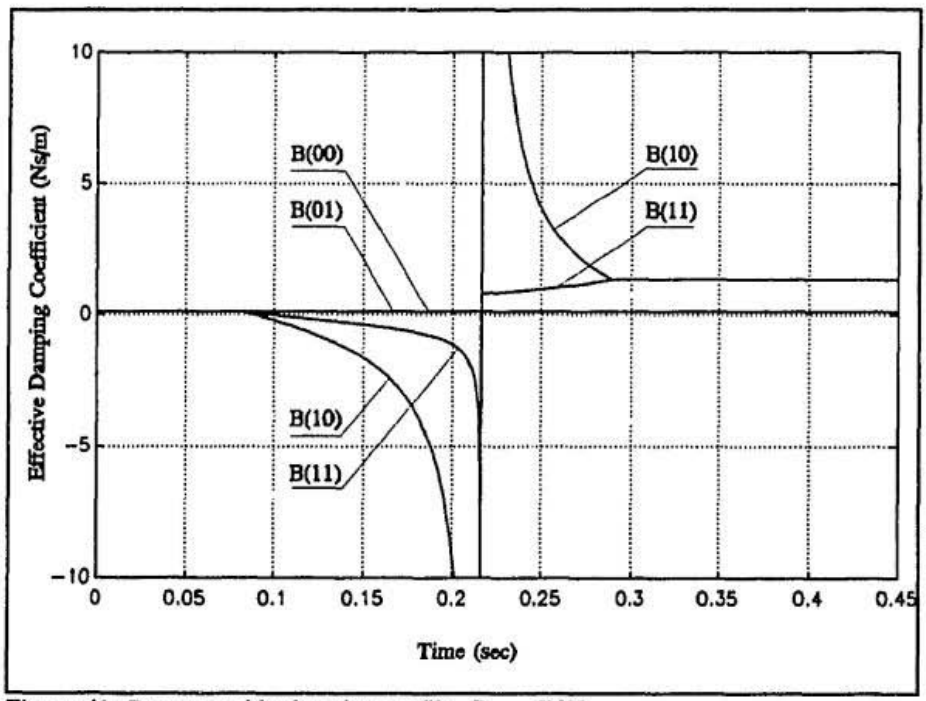

Figure 41: Programmable damping profile, B_{total} - [NS].

Referring to the robot experiments, when the force constraint is accommodated by either B_p or K_p independently, again the demand on each parameter changes between the *Impact Phase* and the *Recovery Phase* (see experiments B(10) and K(01)). Using both together, B(11) and K(11), the demand is clearly reduced. During *Recovery Phase* B_{total} is set to critical damping consequently its magnitude goes to ≈ 1.4Ns/m. A singularity occurs at approximately 0.22s. During the transition

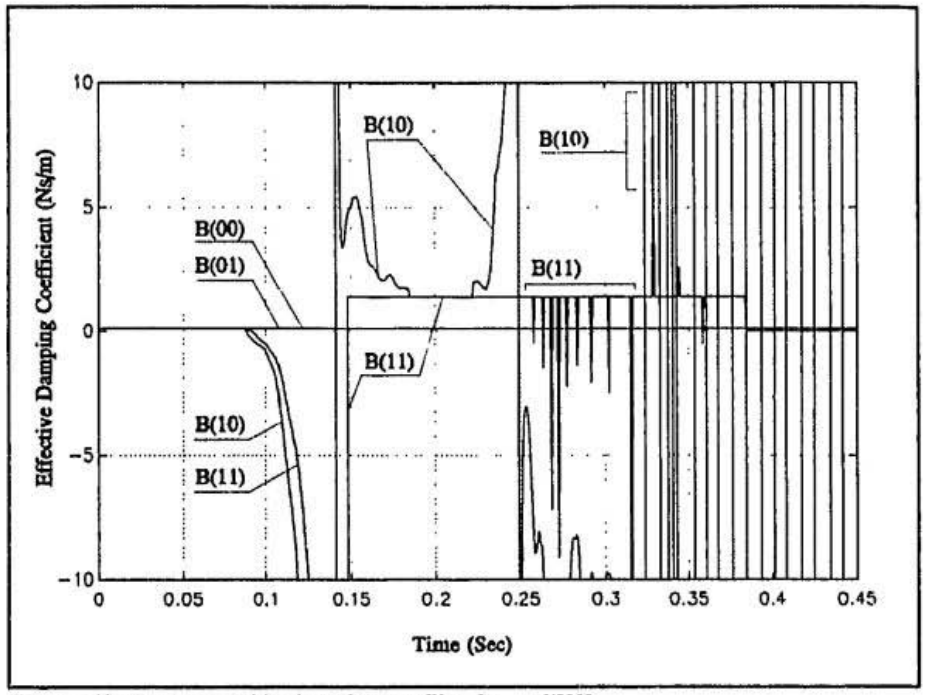

Figure 42: Programmable damping profile, B_{total} - [EX].

between *Impact Phase* and *Recovery Phase* the spring compression is maximum. Hence, its velocity is zero and equation 18 again becomes singular.

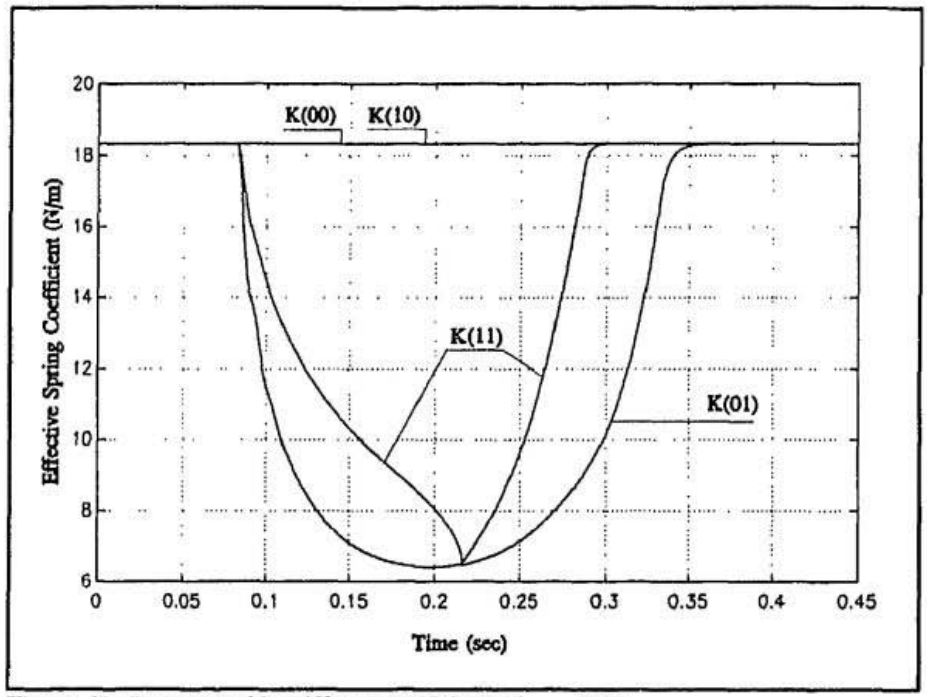

Figure 43: Programmable stiffness coefficient, K_{total} - [NS].

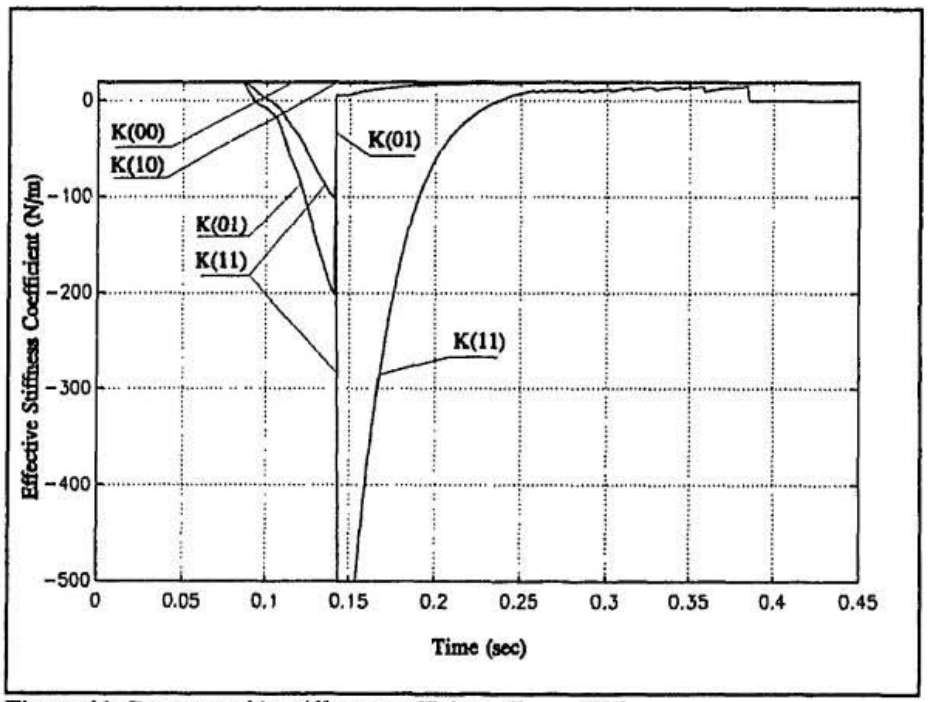

Figure 44: Programmable stiffness coefficient, K_{total} - [EX].

4.2.2 Experiment II

The experiments contained in this section were conducted using a ±60v@±5amp power supply. During the last experiment, E(11), the power supply's blood pressure dropped, fibrillation was induced and spontaneous self-cremation reduced its blood-current level below normal operating conditions. Therefore, E(11) is incomplete and clearly visible, $t \approx 0.16s$, in each of the figures to follow. As with the two previous experiments, the actuator is consistently dropped from 1.5cm which, under the influence of gravity, generates an impact velocity of $\approx 0.50m/s$. Also, during *Recovery Phase* B_{total} is set to critical damping. It should be noted that if damping is turned off, as in E(01), then even though B_{total} equals B_{crit} the damping effects are not actually implemented. The imposed force constraint on F_{crit_robot} = 0.35N.

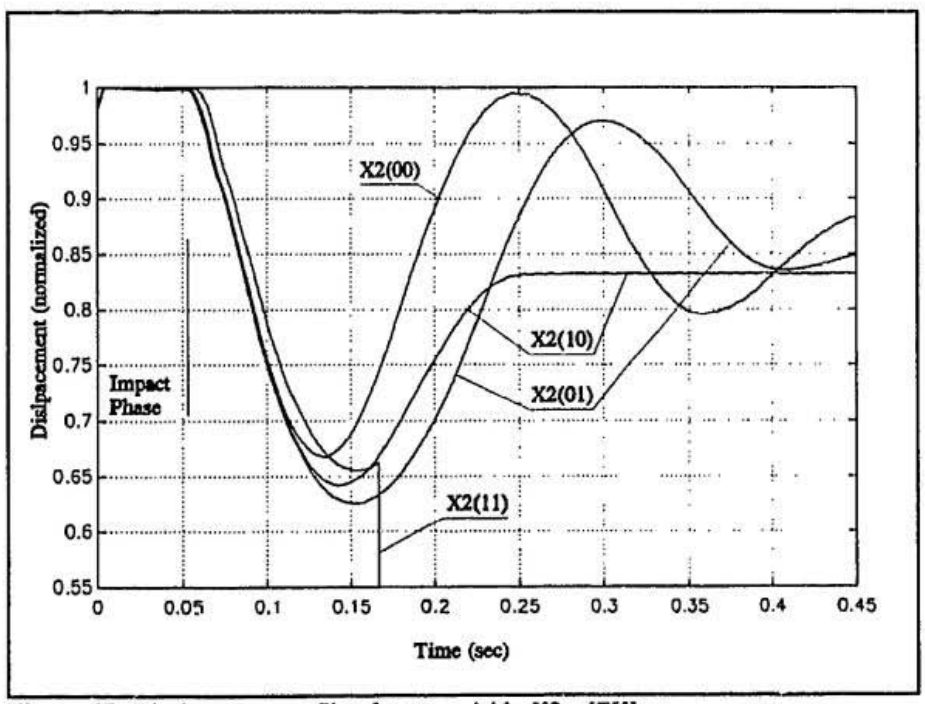

Figure 45: Displacement profile of state variable X2 - [EX].

This section will not contain as much detail as the previous section due to its repetitive nature. However, the important differences are highlighted. Experiment (00) demonstrates the contact effects with B_p and K_p turned off. Note that F_{robot} peaks at about 0.53N (see Figure 47), contact is oscillatory (see Figure 45) and Post-Contact Phase is never reached due the oscillations. Essentially, there is not enough energy being dissipated during the *Impact* and *Recovery Phases*. Experiment (10) demonstrates constrained contact motion with $F_{crit}=F_{crit_robot}=0.35$N, B_p at 100% and K_p turned off. As $F_{generated}$ violates $F_{crit\_robot}(t \approx 0.9s)$, B_p adjusts to accommodate the force constraint (see Figure 50). Notice the relatively linear velocity response of Vtop_1. The filtered F_{robot} signal, Figure 47, clearly indicates the actuator's attempt to keep $F_{robot} < F_{crit\_robot}$. Similarly, Experiment (01) demonstrates the same effects with K_p at 100% and B_p turned off. As F_{crit_robot} is violated K_p adjusts to maintain F_{robot} at or below 0.35N. Contact is maintained, however, in this case displacement oscillations

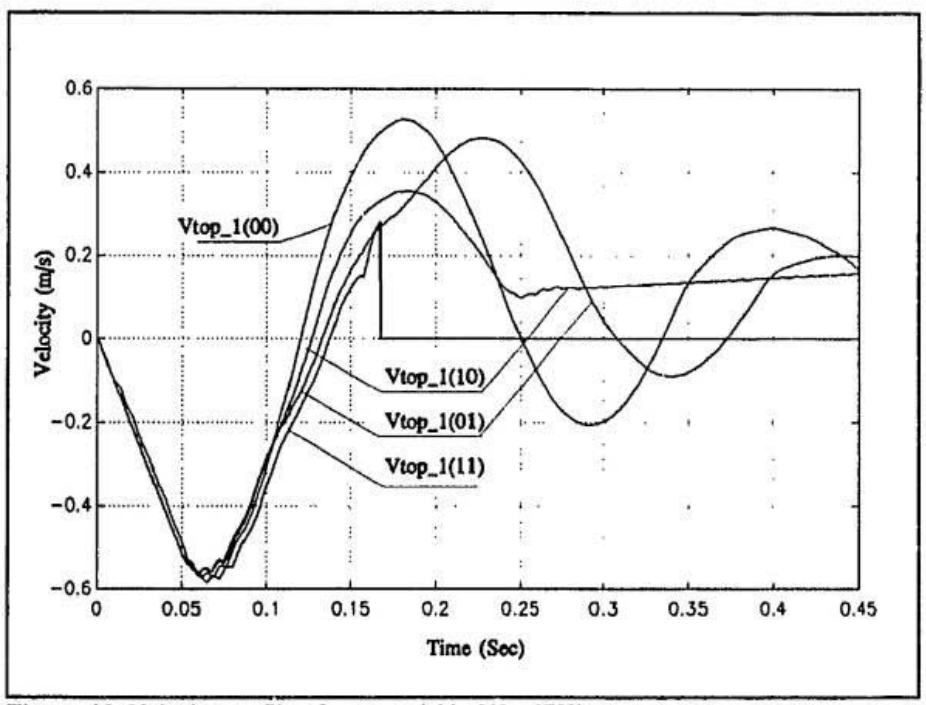

Figure 46: Velocity profile of state variable V2 - [EX].

prevent *Post-Contact Phase* from occurring(refer to Figure 45). The final Experiment, (11), is incomplete. During the first part of *Recovery Phase*, the power supply malfunctioned which prevented its completion. The free fall and *Impact Phase* portions of the experiment, however, were recorded. From this information it is clear that F_{robot} is never violated (see Figure 47) and the demands upon the programmable damping and stiffness is reduced in comparison with E(10) and E(01). These observations prevail throughout all three experiments. Consider the four plots of F_{robot} in Figure 47 and Figure 43. The three force constrained experiments exceed 0.35N. This is attributable to digital filter delays, non-collocated sensors, mutate time constant and other feedback control effects.

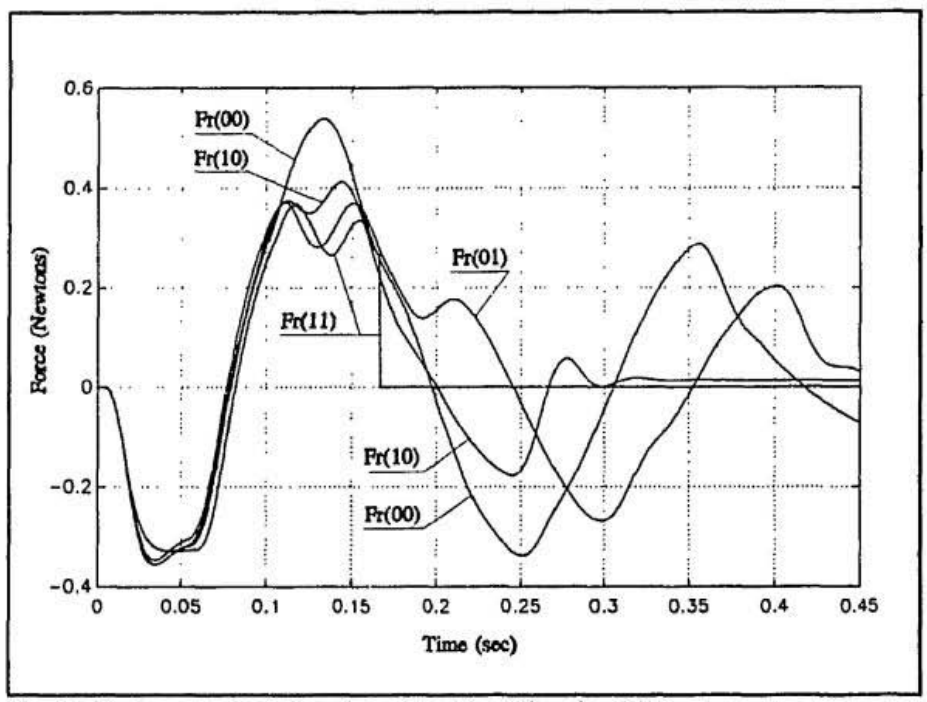

Figure 47: Force generated on the robot, F_{robot}(Filtered) - [EX].

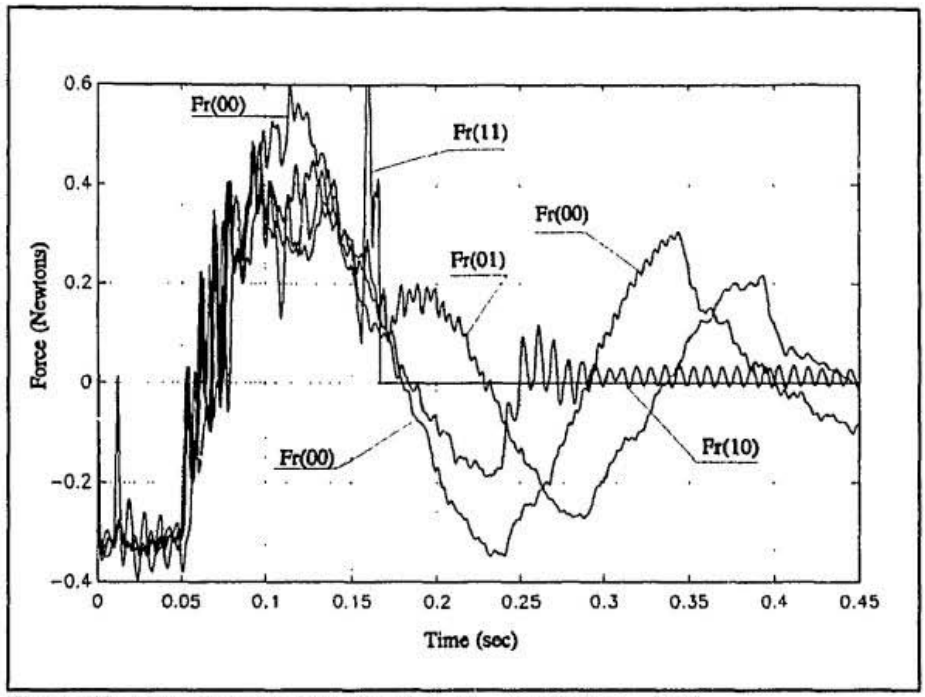

Figure 48: Force Generated on the robot, F_{robot}(Unfiltered) - [EX].

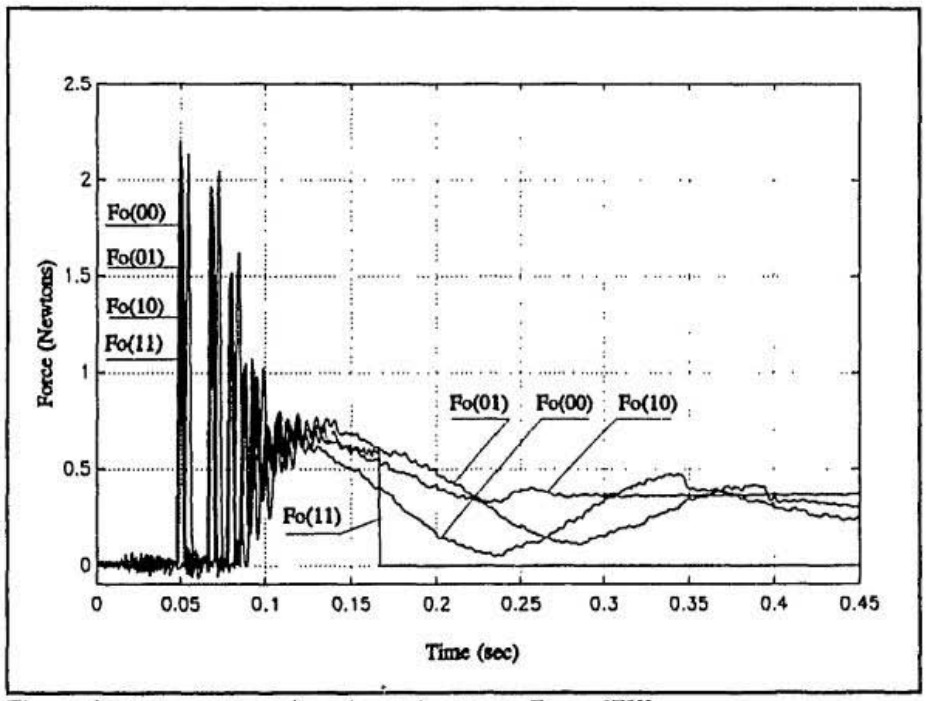

Figure 49: Force generated on the environment, F_{object} - [EX].

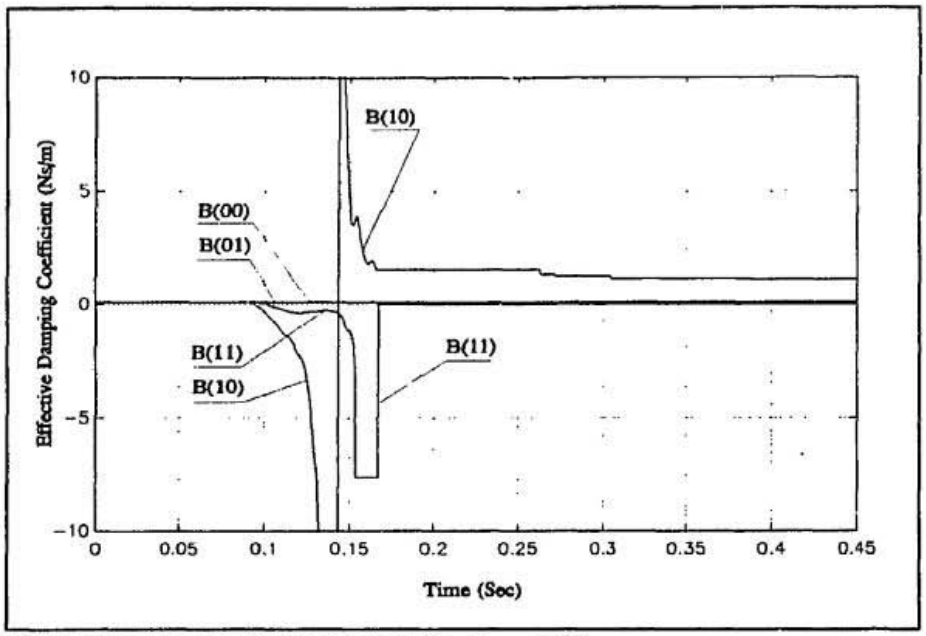

Figure 50: Programmable damping profile, B_{total} - [EX].

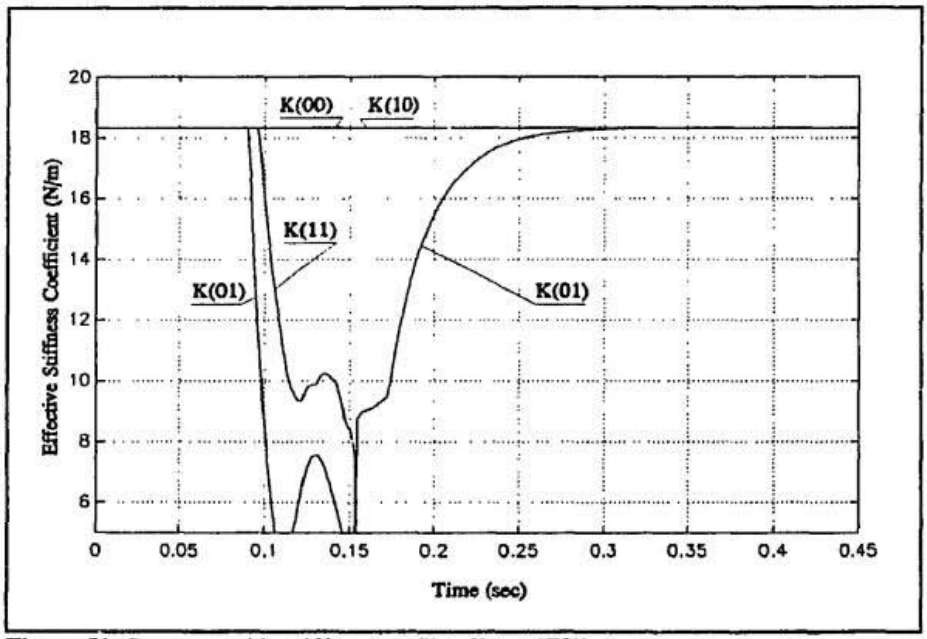

Figure 51: Programmable stiffness profile, K_{total} - [EX].

4.2.3 Experiment III: Advanced Damping Algorithm

During the *Recovery Phase* the damping coefficient is altered based upon a more advanced contact algorithm. This added piece of software attempts to further reduce the time associated with bringing the robot end-effector to steady state. Hence, an increase in the task execution bandwidth.

The C source code of the extra software added to the *Recovery Phase* is illustrated below. Based upon the predicted steady state displacement of *X2* the effective damping, B_{total}, is adjusted to reflect the urgency of bringing the robot system to steady state. There are three conditional statements("if"). The last conditional statement reflects the possibility that the improved algorithm may not be the best solution and instructs the robot to return to the original compliant control algorithm. This is a safety precaution which ensures F_{crit_robot} is never violated. Consider the first conditional statement. It states that if the force being generated on the robot is under control and the calculated damping(which is used to evaluate $F_{desired}$), based on the original control algorithm, is under control, consider the advanced algorithm. If the displacement is above or below X_{ss} the damping is programmed to allow a quick return to X_{ss} based upon the system's instantaneous velocity. If the actuator is near X_{ss} and the velocity is approximately 0.0m/s. then the second conditional statement indicates that there is no need to worry about state of the robot - Stability has been reached and *Post-Contact Phase* has been entered(or pending). In essence, the damping parameter is reduced to allow the compressed spring energy to bring the system toward X_{ss}.

```
/* ========================================================*/
        Tolerance = 0.001;
        if( (F_robot < F_crit_robot) && (F_desired < F_crit_robot) )
                {
                ΔXss = Xss - X2;
                if( (|V2| > Tolerance) && (ΔXss > Tolerance) )
                        {
                        Bp = Bp_current - ΔXss*[K_total]/|V2|;
```

```
                    B_total = Bp + Bv + Bm;
                    Fb = -B_total*(V2-V1);
                    F_desired = Fb + Fs;

                    if( F_desired > F_crit_robot )
                            {
                            IMPLEMENT ORIGINAL ALGORITHM!
                            }
                    }
            }
/* ==========================================================*/
```

To illustrate the effectiveness of the advanced algorithm profiles of $X2$, $V2$, F_{robot}, and B_p have been overlaid in the original numerical simulation plots contained in Section 4.2.1.. They have been reproduced here for convenience. The same experiment initial conditions remain. The nomenclature used to highlight the inserted plots is *(dd) which stands for double damping. Displacement profiles in Figure 52 clearly indicates X_{ss} is reached in a shorter period than in any of the original four experiments. From the velocity profile it is clear that the robot system overshoots the desired X_{ss} position but the overshoot is not significant. The force generated on the robot is kept below F_{crit_robot} and Figure 55 illustrates the degree to which the programmable damping is modified to implement the changes ($0.028s \leq t \leq 0.37s$).

In terms of the time benefits associated with this advanced compliant algorithm, about 0.012 seconds is saved - in comparison with experiments (10) and (11). The performance of the robot in terms of its ability to grasp an object has increased, Hence, its operating bandwidth has increased. For arguments sake, assume that a fixed assembly robot performs a particular task 2000 times in one day cycle(one task takes 43.2 seconds). On a per day basis, the total time saved is 24 seconds or 0.4 minutes. In one year this accumulates to $\approx$2.433 hours. This figure is relatively small with reference to one robot, however, if every robot in the world implements the advanced feature the cost savings is clearly enormous.

This algorithm is not implemented on the direct-drive robot arm simply because the subtle effects would not be observable.

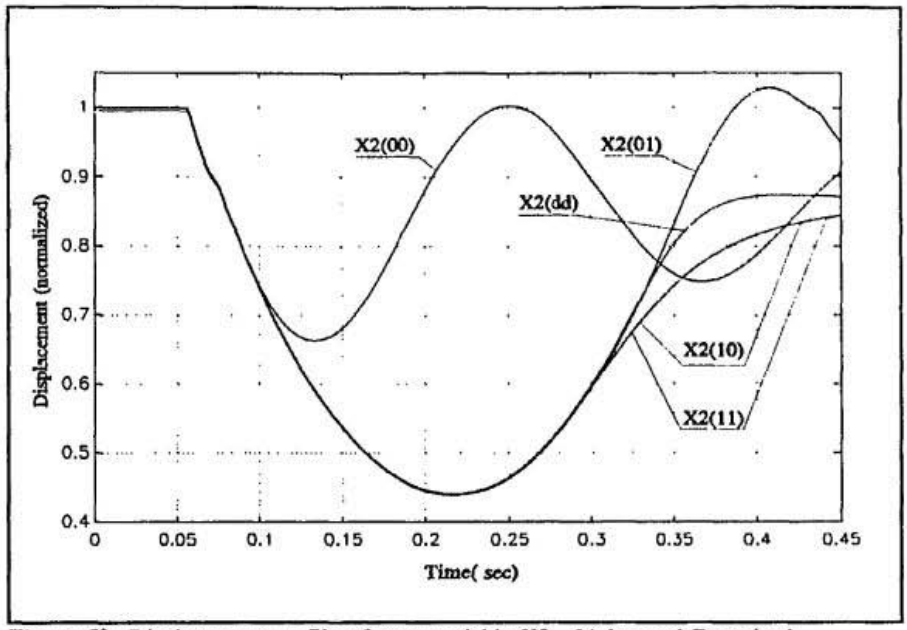

Figure 52: Displacement profile of state variable X2 - [Advanced Damping].

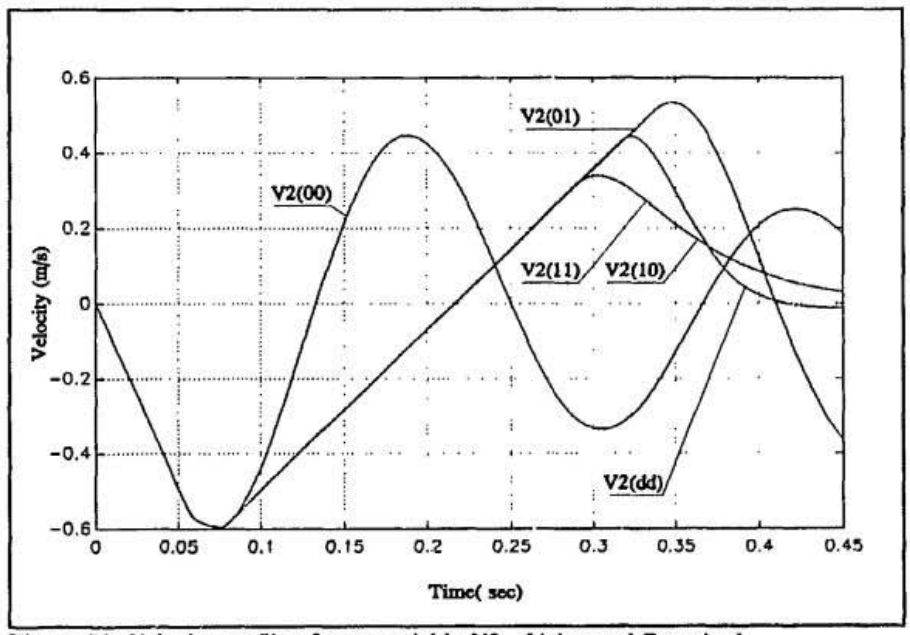

Figure 53: Velocity profile of state variable V2 - [Advanced Damping].

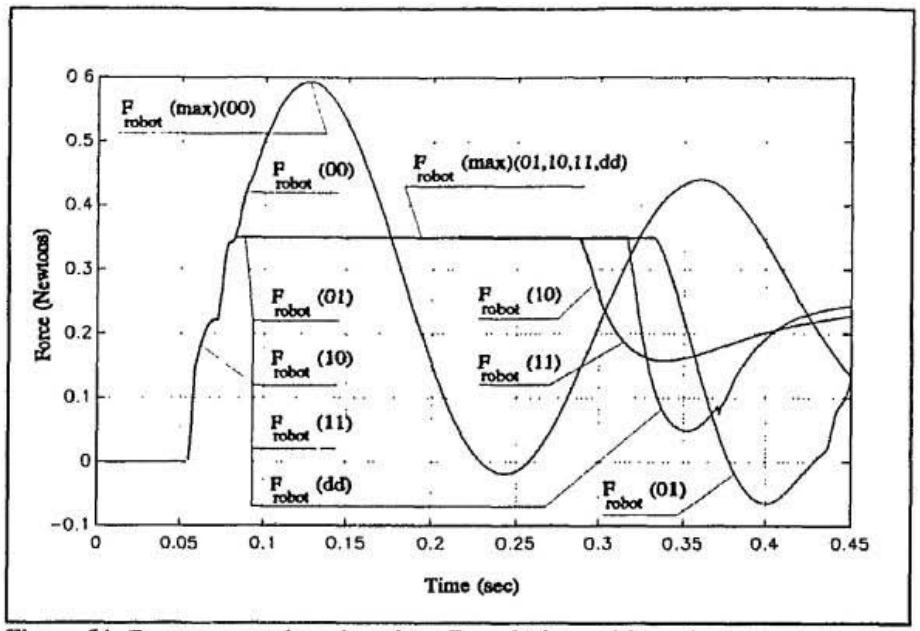

Figure 54: Force generated on the robot, F_{robot} -[Advanced Damping].

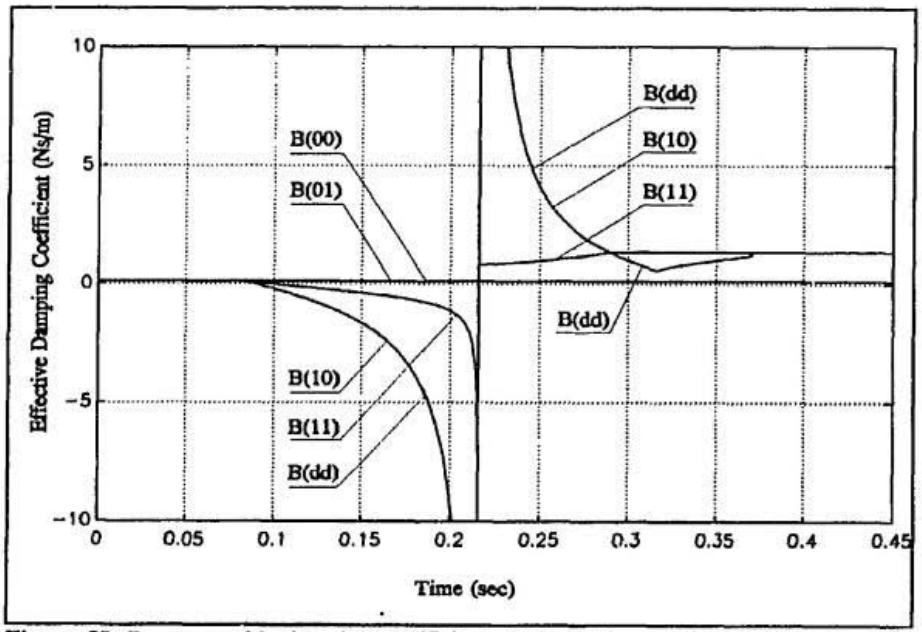

Figure 55: Programmable damping coefficient, B_{total} - [Advanced Damping].

Chapter 5

5.0 Conclusions and Observations

Discrepancies between the robot and the numerical simulation software model are mainly due to unmodeled damping characteristics of the direct-drive robot arm and the inadequate power supply. During the free fall experiments it is evident that as time progressed the unmodelled frictional effects become instrumental in diverging the simulation and robot experiment outputs. However, over the duration of the free fall experiments the numerical simulation and robot experiments clearly showed a high degree of correlation.

The process of integration inherently attenuates signal dynamics. Integration is a summation process which depends upon the instantaneous signal multiplied by the sample period. A typical sample period is much less than one, $\Delta t << 1$, which "squashes" small signal dynamics. The process of differentiation, on the other hand, inherently amplifies minute fluctuations. Differentiation requires the division of the difference between the current signal sample, S[n], and the previous signal sample, S[n-1], by the sample period. Due to the sample period being much less that one,

division "explodes" the difference. The greater the difference the more amplification experienced.

Several important factors exist which are essential prior to purchasing and installing any sensor. 1) Sensors must be chosen carefully to meet the dynamic range specifically for the intended requirements. Load Cell #1, LC_1, is a prime example. The peak compressional force experienced by LC_1 is clearly evident in Figure 19. The $\pm$5N range of the load cell far exceeds the intended application by (5N/$\approx$0.115N)*100% $\approx$4348%. A $\pm$0.75N or even a $\pm$1N load cell would have been sufficient. With the $\pm$5N load cell, the required circuit Gain equalled 2596. This amplified not only the robot's vibrational modes and power supply noise but also people walking in the corridor and the air conditioning fan vibrations. This noise added to inband noise which could not be effectively dealt with. 2) Sensors typically have more than one dynamical process superimposed on its output. A careful examination of what the sensor is to measure and possible interference situations, based upon its mount position, is necessary. Due to the wide variety of available sensors technologies, typically one can be chosen which is impervious to external interference. In band-noise is difficult to work around. 3) Calibration is another extremely important consideration. Electronics and the sensor itself are sensitive to a variety of parameters. Some parameters are controllable quantities, for example, temperature, and some are uncontrollable quantities, for example, age. These parameters affect sensor calibration. A good sensor design should provide means of real-time self calibration. This will ultimately ensure accuracy and long term reliability.

Several motors were destroyed during the Direct-Drive Robot Arm experiments. These motors are not designed to handle $\pm$5amps. Even though the current is pulsed and the experiment duration is less than 0.5s, over time the coated wires of the armature break down and short.

The *Solenoid Release Mechanism* scrapes along the under carriage of the *Robot Tip Assembly* at the beginning of each experiment. This energizes the robot's vibrational modes and also vibrates the support rod on which the Solenoid is mounted. Stabilizer #1 and Stabilizer #2 help dampen this effect.

Preventing the Direct-Drive robot spring from entering into a tension imparts dynamics which compromise system performance. Sometimes during the *Recovery Phase* the rubber tip bounces off the *Impact Surface*. During this transition the *Mechanical Stop* impacts off the *Spring Slider Guide* creating an energy spike. This excites the vibrational modes of the robot which ultimately effect the feedback control loop operation. The impact effects are clearly illustrated in Figure 19 at $t \approx 0.24s$.

A clear foundation for the positive benefits of introducing compliance during strategic time frames associated with environment interaction is given. Damping ultimately dissipates energy and aids in minimizing the time taken to enter *Post-Contact Phase*. Thus, t_{settle} is minimized and the system task execution bandwidth is increased. Altering the contact process with the stiffness parameter, under a force constraint, ultimately stores the energy associated with impact and allows this potential energy to be used if desired. In conclusion, there is a tradeoff between impact energy storage versus impact energy dissipation. This question is application specific and from a more advanced perspective decided in real-time based on the current task. In terms of mobile robots, in the future they will employ demanding running gait strategies. They will benefit from maximum energy retrieval as well as controlled energy dissipation. Such abilities offer extensive strategic opportunities in terms of control algorithms during the transition between compliant and stiff terrains and in terms of stopping. This area of the robot industry is still in its infancy compared to their fixed assembly robot counterparts. In terms of the fixed assembly robots, energy removal dominates.

An idea which may be beneficial in terms of deciding the required percentage

of damping and stiffness may fall under the following proposed regime. The natural damped bandwidth on the environment should be three to four times as small as the natural damped bandwidth of the robot interaction. This would allow the robot to respond, if needed, without attenuation.

The developed numerical simulation model for the single degree of freedom Direct-Drive robot arm is an accurate representation of a real-world system. A high degree of confidence can be placed in the simulation results. The program is ultimately a research tool in which every parameter may be varied. Any control algorithm concept can be implemented during any phase of contact independently or in some combination, with confidence levels equal to the programmer's abilities.

The Direct-Drive robot arm is a detailed, finely machined structure. All components are adjustable to allow for calibration and component alignment. It is light weight and mobile. Modifications are easily implemented, for example, adding new sensors, extending the robot length and the installation of a more powerful motor. As with the numerical simulation program, the direct-drive single degree of freedom robot is ultimately a research tool in which every parameter may be varied.

Ideal Damping and Ideal Stiffness laws were given for implementing a programmable compliant environment interactive control strategy. Based on these equations the decision of energy dissipation versus energy conservation is addressable. Each equation can independently facilitate contact while limiting the generated force on the robot and/or the environment.

The contact process has been broken into 5 well defined phases: *Pre-Contact Phase*, *Pre-Contact Critical Phase*, *Impact Phase*, *Recovery Phase* and *Post-Contact Phase*. Recognising these phases is a critical step in allowing robot interactions with the environment.

The advanced programmable damping algorithm presented in Chapter 4 reconfirms the notion that the originally proposed ideal equations are not the absolute optimal solution. Further research must be based on clearly defining what is best for a particular task. From a practical perspective the software model should be developed and included in a three degree of freedom gripper and actual assembly tasks executed. This will highlight and provide more realizable limitations and insight to the limitations of the suggested programmable compliant algorithm.

Digital filtering techniques provide an easy method of implementing filters. One major drawback, however, is the delay associated with filtering. This delay must be carefully considered when used in a feedback control algorithm. Unstable behaviour and loss of feedback parameter tracking are two dominant control problems which are sensitive to feedback delays.

The optimal tradeoff between the percentage of damping and stiffness has not been addressed. This is an application specific question and requires clearly defined task goals. Only then can the "best" solution be focused upon and evaluated in terms of performance and if indeed there is a "best" solution.

The compliant concept described has many practical uses beyond the mobile and fixed robot industry. The Introduction and Chapter 2 illustrates a variety of applications. To extend the list beyond the robot industry the following have been cited. Adaptive shock absorbers: potential applications include aircraft, cars and space vehicle interactions (docking). Vibration snubbers: potential applications include industrial machines, jack hammers and structure which are subject to earthquakes and other unpredictable natural events. In all cases the compliant device would in real-time limit the force being transmitted, from the disturbance source, to the destination without damaging the destination structure. The destination structure, for example, being a vehicle(impact forces) or a building.

Chapter 6

Recommendations

The following recommendations are put forth based upon observations made throughout the development and experiments carried out on the direct-drive robot arm. Described are not only enhancements which would make the existing hardware and software of the direct-drive robot arm more robust, reliable and efficient but enhancements which would alter its physical appearance.

1) The Direct-Drive Robot Arm should be modified to allow control of the force generated on the object. These modifications could include a second motor mounted in the same configuration as the motor currently used. The second motor, however, would be coupled to the reflector disk assembly via a second aluminum shaft. This position would allow control of the lower portion of the physical spring. In essence, both ends of the spring could be independently controlled which would mimic changing the spring constant K_c. Another solution centres on the development of an electromagnet damper and spring. The time constants in this design would provide a higher bandwidth.

Electro-Rheological fluids would provide an means of implementing positive damping.

2) The power rating of the armature controlled permanent magnet DC motor should be increased. Cogging should be kept at a minimum.

3) The electrical schematics for the five sensors, motor driver and solenoid driver should be implemented on printed circuit boards. This would not only eliminate wire connection noise and create a better ground plane but would make assembly and disassembly easier.

4) To allow the spring to enter the Tension state, the end of the spring closest to the *Actuator Tip Assembly* should be connected. This would allow removal of the *Mechanical Stop* and eliminate the impulse spike from effecting the control algorithm.

5) The Real-Time interrupt driven control software should be streamlined. This would allow the sampling rate to increase resulting in performance benefits. Separate processors could also be used, one for sensor measurment and filtering and one for feedback control.

6) The robot arm base should be mounted on an isolation table in an effort to reduce external vibration excitations.

7) The horizontal angle offset of the accelerometer and LC_1 should be accounted for in both the numerical simulation and the control algorithm.

8) Throughout the experimentation, environment models were limited to stiff uncompliant surfaces. It is suggested that further studies be conducted on compliant environment models and also time varying models.

9) Static and Kinetic friction tests should be designed to evaluate the frictional effects associated with 1) the rubber tip's lateral movements across the *Impact Surface* and 2) the *Spring Slider* movements through the *Spring Slider Guide*.

Chapter 7.0

References

Akella, P., Siegwart, R. and Cutkosky M., 1991, "**Manipulation with soft fingers: Contact force control,**" In *Procs. of the 1991 IEEE ICRA*, pp. 652-657.

Akella, P. and Cutkoskey, M., 1989, "**Manipulating with soft fingers: Modeling contacts and dynamics,**" In *Procs. of the 1989 IEEE ICRA*, pp. 764-769.

An, C. H. and Hollerbach, J. M., 1987, "**Dynamic Stability issues in Force Control of Manipulators,**" *Proceedings of International Conference on Robotics and Automation*, pp. 890-896. IEEE Press.

Asada, H. and d Youcef-Toumi, K., 1987, "*Direct-Drive Robots*," The MIT Press, Cambridge, Massachusetts, USA.

Burton, R., 1968, "*Vibration and Impact*", Dover Publications, New York.

Cetinkunt, S. and Wu, S., 1992, "**Discrete-Time Tip Position Control of a Flexible One Link Arm,**" *Journal of Dynamic Systems, Measurement, and Control*, Vol. 114, pp. 428-435.

Colgate, E. and N. Hogan., 1989, "**An Analysis of Contact Instability in Terms of Passive Physical Equivalents,**" *Proceedings of International Conference on Robotics and Automation*. IEEE Press.

Cutkosky, M. R. and Kao, I., 1989, "**Computing and Controlling the Compliance of a Robotic Hand,**" *IEEE Transactions on Robotics and Automation*, vol. RA-5, no, 2. pp. 151-165.

Daniel, R.W., Irving, M.A., Fraser, A.R. and Lambert, M., 1985, "**The Control of Compliant Manipulator Arms**", pp. 119-125.

Eppinger, S.D. and Seering, W.P., 1986, "**On dynamic models of robot force control,**" In *Proceedings of International Conference on Robotics*, IEEE, pp. 29-34.

Eppinger, S.D. and Seering, W.P., 1992, "**Three Dynamic Problems in Robot Force Control,**" *IEEE Transactions on Robotics and Automation*, Vol. 8, No. 6, pp. 751-758.

Haug, E.J., Wu, S.C. and Yang, S.M., 1986, "**Dynamics of Mechanical Systems with Coulomb Friction, Stiction, Impact and Constraint Addition - Deletion I,**" *Journal of Mechanism and Machine Theory*, Vol. 21, No. 5, pp. 401-406.

Instrumar Limited, "**Evaluation of Potential Sensing Technologies for the Mobile Servicing System for the Space Station,**" P.O. Box 13246, Station A, St John's, Newfoundland, Canada A1B 4A5, March 20, 1992.

Johnson, R.C., 1958, "Impact Forces in Mechanisms," Machine Design, June 12.

Kazerooni, H., Waibel, B. J. and Kim S., 1990, "**On the Stability of Robot Compliant Motion Control: Theory and Experiments,**" ASME Journal of Dynamic Systems, Measurement and Control, Vol. 112, pp. 417-425.

Kazerooni, H., 1987, "**Robust, Non-Linear Impedance Control for Robot Manipulators,**" *Proceedings of IEEE International Conference on Robotics and Automation*, pp. 741-750.

Laurin-Kovitz, K.F., Colgate, J.E. and Carnes, S.D.R., 1991, "**Design of Components for Programmable Passive Impedance,**" *Proceedings of International Conference on Robotics and Automation*, pp. 1476-1481.

Liu, G.J. and Goldenburg, A.A., 1991, "**Robust Hybrid Impedance Control of Robotic Manipulators,**" *Proceedings of the International Conference on Robotics and Automation*, IEEE, pp. 287-292.

Luk, B.L., Collie, A.A. and Billingsley, J., 1991, "**Robug II: An Intelligent Wall Climbing Robot,**" Procs. ICRA, pp. 2343-2347.

Martin, K.F. and Lockman, H., 1987, "**Force Sensing in Magnitude, Direction, and Position,**" *Transactions of the ASME*, Vol. 109, pp. 286-290.

Mason, M.T., 1981, "**Compliance and Force Control for Computer Controlled Manipulators,**" *IEEE Transactions on Systems, Man, and Cybernetics*, Vol SMC-11, No. 6, pp. 418-432.

Mills, J.K., 1989a, "**Stability of Robotic Manipulators During Compliant Motion with Application to Transition to and from Compliant Motion,**" submitted to

Automatica.

Mills, James K., 1990, "**Manipulator Transition to and from Contact Tasks: A Discontinous Control Approach,**" In *Procs. of the 1990 IEEE ICRA*, pp. 440-446.

Mills, J.K. and Nguyen, C.V., 1992, "**Robotic Manipulator Collisions: Modeling and Simulation,**" *Transactions of the ASME*, Vol. 119, pp. 650-659.

Parker, J.K. and Paul, F.W., 1987, "**Controlling Impact Forces In Pneumatic Robot Hand Designs,**" *Transactions of the ASME*, Vol. 109, pp. 328-334.

Paul, R. and Shimano, B., 1976, "**Compliance and Control,**" Proceedings of the *Joint Automatic Controls Conference*, AUTM2-2, pp. 694-699.

Raibert, M.H., "**Four-Legged Running with One-Legged Algorithms,**" Second International Symposium on Robotics Research, H. Hanafusa, H. Inoue (eds). Cambridge: MIT Press, pp. 311-315.

Warnecke, H. and Lindner, H., 1985, "**Trends in Robotics Research in the European Community,**" *Proceedings of the International Conference on Robotics and Automation*, IEEE, September 9-10, pp. 7-13.

Whitney, D.E., 1976, "**Force Feedback Control of Manipulator Fine Motions,**" *Joint Automatic Control Conference*, pp. 687-693.

Whitney, D.E., 1985, "**Historical Perspective and State of the Art in Robot Force Control,**" *Proceedings of IEEE International Conference on Robotics and Automation*, pp. 262-286.

Whitney, D.E., 1987, "**Historical Perspectives and State of the Art in Robot Force Control,**" *International Journal of Robotics Research*, Vol. 6, no. 1, pp. 3-14.

Yang, B. and Mote, C.D.Jr., 1992, "**On Time Delay in Noncolocated Control of Flexible Mechanical Systems,**" *Journal of Dynamic Systems, Measurement, and Control*, Vol. 114, pp. 409-415.

Zheng, Y.F. and Fan, Y., 1991, "**Robot Force Sensor Interacting with Environments,**" *IEEE Transactions on Robotics and Automation*, Vol. 7, NO. 1, pp. 156-164.

Zheng, Y.F. and Hemami, H., 1985, " **Mathematical Modelling of a Robot Collision with its Environment,**" *Journal of Robotic Systems*, Vol. 2, No. 3, pp. 289-307.

Appendix A

Direct-Drive Robot Arm Details

Figures

Tables

A.0 Critical Mass Components

Prior to assembly, critical component mass's were evaluated. The values for M_{top}, M_{mid} and M_{tip} are evaluated based on the collected data and used in the Numerical Simulation software. Table AI contains a description of the each component and its corresponding mass. Figure A1 indicates the location of each component.

Table AI: Robot arm component description and masses.

Num	Description	Mass
1	LC_1_Y02_Sensor_Mass	3.13
2	AC_Sensor_Mass	0.75
3	PS_1_Sensor_Mass	2.29
4	Stabilizer_1_Mass	0.33
5	Couple_Clamp_2_Mass	0.73
6	Actuator_Tip_Jig_Mass	2.94
7	Slider_Guide_Mass	1.0
8	Robot_Aluminum_Arm_Mass	5.88*0.5
9	Physical_Spring_Mass	0.69/2
10	Stabilizer_2_Mass	2.5*0.45677
11	Wire_Mass	1.50
12	Robot_LC_Couple_Clamps_Mass	0.25
13	Robot_LC_Carriage_Mass	0.75
14	Plastercine_Mass	6.75
	M_{top}	24.8469
15	Reflector_Disk_Assembly_Mass	2.92
16	Spring_Slider_Guide_Mass	1.61
17	Physical_Spring_Mass	0.69/2
18	Mechanical_Stop_Mass	0.25
	M_{mid}	5.125
19	Rubber_Tip_Mass	0.016239347
	M_{tip}	0.016239347
	$M_{total} = M_{top} + M_{mid} + M_{tip}$	29.988

Notes:

1) All masses are given in grams.

2) The Physical_Spring_Mass is divided by two since it physically couples both M_{top} and M_{mid}.

3) Fifty percent of the Robot_Aluminum_Arm_Mass is used in computing M_{top} because only half of its mass is supported by the robot assembly.

4) The Stabilizer_2_Mass is scaled by 0.45677 because it is located 17.4815 cm from the robot tip. Based on the length of the robot arm, 31.59125 cm, the effective mass due to the stabilizer on the robot tip is multiplied by:

$$\frac{31.59125-17.4815}{31.59125}=0.45677 \qquad \text{(A1)}$$

5) The total mass associated with the sensor wires bussed through the main robot aluminum tube and the wire joining the LC_1, PS_1 and accelerometer sensors at the outer tip of the robot was estimated.

6) The rubber tip mass is calculated in Appendix B.

In comparison, the output of the impact load cell, LC_2, was recorded with the robot resting on the *Impact Surface*. This value should correspond with M_{total}. The load cell output voltage was measured to be 0.757volts, Therefore the force equals:

$$F_{object}=\frac{LC2_{output}}{LC2_{Gain}\times LC2_{Sensitivity}\times EX_{ratio}}=0.30694N \qquad \text{(A2)}$$

where $LC2_{output}$ = 0.757volts
$LC2_{Gain}$ = 241
$LC2_{Sensitivity}$ = 0.01535mV/N
EX_{ratio} = 10/15

which translates into, $M_T = F_{object}/9.81$ = 0.031289Kg = 31.289grams. In comparison, the results differ by 4.16%. The only assumption made during the mass calculation is the effective mass of the wire(see note 5). Evaluating this quantity is extremely difficult.

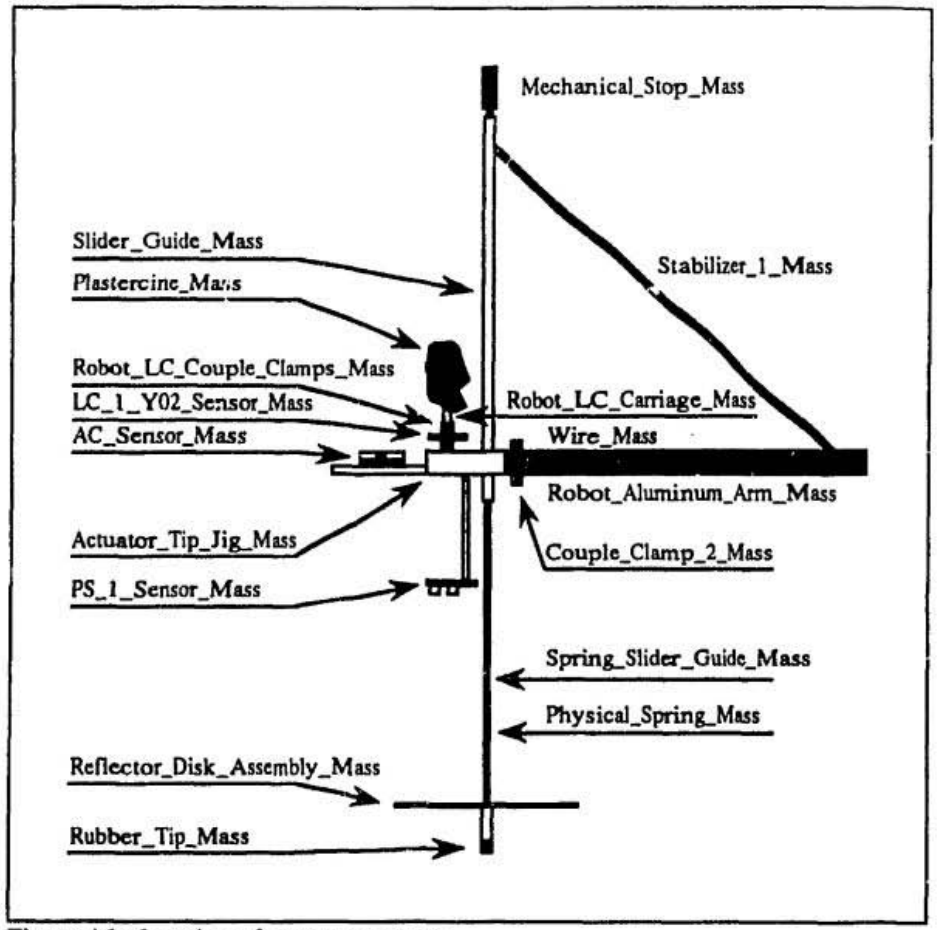

Figure A1: Location of mass components.

As a reference measurement, a 50g mass was placed on the *Impact Surface* and evaluated using the same procedure. The results were within 2.7%(51.33g). Taking this percentage off the measured mass, M_T, results in a discrepancy of less than 2%. This error could be a result of component drift resulting in the $LC2_{gain}$ being slightly off.

A.1 Component Dimensions

Figure A2 shows the dimensions used in the development of the direct-drive arm. The measured lengths do not constitute a complete list but contains the necessary

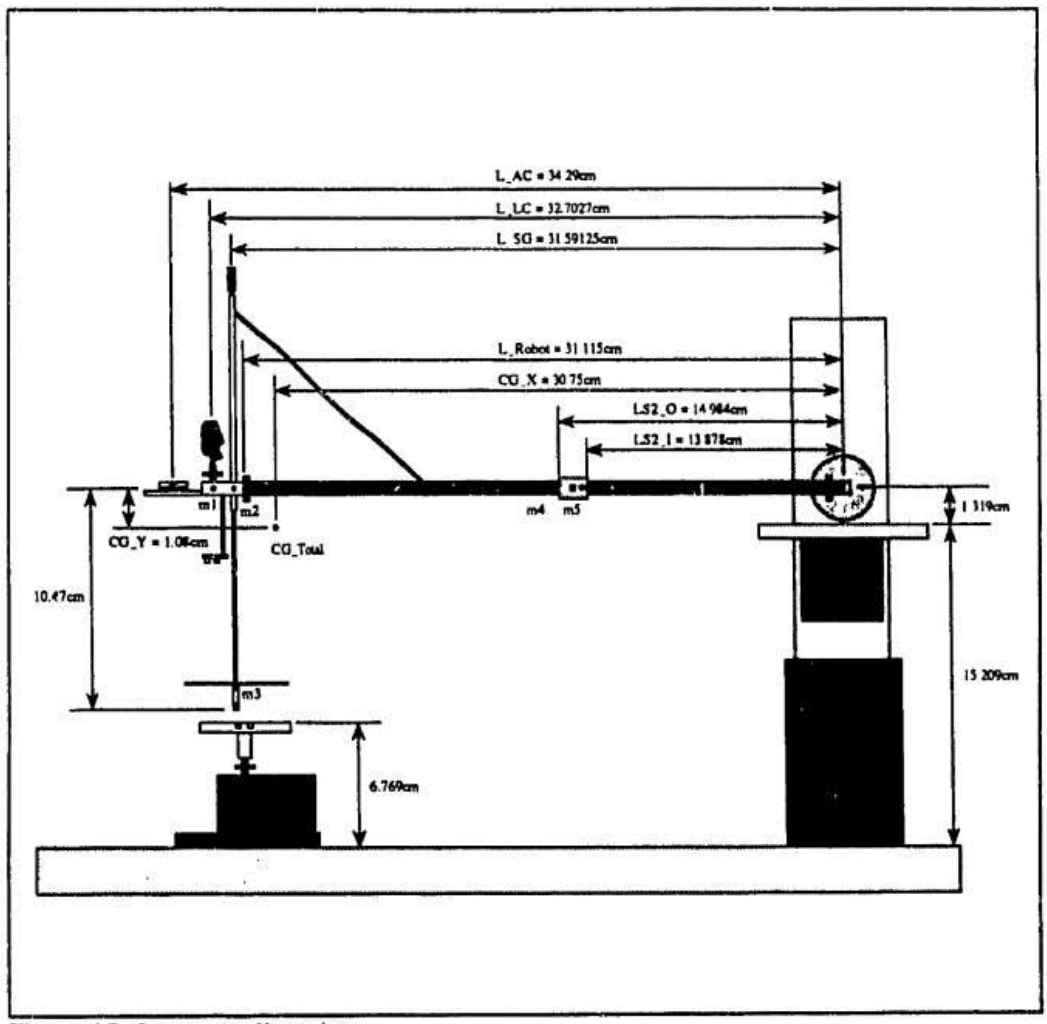

Figure A2: Important dimensions.

information required by the project. Also contained in the figure are the locations of the five strategic mass groups which are used in the centre of mass derivation in Section A.2.

A.2 Centre of Gravity

Evaluating the robot arm's centre of gravity is based upon identifying concentrated mass areas and grouping them together. There are five strategic regions in which the robot can be divided. Figure A2 identifies these locations. Adding the masses and locating their individual mass centres allowed the composite centre of mass to be evaluated. Matlab program MMI.m in Section A.2.1 contains the derivation for locating the center of mass during non-contact situations. Table AII summarizes the programs output.

Table AII: Center of mass program output - MMI.m.

item	Parameter	MMI.m output
1	m1 (grams)	15.64
2	m2 (grams)	6.33
3	m3 (grams)	2.9362
4	m4 (grams)	6.88
5	m5 (grams)	2.5
6	Mtotal (grams)	34.2862
7	Io (gramms*m^2)	3.3155
8	CG_X (meters)	0.3075
9	CG_Y (meters)	-0.0108
10	CG_Total (meters)	0.3077

Figure A2 indicates the relative position of the robot arm's effective mass centre, CG_Total. During the contact process, m3 moves toward m1 and m2. This changes the free fall centre of mass location derived in MMI.m. Overall, the effect of this mass migration only alters CG_Y and since CG_X is 29.4 times greater than CG_Y, the mass migration effects can be ignored.

A.2.1 Mass Moment of Inertia Program

```
% MMI.m =>      Mass Moment of Inertia:  created to determine the tagential
%              acceleration of the robotic tip.  This should correspond
%              to the accelerometer output.
%              VERSION 2.0 April 7, 1994.

L_AC = 0.3429;  % ===== Distance from the motor shaft to the accelerometer
L_LC = 0.327025;        % ===== Distance from the motor shaft to the robot LC
L_SG  = 0.3159125;      % ===== Distance from the motor shaft to the slider guide
L_Robot = 0.31115;      % ===== Distance from the motor shaft to the couple #1
LS2_O = 0.14984;        % ===== Distance from the motor shaft to outter Stabilizer #2
LS2_I = 0.13878;        % ===== Distance from the motor shaft to inner outter Stabilizer #2

% ===== Mass components lumped into five major sub-sections =====
A = 3.13;       %LC_Y02_Sensor_Mass
B = 0.75;       %AC_Sensor_Mass
C = 2.29;       %PS_Sensor_Spring_Mass
D = 0.75;       %Robot_LC_Carriage_Mass
E = 2.94/2;     %Actuator_Tip_Jig_Mass
F = 6.75;       %Plastercine_Mass
G = 0.50/2;     %Wire_Mass
H = 0.25;       %Robot_LC_Couple_Clamps_Mass
        m1 = A+B+C+D+E+F+G+H;
I = 1.00;       %Slider_Guide_Mass
J = 0.33;       %Stabilizer_1_Mass
K = 1.61;       %Spring_Slider_Guide_Mass
L = 0.69;       %Physical_Spring_Mass
M = 0.25;       %Mechanical_Stop_Mass
N = 2.94/2;     %Actuator_Tip_Jig_Mass
O = 0.73;       %Couple_Clamp_2_Mass
P = 0.50/2;     %Wire_Mass
        m2 = I+J+K+L+M+N+O+P;
Q = 2.92;       %Reflector_Disk_Assembly_Mass
R = 0.016239347;%Rubber_Tip_Mass
        m3 = Q+R;
S = 5.88;       %Robot_Aluminum_Arm_Mass
T = 1.00;       %Wire_Mass % ===== for the wire mass through main Tube =====
        m4 = S+T;
U = 2.5;        %Stabalizer_2_Mass
        m5 = U;
mt = m1 + m2 + m3 + m4 + m5;

% ===== Composite Center of Gravity Evaluation =====
     x1 = L_LC, y1 = 0.0, x2 = L_SG, y2 = -0.01, x3 = L_SG, y3 = -0.1047, x4 = L_Robot;
     y4 = 0.0, x5 = (LS2_O + LS2_I)/2, y5 = 0.0;

% ===== X component of Center of Gravity =====
     CG_X = (m1*x1 + m2*x2 + m3*x3 + m4*x4 + m5*x5)/mt;
% ===== Y component of Center of Gravity =====
     CG_Y = (m1*y1 + m2*y2 + m3*y3 + m4*y4 + m5*y5)/mt;
% ===== Effective Center of Gravity =====
     CG_total = sqrt((CG_X*CG_X + CG_Y*CG_Y));
% ===== Mass Moment of Inertia of the composit system referenced to motor axis =====
     Io = x1^2*m1 + x2^2*m2 + x3^2*m3 + x4^2*m4 + x5^2*m5;
% ===== Gravitational scaler =====
     C = (L_AC*mt*CG_total)/Io
```

A.3 Robot Mass Moment of Inertia

Based on the lumped effective mass of the robot's individual components and the effective centre of gravity, both derived from MMI.m an approximation of the robot's mass moment of inertia can be evaluated:

$$I_{robot}(1)=CG_{total}^2 \times m_{total}=0.3077^2 \times 0.034286=0.00324619 Kgm^2 \quad \text{(A3)}$$

and as a comparison consider the output of LC_2 with the robot resting on the impact surface:

$$I_{robot}(2)=L_{SG}^2 \times M_T=(0.3159125m)^2 \times 0.031289Kg=0.00312266 Kgm^2 \quad \text{(A4)}$$

which gives confidence within:

$$\frac{0.00324619-0.00312266}{0.00324619} \approx 3.81\% \quad \text{(A5)}$$

A.4 Accelerometer Output

During free fall, the robot arm is constrained by the *Actuator Mount Assembly*. Hence, the motion can be described as rotation about a fixed axis and the angular displacement of the *Robot Tip Assembly* subscribes an arc. The *Robot Tip Assembly* acceleration can be divided into normal, a_n, and tangential components, a_t. Since the accelerometer measures a_t we can evaluate the expected tangential acceleration, a_{tex}, based on the robot assembly and compare it with the output of the accelerometer.

Summing the moments about the motor shaft and solving for the angular acceleration:

$$\Sigma M_o = \alpha I_o = m_{total} \times g \times CG_{Total} - B_m \tag{A6}$$

where
I_o = Composite Mass Moment of Inertia
CG_{total} = Composite Centre of Gravity
m_{total} = Composite Mass
g = Earth gravity
B_m = Motor Friction Effects

therefore,

$$\alpha = \frac{m_{total} \times g \times CG_{total} - B_m}{I_o} \tag{A7}$$

Since the output from the accelerometer measures the tangential component of the *Robot Tip Assembly*'s acceleration, a_t, C can be evaluated with the equation $a_t = L\_AC * \alpha$:

$$a_t = L\_AC * \alpha = L\_AC * \left[\frac{m_t g CG_{total} - B_m}{I_o} \right] = gC - \frac{L\_AC * B_m}{I_o} \tag{A8}$$

where,

$$C = \frac{m_t \times L\_AC \times CG_{total}}{I_o} \tag{A9}$$

B_m is set to zero because the motor has been removed from the robot assembly. L_AC is the distance between the motor shaft and the location of the mounted accelerometer. The constant C is measured in g force and indicates A_{tex}. Again, Figure A2 illustrated the five strategic positions on the robot assembly were the individual component masses

have been lumped. All data was recorded and used in evaluating the constant C. Refer to Table AII and matlab program MMI.m:

$$C=\frac{m_{total}\times L\_AC\times CG_{total}}{I_o}=\frac{34.2862grams\times 0.3429m\times 0.3077m}{3.3155}=1.0911 \quad \text{(A10)}$$

Figure A3 contains the output of the accelerometer signal and Figure A4 is an enlarged view. With the motor removed, during free fall the magnitude of the signal is $\approx$ -1.25 which results in error of:

$$C_{tolerance}=\frac{1.0911-1.25}{1.0911}=-14.56\% \quad \text{(A11)}$$

As a check, another immediate relationship which can be used to determine the accelerometer scaler(C) is to divide the position of the accelerometer location by the composite centre of mass: L_AC/CG_{total} = 0.3429/0.3077 = 1.1144, which results in an error of:

$$C_{tolerance}=\frac{1.0911-1.1144}{1.0911}=-2.135\% \quad \text{(A12)}$$

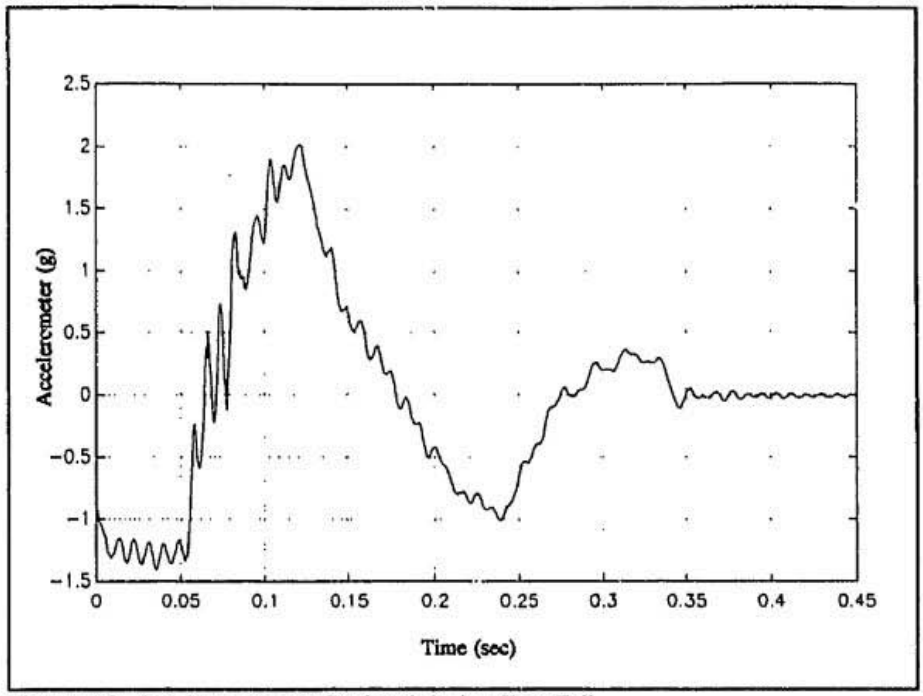

Figure A3: Accelerometer (AC) signal during Free Fall.

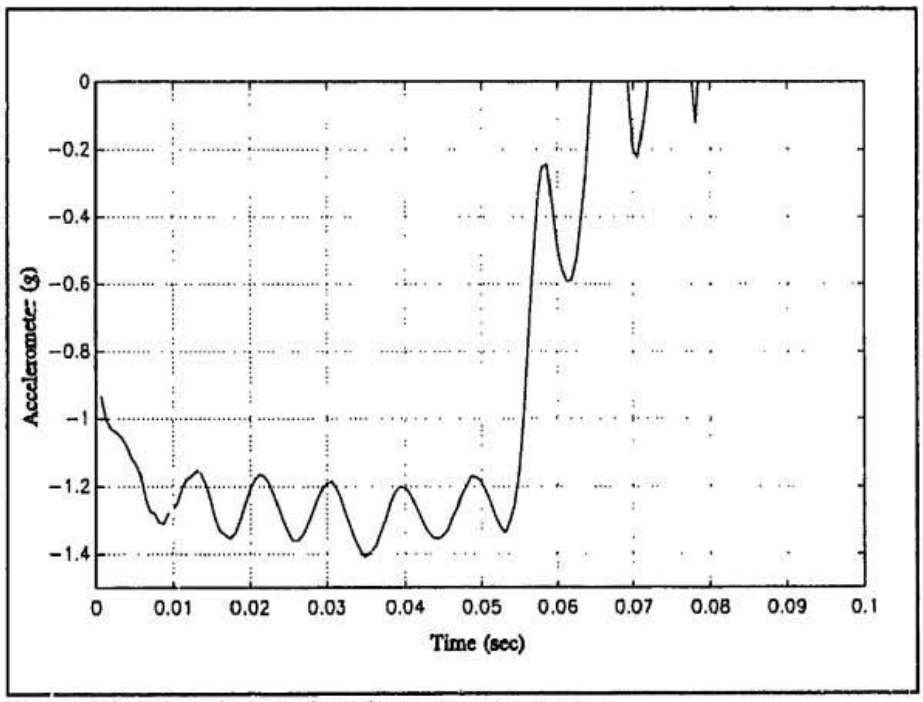

Figure A4: Enlarged view of accelerometer sensor output.

A.5 Load Cell #1 Output

Physically, the load cell which measures the force being generated on the robot, F_{robot}, is displaced from the robot arm's centre of gravity. As with the accelerometer signal output, LC_1 requires interpretation. Figure A5 illustrates the position of LC_1.

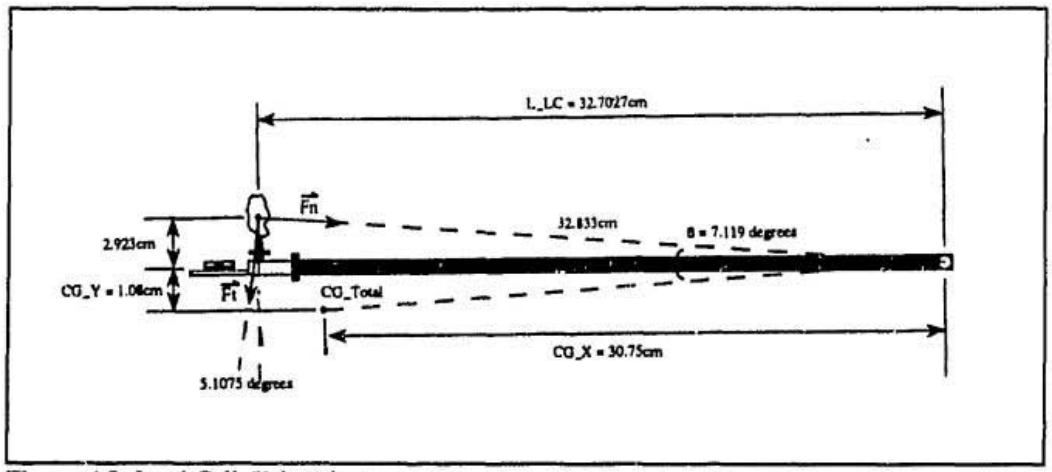

Figure A5: Load Cell #1 location.

During excitation (process of contact), the forces acting on LC_1 can be resolved into normal and tangential components:

$$\Sigma F_n = m \times a_n \tag{A13}$$

and

$$\Sigma F_t = m \times a_t \tag{A14}$$

The load cell is not calibrated for torsional excitation forces or lateral induced forces nor should the devices be subject to them (Entran Spec. Sheet). Therefore, even if F_n could be evaluated it is of no use. It should be noted that the magnitude of the load being supported by LC_1 in conjunction with the maximum effective drop height, 2.5cm, minimizes the potential risk of damage to the load cell. However, these effects still contribute to the overall output of the load cell.

Mounted on the upper section of LC_1 are four constituent masses: (1) Robot_LC_Couple_Clamps_Mass = 0.25/2g, (2) Robot_LC_Carriage_Mass = 0.75g , (3) Plastercine_Mass = 6.75g and (4) LC_1_Y02_Sensor_Mass = 3.13/3g which total 8.668g

During free fall the load cell output, measured from the Keithley side of the analog filter is 2.88volts (see sensor generic schematic in Appendix C, Figure C6). The predicted tangential force component in terms of voltage is:

$$\Sigma F_t(v) = M_{top} \times g \times \frac{L\_LC}{CG_{total}} \times LC1_{gain} \times LC2_{Sensitivity} \times EX_{ratio} \times COS(5.1) \approx 2.76375v \quad \text{(A15)}$$

where M_{top} = 0.008668Kg
g = gravitation constant
L_LC = 0.327027m
CG_Total = 0.3077m
$LC1_{gain}$ = 2596.58
$LC1_{Sensitivity}$ = 17.725mV/N
EX_{ratio} = 10/15

Thus, 2.76375/2.88 => 95.96% of the output is being contributed by tangential forces and ≈4.04% by normal forces. During environment interaction the contribution of the tangential and normal forces will vary due to a variety of factors, such as, the impact force upon contact, friction forces and the shifting centre of mass. All of these contributions are difficult to quantify.

A.6 Spring Constant Evaluation

The same test jig used in the calibration of Proximity sensor One was use to determine the spring constant, K_c, of the physical spring used in the direct-drive arm. The reflector disk was removed and replaced with a flat support surface made out of aluminum and the jig was mounted vertically allowing gravity to compress the spring. Table AIII contains the mass verses compression data and Figure A6 illustrates the force displacement relationship. The first reading is the reference point from which all other data points were measured. Graphite between the slider and the slider guide reduced the erroneous effects caused by friction. Note that the first point is off the average slope and was therefore omitted form the slope calculation. The smaller the mass the larger the displacement error caused by friction. The average slope was calculated from data points 2 through 6 which represents the spring constant used in both the numerical simulation program and the robot arm feedback control interface program: $K_c = 18.330286$N/m

Table AIII: Spring constant data.

data	Mass (grams)	Displacement (inches)
1	20	0.0
2	30	0.153
3	40	0.3580
4	50	0.568
5	60	0.7725
6	70	0.9970

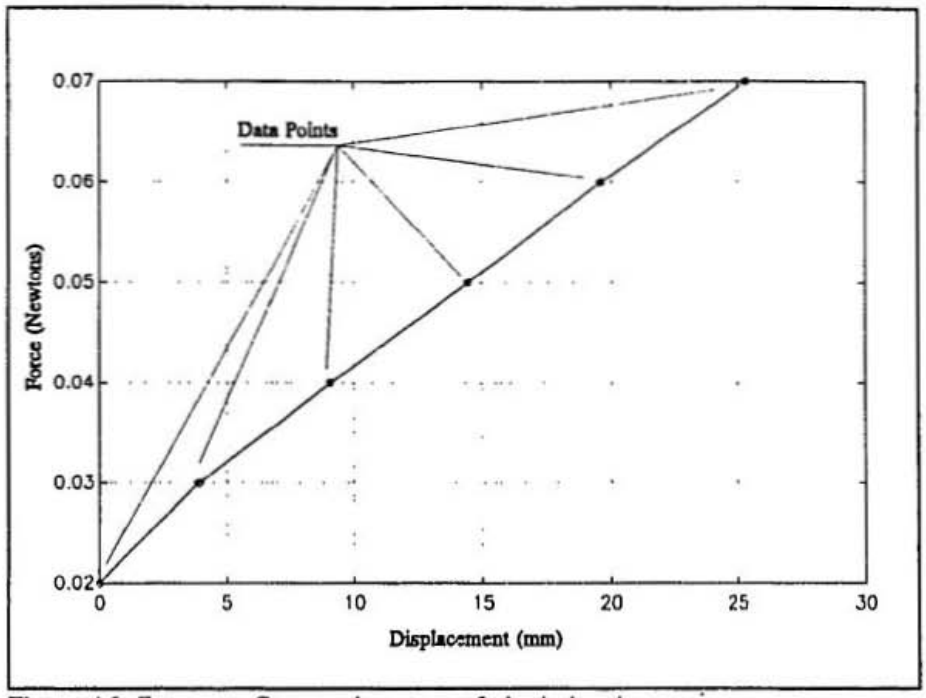

Figure A6: Force -vs- Compression curve of physical spring.

A.7 Motor Resistance and Inductance Evaluation

The following two tables contain the armature resistance, R_a, and armature inductance, L_a, measurements of the permanent magnet DC motor used in the robot arm.

Table AIV: Permanent magnet DC motor winding resistance data points.

num	Resistance (Ω)	num	Resistance (Ω)
1	9.4	11	8.1
2	8.7	12	8.9
3	9.0	13	8.2
4	9.5	14	8.8
5	10.8	15	7.7
6	10.0	16	8.6
7	8.4	17	8.0
8	8.1	18	8.1
9	8.4		
10	9.2		
Average = 157.9/18 = 8.772Ω			

Table AV: Inductance measurements, L_a.

num	Inductance (mH)
1	4.26
2	4.22
3	4.28
4	4.26
5	4.25
6	4.31
Average = 25.58/6 = 4.263mH	

From R_a and L_a the electrical time constant can be evaluated:

$$\tau_e = \frac{L_a}{R_a} = \frac{4.262mH}{8.772\Omega} = 0.00048596\mu sec \qquad \text{(A16)}$$

and the motor's corresponding electrical bandwidth determined:

$$BW_{electrical} = f_c = \frac{R_a}{2 \times \pi \times L_a} = 327.5Hz \qquad \text{(A17)}$$

Both variables were measured using a multimeter. During the measurement procedure, the rotor was rotated in equal increments to obtain an average value for the parameters. This helped average the varying effects of commutation resistance, winding resistance, permanent magnet non-uniformity, winding inductance and other factors which effect these parameters. Since the motor is energized for less than ½ second during each experiment, motor heating is negligible and the effect of temperature on these parameter can be ignored.

A.8 Motor Mass Moment of Inertia

The permanent magnet DC motor rotor diameter = 19.66mm and its mass = 37.33g. The motor rotor takes the form of a circular cylinder. Based this information an approximation of the rotor's mass moment of inertia can be evaluated:

$$I_{rotor} = \frac{r^2 \times m}{2} = \frac{1}{2} \times \left[\frac{0.01966m}{2}\right]^2 \times 0.03733Kg = 0.0000018037Kgm^2 \qquad \text{(A18)}$$

A.9 Motor Viscous Damping

The interaction of the permanent magnet field with the motor's armature iron core results in a viscous retarding force, B_m. Motor bearings also contribute to the total viscous damping effects. Two experiments were conducted, one with the motor removed and one with the motor installed. The release height is 2.5cm with respect to the center of gravity. Figures A7 through A10 contain the sensor output data.

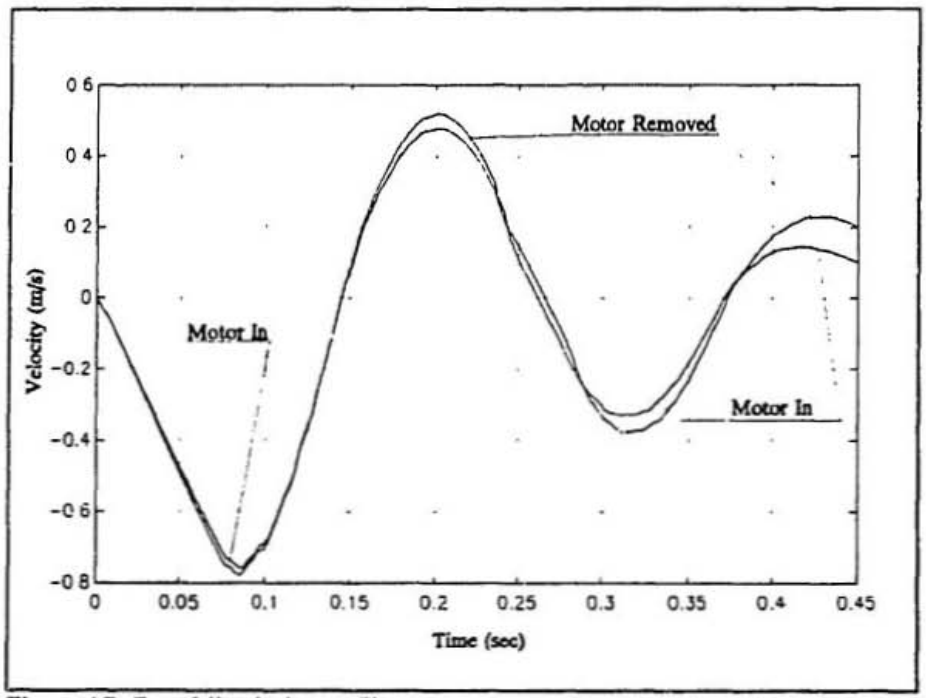

Figure A7: Free fall velocity profile.

From the free fall portion of LC_1, F_{robot} plot, is extremely difficult to obtain an accurate magnitude reading because the vibrational modes of the robot arm are superimposed on the signal. Figure A10 is a filtered and enlarged view of F_{robot}. Clearly, there is a measurable force difference. At t=0.0643s, $F_{robot(m)}$ = -0.2830N and F_{robot} = -0.3005N, which F_{diff}= 0.0175N. Since the experiment output has been mapped to the numerical simulation F_{diff} must be unmapped: F_{diff} = 0.0175/2.8665 = 0.006105N

(see Section 3.4.1.3, Equation 21). This is the effective retarding force being generated by the motor at t=0.0643s. Converting this force into a scalable viscous damping force is accomplished by dividing F_{diff} by the instantaneous velocity and transferring the result to the motor shaft:

$$B_{m(scalable)} = \frac{F_{diff} \times L_{LC}}{Velocity} = \frac{0.006105N \times 0.327027m}{0.6139m/s} = 0.003252158Ns$$

Hence, the absolute viscous effects of the motor on the center of gravity is given by:

$$B_m = \frac{B_{m(scalable)}}{CG_{total}} = \frac{0.003252158}{0.3077} = 0.010569Ns/m \qquad \text{(A20)}$$

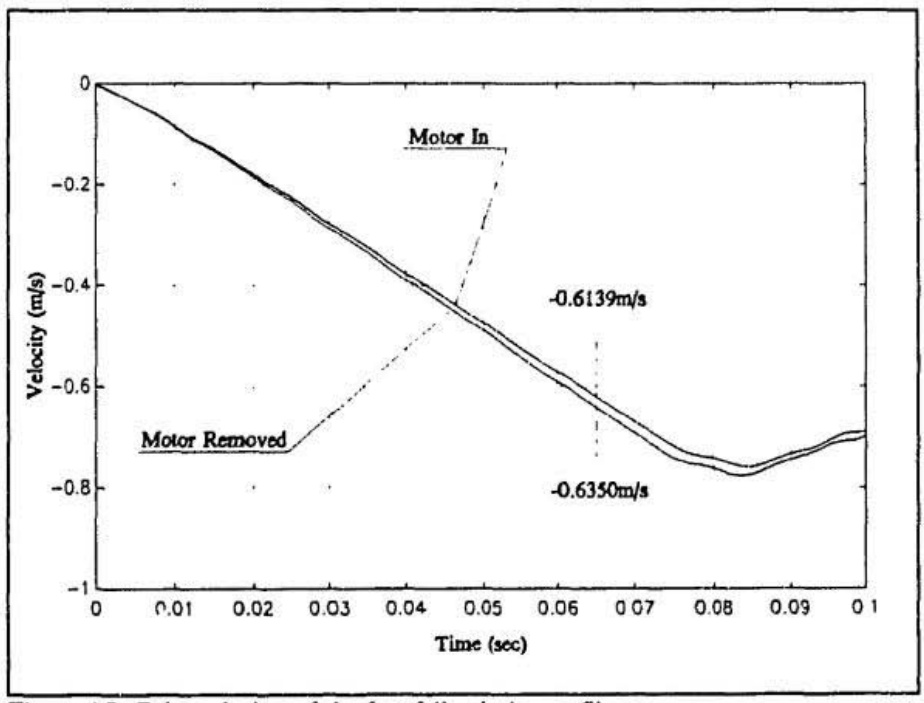

Figure A8: Enlarged view of the free fall velocity profile.

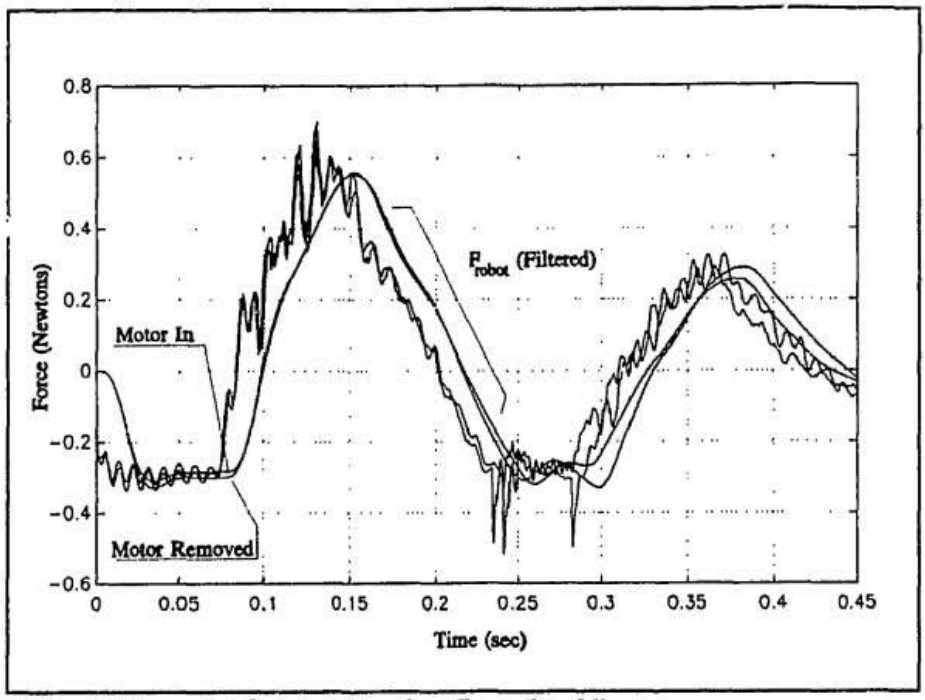

Figure A9: Generated force on the robot, F_{robot} - free fall.

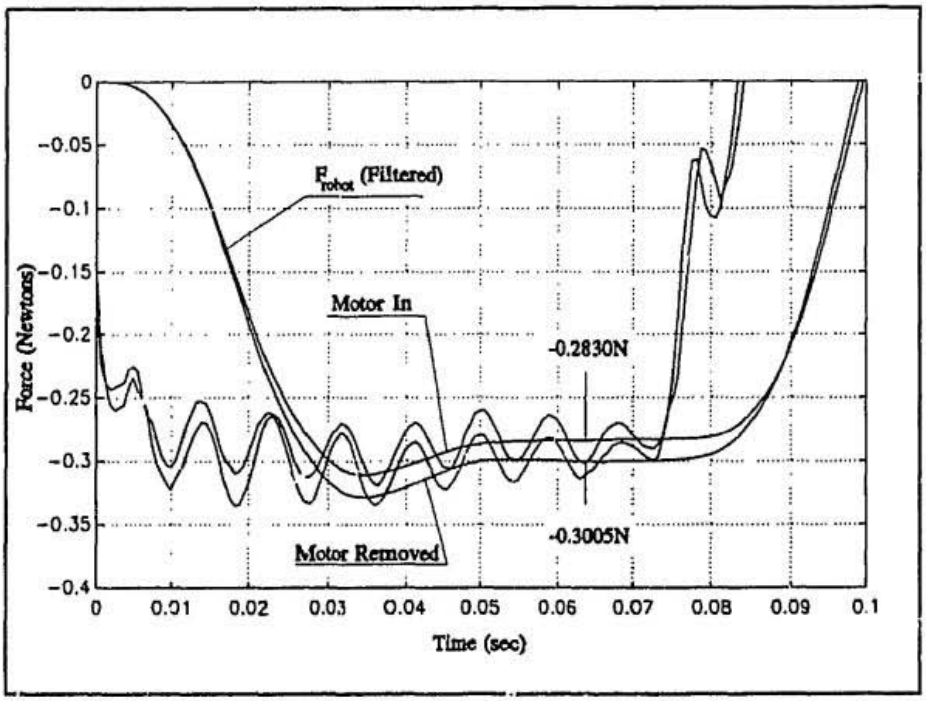

Figure A10: Enlarged view of F_{robot} - free fall.

Appendix B

Interactive Ribber Tip Analysis

B.0 Non-Linear Rubber Tip Model

Figure B1 describes the relationship between applied pressure and percent compression of natural rubber impregnated with bubbles. The material and original compression curve were obtained from INSTRUMAR. Table BI contains the estimated data points from the original compression curve. The data points were obtained with the use of a set of dividers and a ruler, thus, the units of Table BI are in centimetres. Using the conversion factors Xscale = 6.211 and Yscale = 0.0659, Figure B1 is realized.

The compression axis is normalized to 1, hence, 0.1 implies 10% compression and in a similar manner 0.6 implies 60% compression. There are two separable phases exhibited which are distinguishable around 55% compression. Up to 55% compression the data points are approximately linear. Above 55% the pressure required to compress the rubber increases exponentially. This transition is called void fraction and occurs when the impregnated bubbles have collapsed.

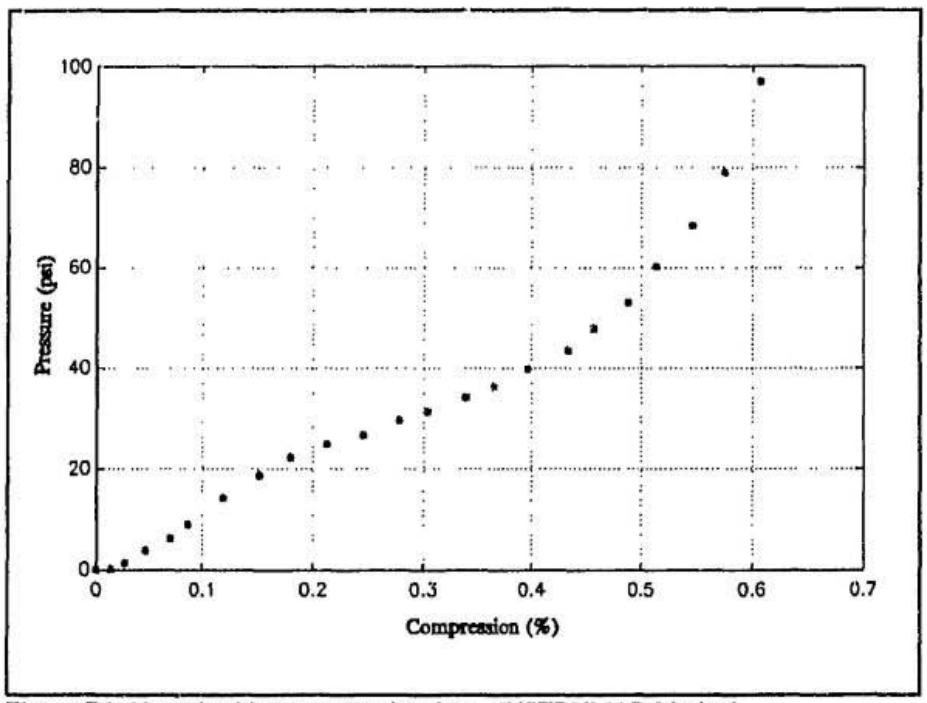

Figure B1: Natural rubber compression data - INSTRUMAR Limited.

Table BI: Natural rubber compression-vs-pressure data.

data	Pressure(x) (cm)	Compression(y) (cm)	data	Pressure(x) (cm)	Compression(y) (cm)
1	0.0	0.0	13	5.04	4.6
2	0.02	0.2	14	5.5	5.1
3	0.2	0.4	15	5.85	5.5
4	0.6	0.69	16	6.4	6.0
5	1.0	1.05	17	7.0	6.55
6	1.45	1.3	18	7.7	6.9
7	2.3	1.8	19	8.53	7.39
8	3.02	2.28	20	9.7	7.8
9	3.58	2.72	21	11.0	8.28
10	4.01	3.22	22	12.7	8.7
11	4.3	3.7	23	15.62	9.2
12	4.77	4.2			

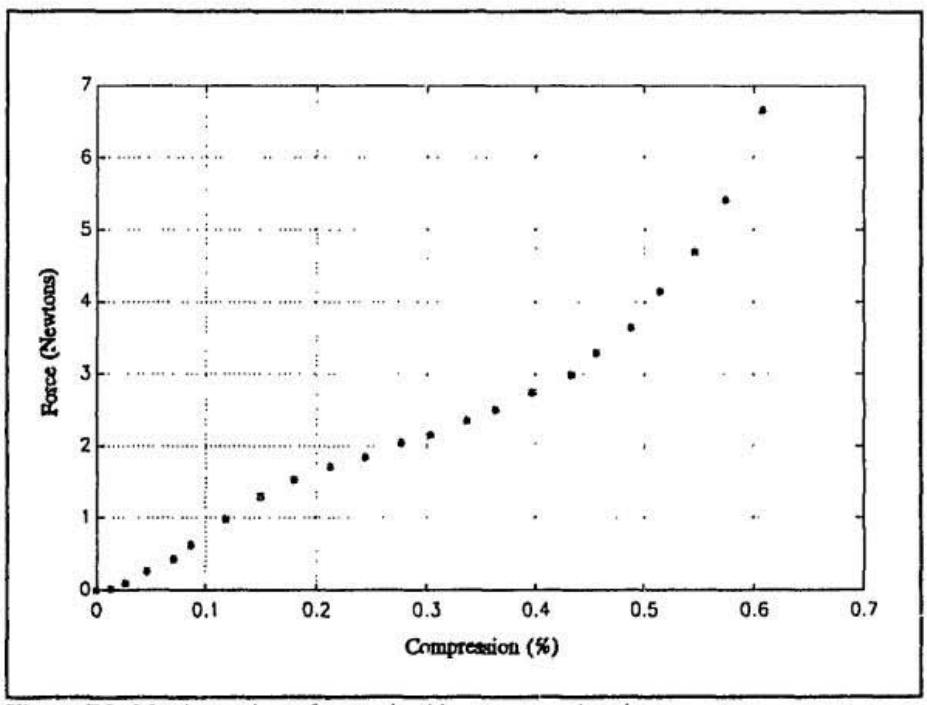

Figure B2: Metric version of natural rubber compression data.

Figure B2 is a direct mapping of Figure B1, however, the data now is represented in Newtons -vs- percent compression.

Mathematically there are numerous methods for generating this type of response: continuous and piece-wise continuous. Based on the need for a simple model required to minimize the software computational time necessary to evaluate the tip response a continuous mathematical model will suffice. Several math functions produce the generic profile: $y=X^3$, $y=aTanh()$, $y=Tan()$ and $ln()$. The natural logarithmic equation was chosen and modified to more accurately represent the tip dynamics. It is mathematically represented by Equation B1 and graphically illustrated in Figure B3.

$$F_{K_{tip}} = K \times \ln\left[\frac{1 + Max\left(\frac{X_1 - X_0 - lo_{tip}}{lo_{tip}}\right)}{1 - Max\left(\frac{X_1 - X_0 - lo_{tip}}{lo_{tip}}\right)}\right] \qquad \text{(B1)}$$

where K = Spring constant scaler = 2.0

Max = tension/compression scaler = 1.525

lo_{tip} = Natural rubber tip length = 0.3175cm

The singular points occur at:

$$Percent_{Comp} = \pm\frac{lo_{tip}}{Max} = \pm\frac{1}{Max} = \pm\frac{1}{1.525} = \pm 0.655 \qquad \text{(B2)}$$

where Max is a scaler which determines the singularity position. Equation B2 is normalized to lo_{tip}.

Figure B3 contains the best curve fit of the natural log function to the data points. The approximation was obtained through trial and error. Figure B4 illustrates the complete tension -vs- compression plot of the natural log approximation. Compression

greater than the singularity point does not exist. In a similar fashion, tension beyond the negative of the singular point does not exist. During software integration the time steps may impose a magnitude jump which overshoots the singular point. Appropriate action is taken if this situation arises.

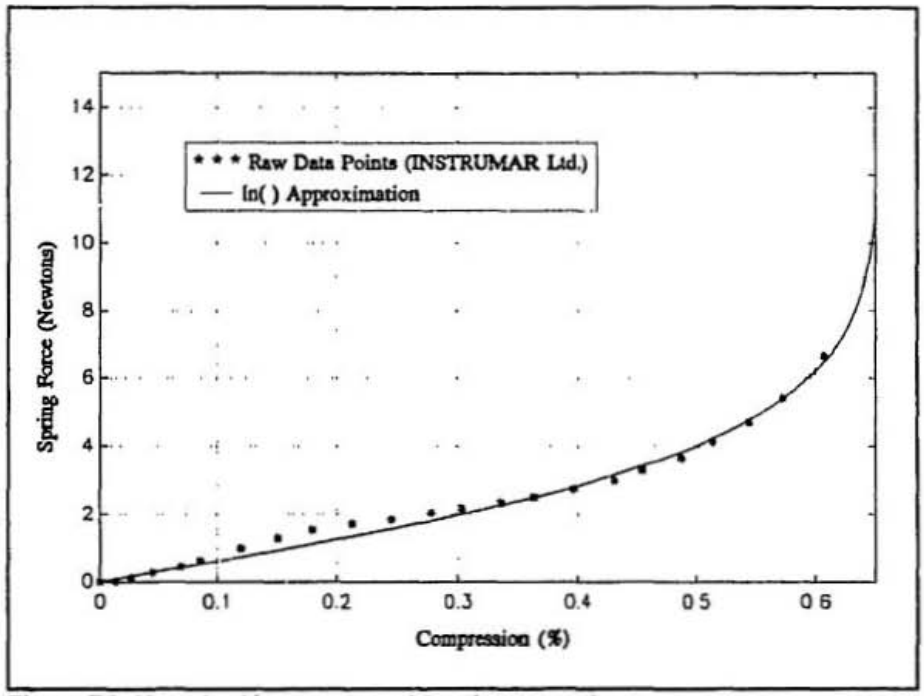

Figure B3: Natural rubber -vs- natural log, ln( ), mapping.

Figure B5 contains the normalized compression and tension plots of K_{tip}.

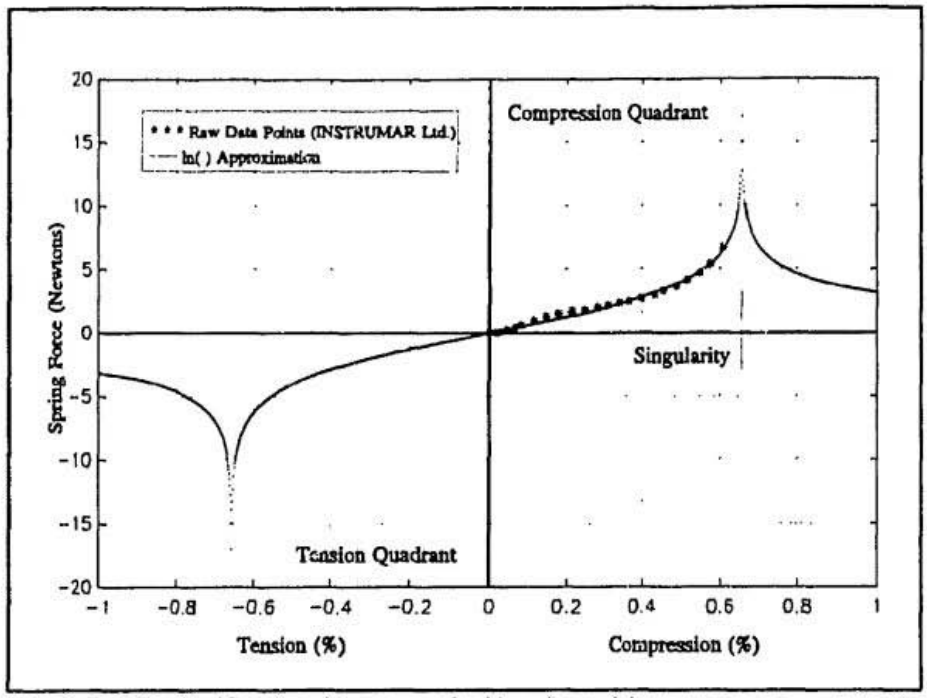

Figure B4: Tension/Compression curve of rubber tip model.

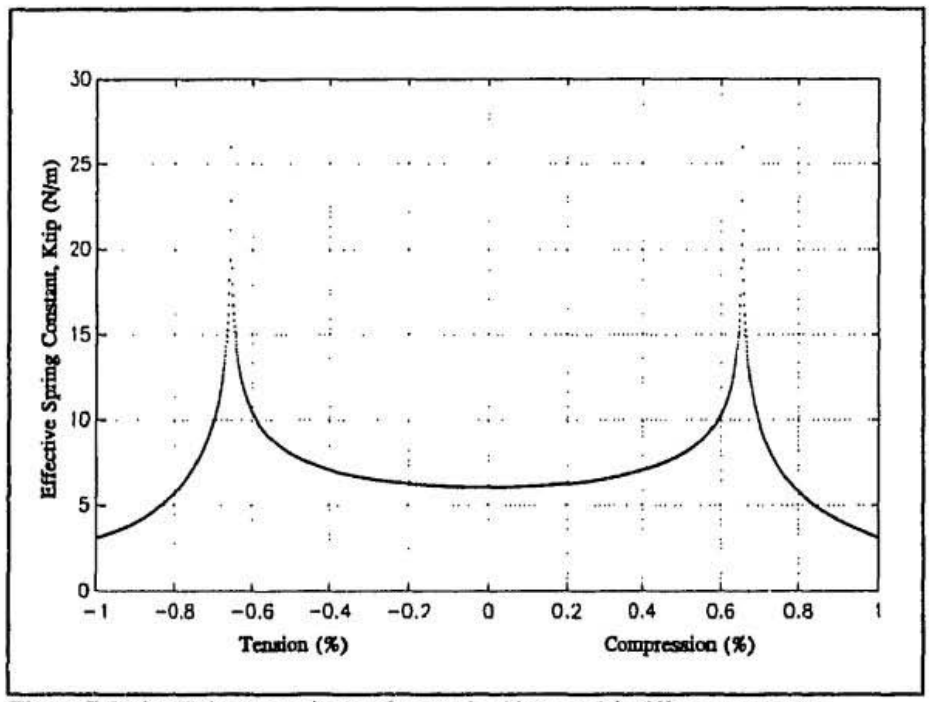

Figure B5: Coefficient magnitude of natural rubber model stiffness parameter.

B.1 Rubber Tip Mass

The mass of the rubber tip used in the experiment was evaluated and used in the numerical simulation. From the two natural rubber samples obtained from INSTRUMAR(DYK Brand, 565-C black open cell sponge) the following data was obtained:

Sample One:

$$Volume_{S1}=15.3\times15.1\times0.635=146.704cm^3$$

Sample Two:

$$Volume_{S2}=15.3\times15.22\times0.3157=73.934955cm^3$$

Their mass was measured to be:

$$Mass_{S1}=0.07139Kg$$

and

$$Mass_{S2}=0.03805Kg$$

Therefore, their densities equal:

$$Density_{S1}=\frac{Mass_{S1}}{Volume_{S1}}=0.000486625\frac{Kg}{cm^3}$$

and

$$Density_{S2}=\frac{Mass_{S2}}{Volume_{S2}}=0.000514641\frac{Kg}{cm^3}$$

which in terms of tolerance is around 5 percent:

$$Tolerance=\frac{Density_{S1}-Density_{S2}}{Density_{S1}}\times100\%=5.44\%$$

Taking their average,
results in an acceptable density for the natural rubber. The mass of the rubber tip is calculated as follows based upon the cylindrical shape of the tip used in the experiment:

$$Avg_{Density} = \frac{0.000486625 + 0.000514641}{2} = 0.0005006 \frac{Kg}{cm^3}$$

$$Volume_{tip} = \pi \times r^2 \times h = (\pi)(0.18034^2)(0.3175) = 0.032439767 cm^3$$

which allows the mass to be calculated as:

$$M_{tip} = Avg_{Density} \times Volume_{tip} = 16.239 \times 10^{-6} Kg$$

Appendix C

Sensor Details

Figures

Tables

C.0 Sensor Details

C.1 Proximity Sensors #1 and #2

There are two proximity sensors used in the experiment. One proximity sensor measures the spring deflection and is referred to as PS_1, the other is used to measures the distance between the *Reflector Disc* and the *Impact Surface*. The latter is referred to as PS_2. Figure 6 indicates the location of PS_1 and Figure 7 indicates the location of PS_2 on the direct-drive robot arm experiment setup (Section 3.4.1). Both proximity sensors consist of a Transmitter(Tx) and a Receiver(Rx) circuit pair, hence, they are further defined as PS_1_Tx, PS_1_Rx, PS_2_Tx and PS_2_Rx. In both cases the Tx's emissions are reflected by the *Reflector Disc*. The intensity of the reflection is measured by the Rx circuit, hence, the distance between the *Reflector Disc* and each proximity sensor can be interpreted. It should be noted that the distance being measured by the sensors are different thus their individual Gain is slightly different and the *Robot Frame Assembly* should be grounded.

The heart of both proximity sensor's operation is a spectrally and mechanically matched Transmitter and Receiver pair manufactured by Texas Instruments, TIL31 and TIL81 respectively. Their matched characteristics make them ideally suited for use together.

C.1.1 Transmitter Circuit

The TIL31 is an infrared emitting diode. Its spectral output is well defined and limited between 875nm and 975nm with peak emissions at 925nm. The main reason for choosing this device is because its emissions are confined to an angular displacement of 10 degrees relative to its optical axis. This enabled a well defined point light source to be focused on the *Reflector Disc* which ultimately increased the accuracy and

repeatability of the both proximity sensor circuits. Figure C1 contains PS_1_Tx and PS_2_Tx schematics. Both circuits are identical.

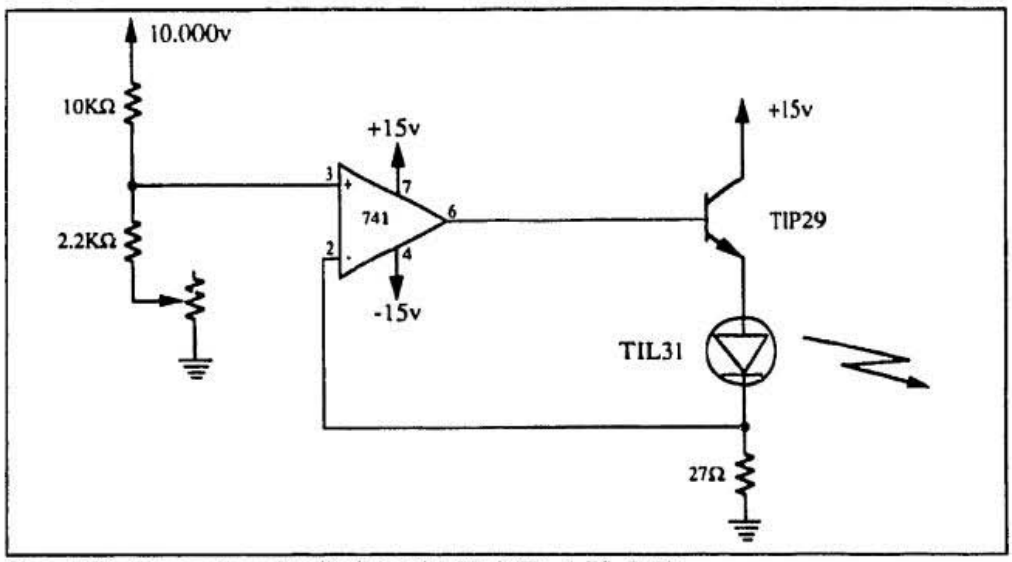

Figure C1: Transmitter circuit schematic: PS_1_Tx & PS_2_Tx.

C.1.2 Calibration

Adjust the 10K potentiometer until the TIL31 continuous forward voltage is 150.0 mA (which is also the transistors collector current). With the 27.0Ω resistor installed, the base voltage of the transistor is approximately 6.38 volts and the output of the voltage divider circuit is 4.05 volts. The greater the collector current the more intense are the IR emissions.

Notes:

- Maximum forward collector current is 200mA.
- +10.000v reference signal is produced by Analog Devices chip 588.

C.1.3 Receiver Circuit

The TIL81 is configured to operate in the phototransistor mode. Its bandwidth is 450 nm to 1100nm and its peak sensitivity is around 910nm. Referring to Figure C2, the Receiver circuit contains three sub-components: Dark Current Zero adjust, Gain and Filter. Covering the TIL81 is a 6mmX6mmX3mm Infrared glass filter. This attenuates all frequencies below 850nm. Figure C2 contains PS_1_Rx schematic and Figure C3 contains PS_2_Rx schematic.

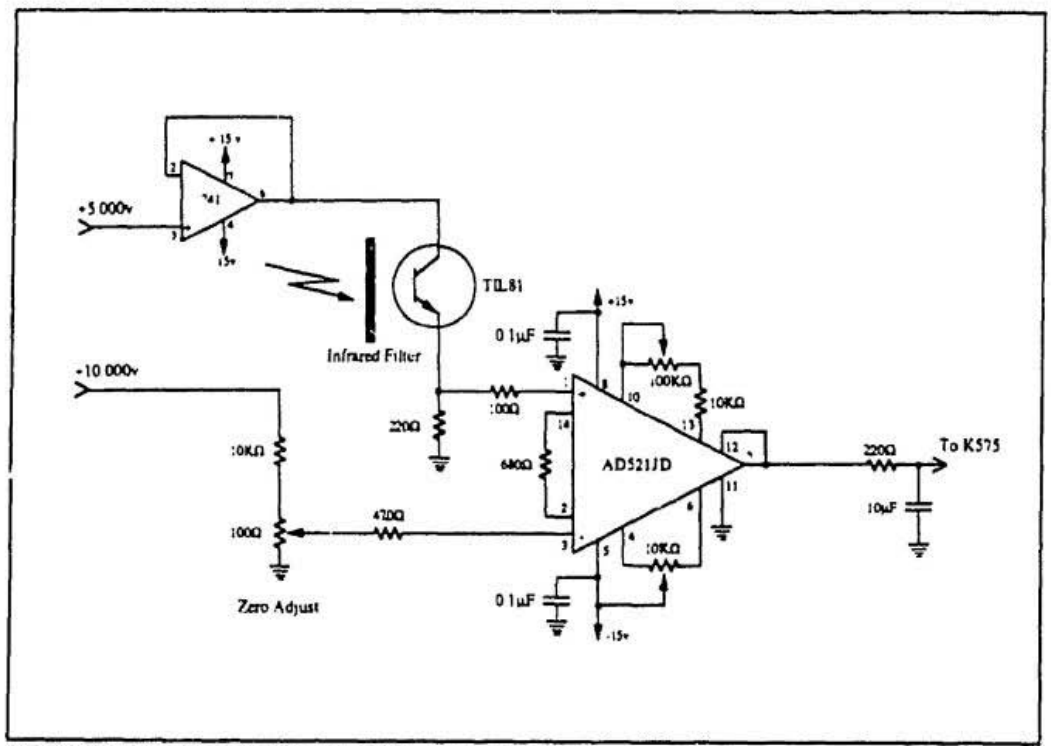

Figure C2: Receiver circuit schematic: PS_1_Rx.

C.1.4 Calibration

Zero Adjust Circuit: The Zero Adjust circuit compensates for the TIL81 dark current. Cover the TIL81 to block out any light which may enter the device. While monitoring the AD521JD output, adjusting the 100Ω potentiometer until a reading of 0.0v

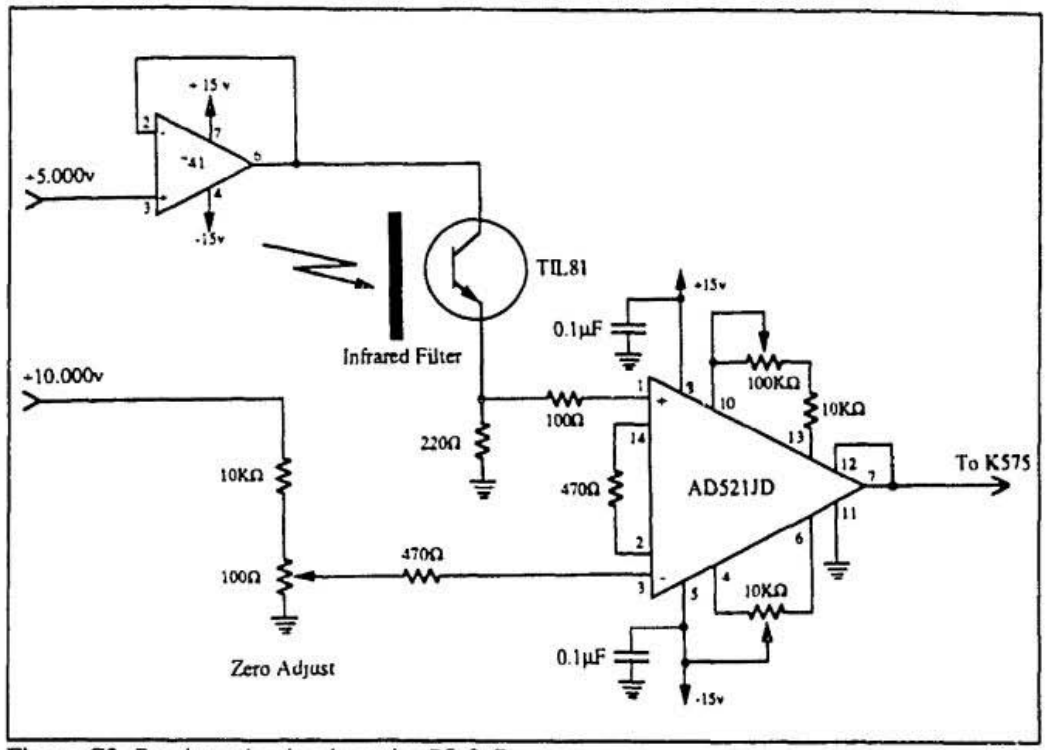

Figure C3: Receiver circuit schematic: PS_2_Rx.

is obtained.

Gain/Zero Adjust: Calibration procedure of each sensor circuit is identical. The gain of the AD521JD chip of is adjusted to 125 for PS_1. The gain of PS_2 is described in the notes below. Connect an appropriate calibration signal, for example, a 10mV DC signal, to the positive input of the AD521JD chip and ground the negative input. Adjust the 100KΩ potentiometer until the appropriate gain is reached. The second required calibration requires both inputs to be grounded. Once the inputs are grounded, adjust the 10KΩ potentiometer until the output is zero volts.

Notes:

- Both circuits do not account for the dark current temperature dependence of the TIL81.

- The experiment setup should be turned on at least 10 minutes prior to data acquisition so thermal effects can stabilize.

- Only PS_1_Rx's output is filtered: f_c = 72.34Hz

- +5.000v and +10.000v reference signals are produced by Analog Devices chip 588.

- During free fall PS_1 is cooled by the surrounding air. This alters both the TIL31 and TIL81 outputs. Black tape wrapped around the sensor reduced this problem to an acceptable level (refer to Figure 6, Sectio 4.3.1).

- PS_2 Gain: This gain is arbitrary in the sense that there is no exact gain value. With the robot arm resting the on the Impact Surface, adjust the 100KΩ potentiometer until the AD521JD output reads approximately 8 volts.

C.1.5 Calibration Detail of PS_1

Calibrating Proximity Sensor #1(PS_1) relied on the design of a mounting platform which would rigidly hold the proximity sensor and the reflector disk assembly unit. This ensured accurate results by eliminating errors introduced by the tedious procedure necessary to obtain the compression - voltage relationship. Specific examples which would contribute to the error if the test jig were not used are: holding the reflector disk in a particular position during the 2 seconds required for the software program to acquire the data, maintaining the digital calipers in position and not contaminating the reflector disk surface with finger debris. The test jig is illustrated in Figure C4.

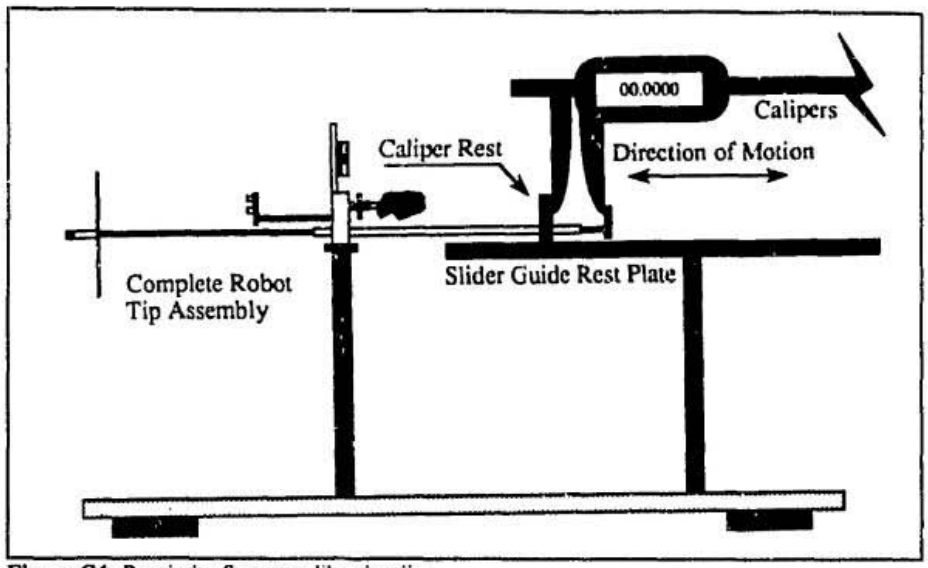

Figure C4: Proximity Sensor calibration jig.

As the calipers are opened the *slider* moves through the *slider guide* and in the process compresses the spring. The *Reflector Disc Assembly* moves toward PS_1, hence, the compression - voltage relationship can be obtained.

Prior to calibration the gain and offsets of the PS_1 differential circuitry were adjusted such that lo_{spring} = 0.0 volts and maximum compression was 10.0 volt. This allowed for maximum resolution given that the A/D converter's input range is defined as $\pm$10.0 volts. Therefore, during compression the proximity sensor circuit would be positive and during tension a negative voltage would be produced. Under no load, lo_{spring} the output would equal 0.0 volts.

The precision calipers were mounted on the slider guide rest platc which enabled the natural length(no load condition) of the spring to be zeroed with the calipers. Adjusting the calipers automatically compressed the spring giving an accurate displacement reading during the experiment. Two calibration tests were conducted with displacement ranging from 0.0 inches to 1.75 inches in increments of 0.1 inches. The results were recorded and are contained in Table CI. Figure C5 highlights the experiment results. Overlaid in the same figure is a third order least

squares approximation of the data points and Equation CI represents the relationship between PS_1 output and actual compression.

$$Spring_{displacement} = A \times V^3 + B \times V^2 + C \times V^2 + D \qquad \text{(C1)}$$

where
A = PS_1_1 = 0.04594217515180
B = PS_1_2 = -0.81158674281651
C = PS_1_3 = 8.11956000994870
D = PS_1_4 = 0.06798466446682

NOTES: The first data points were forced equal to 0.0volts.

Proximity Sensor Data used in calibrating the spring displacement is contained in Table CI.

Table CI: Proximity Sensor #1 calibration data.

X (in)	Maximum (volts)	Minimum (volts)	Average (volts)	Maximum (volts)	Minimum (volts)	Average (volts)
0.0	0.000000	0.000000	0.000000	0.000000	0.000000	0.000000
0.1	0.367695	0.365327	0.366605	0.304255	0.301865	0.303172
0.2	0.669147	0.666763	0.668057	0.652193	0.649800	0.651119
0.3	1.054007	1.051595	1.052888	1.031766	1.029332	1.030651
0.4	1.445904	1.443547	1.444832	1.429695	1.427337	1.428618
0.5	1.880795	1.878362	1.879671	1.870907	1.868459	1.869793
0.6	2.366506	2.364125	2.365412	2.349123	2.346762	2.348057
0.7	2.903598	2.901227	2.902507	2.903598	2.901227	2.902507
0.8	3.501770	3.499372	3.500684	3.470738	3.468333	3.469645
0.9	4.132306	4.129967	4.131244	4.101518	4.099130	4.100437
1.0	4.797991	4.795604	4.796891	4.779691	4.777283	4.778612
1.1	5.515998	5.513591	5.514899	5.502691	5.500278	5.501604
1.2	6.261889	6.259491	6.260798	6.251534	6.249120	6.250433
1.3	7.026100	7.023696	7.024992	7.011021	7.008553	7.009899
1.4	7.735752	7.733302	7.734630	7.738585	7.736124	7.737463
1.5	8.428743	8.426306	8.427625	8.416887	8.414381	8.415732
1.6	9.013021	9.010574	9.011904	9.006190	9.003686	9.005033
1.7	9.462851	9.460410	9.461738	9.476068	9.473577	9.474939
1.75	9.657035	9.654535	9.655868	9.651205	9.648666	9.650035

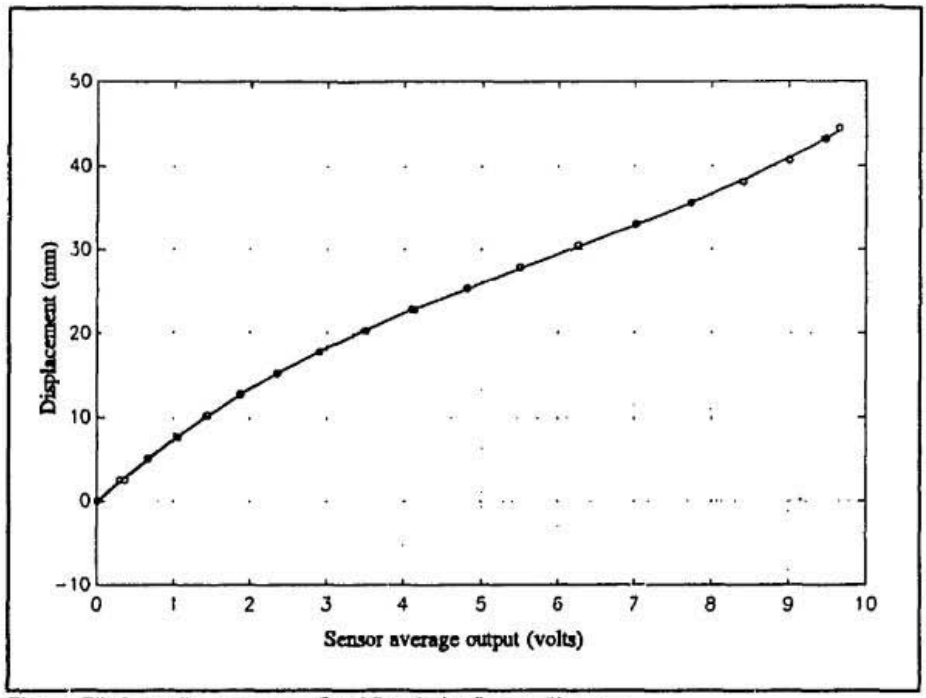

Figure C5: Least Squares curve fit of Proximity Sensor #1 output.

C.2 Accelerometer and Load Cell #1 & #2 Sensors

The three sensors are manufactured by *Entran Devices*. They are full bridge-semiconductor based devices and are provided with an open ended zero adjust half-bridge. Table CII summarizes each sensor circuit calibration specifics and also lists some other important information.

Table CII: AC, LC_1 and LC_2 specifications.

Parameter\Sensor	Accelerometer	Load Cell #1	Load Cell #2
Model	EGA-125F/5-5D	ELF-TC13/5-5	ELF-TC13/5-5
Serial Number	93K93J07-A04	93K93J16-Y02	93K93J16-Y03
Range	±5 g's	±5 Newtons	±5 Newtons
Sensitivity (@15v)	14.6mV/g	17.725mV/N	15.354mV/N
AD521JD Gain	125	2596	241
Filter Cutoff	72.34Hz	72.34Hz	N/A
Rg	470Ω	22Ω	220Ω
R1	802Ω	1781Ω	1924Ω
R2	810Ω	1777Ω	1926Ω
R3	794Ω	1775Ω	1917Ω
R4	794Ω	1772Ω	1920Ω

C.2.1 Calibration

It should be noted that the gain values were obtained through trial and error. Free fall tests were conducted during which the three sensor circuit outputs were monitored. Because the Keithley data acquisition system AD converters accept ±10.0 volts, the gains of each circuit were adjusted to maximize the voltage range. Upon completion of the trial and error free fall experiments, a 10.0mv signal applied to

each of the sensor inputs aided in obtaining the overall individual circuit gains. As a calibration check, 10g and 50g masses were placed on both load cell sensors and based upon their respective gains, verified. The accelerometer circuit gain was not verified through any special test due to the difficulties associated with doing so. Free fall tests concluded, however, that the accelerometer responded with an acceptable accuracy.

Calibration procedure of each sensor circuit is identical and exactly the same as PS_1 and PS_2. The gain of the AD521JD chip is adjusted to 125, 2596 and 241 as recorded in Table CII. Connect an appropriate calibration signal, for example, a 10mV DC signal, to the positive input of the AD521JD chip and ground the negative input. Adjust the 100KΩ potentiometer until the appropriate gain is reached. The second required calibration requires both inputs to be grounded. Once the inputs are grounded, adjust the 10KΩ potentiometer until the output is zero volts.

Notes: - Only the accelerometer sensor and Load Cell #1 are filtered prior to being sampled.

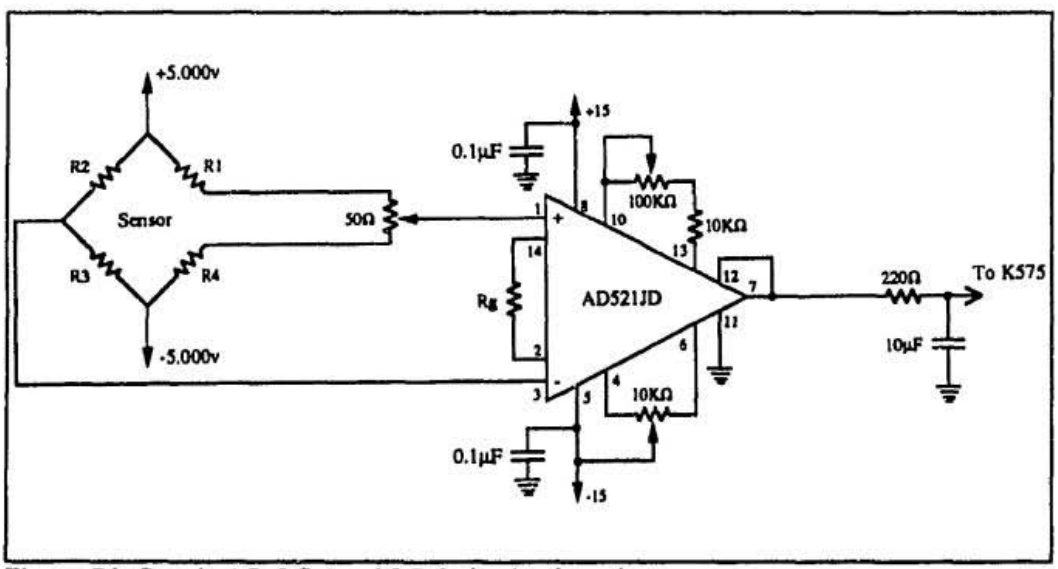

Figure C6: Generic AC, LC_1 and LC_2 circuit schematic.

C.3 Precision Voltage Reference

Generating the precision voltage references required by the five sensors is accomplished using the Analog Devices AD558JQ voltage reference chip. Precision is maintained up to 12bits. Figure C7 contains the +10.0v reference schematic and Figure C8 contains the ±5.0v reference schematic.

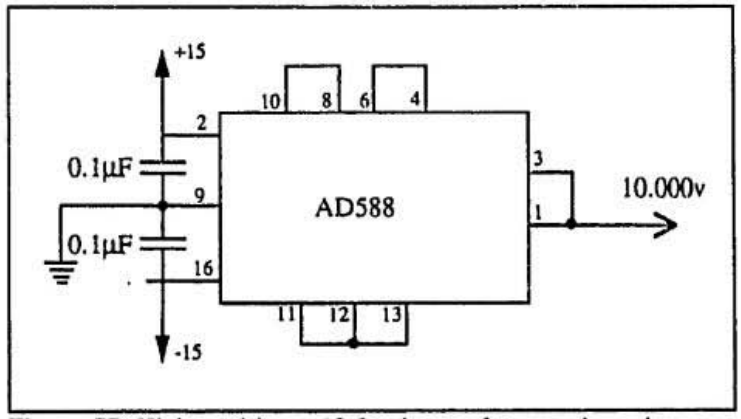

Figure C7: High precision +10.0 voltage reference schematic.

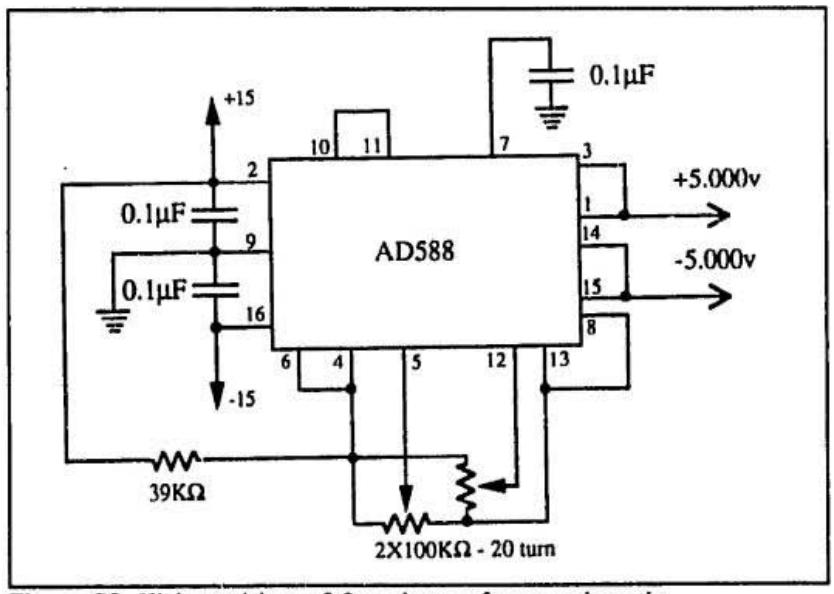

Figure C8: High precision ±5.0v voltage reference schematic.

C.4 Motor Driver Circuit

Figures C9 and C10 contain the motor driver circuit schematics. There are three main sub-circuits: Current limit circuit, Voltage Controlled Current Source (VCCS) and a Shut Down circuit. The first stage divides the DAC voltage in two. This limits stage one's output voltage between ± 5.0v because the maximum DAC range is ± 10.0v. Stage two consists of a VCCS which provided an accurate method of motor torque control. Maximum torque current is limited by the maximum output of Stage one and equals ± 5.0A. Control of the feedback loop is provided by a power operational amplifier, model PA03, manufactured by APEX. Its open loop gain bandwidth is several decades greater than required by the experiment. To ensure closed loop stability the bandwidth of the VCCS should be at least reduced to the motor bandwidth: 327.5Hz. Using the Rate of Closure Technique(APEX application note 16) a 10μF capacitor in series with a 150Ω resistor limited the bandwidth to around 100Hz. This bandwidth also limits the robot's vibrational modes from feeding back and causing instability. Figure C10, stage 3, provides a means by which the PA03 can be turned off. If for some reason the Motor current exceeds 5amps stage 3 will disable the VCCS. Upper and Lower current limits are calibrated using +Vref and -Vref respectively. By placing a voltmeter at +Vref, the 200Ω resistor of the voltage divider circuit allows the upper current limit to be set. The voltage reading is one to one with the current. Adjustment of the lower current limit is exactly the same. To reset the VCCS, if disabled, press and release the Preset switch.

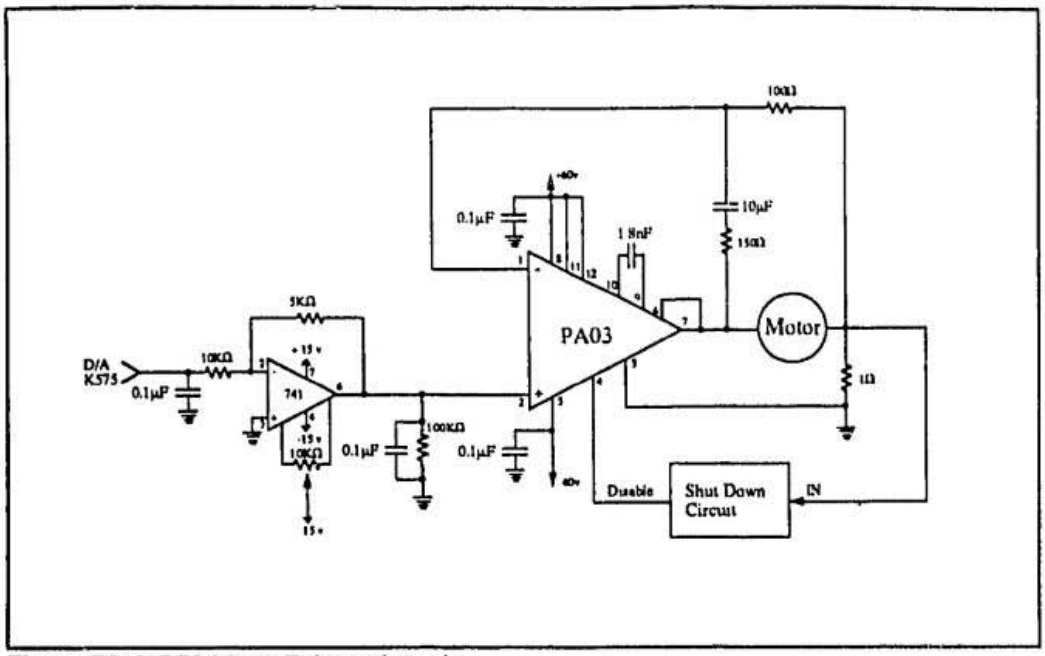

Figure C9: VCCS Motor Driver schematic.

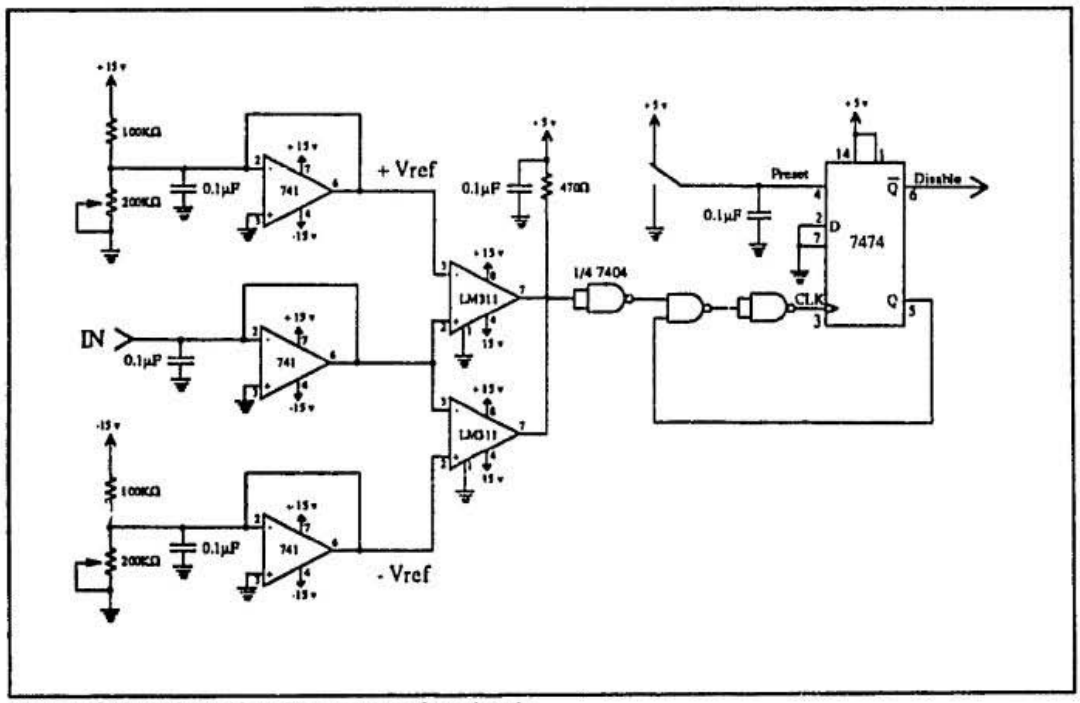

Figure C10: VCCS Shut Down protection circuit.

C.5 Solenoid Release Circuit

Initiating the experiment is accomplished with the solenoid release circuit. It is a Voltage Controlled Current Source. A start pulse originating from the control software activates the VCCS which in turn energizes the solenoid. As the solenoid flux return plate retracts the robot arm is released. Figure C11 contains the solenoid release circuit.

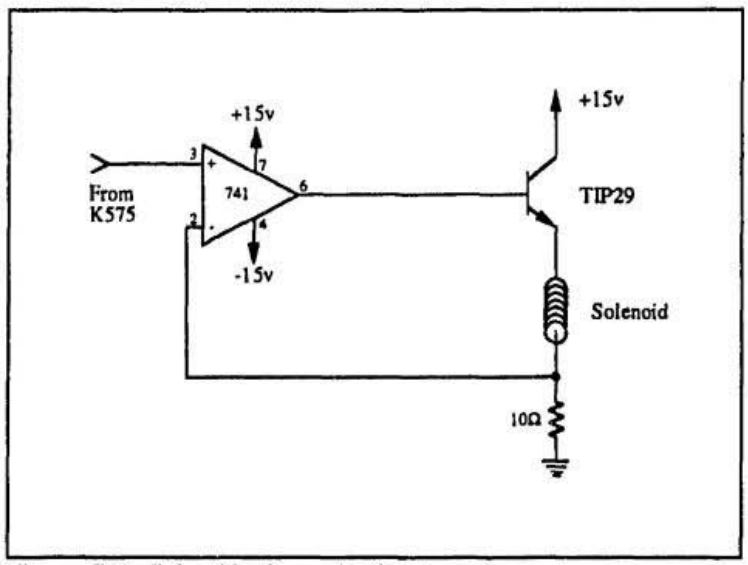

Figure C11: Solenoid release circuit schematic.

Appendix D

Multiplexed Signal Reconstruction

Figures

D.0 Signal Reconstruction Overview

The numerical simulation control algorithm is based on the simultaneous sampling of all six sensors. This was also desired in the direct-drive robot arm experiments. Since the K575 contains a single A/D converter chip the sampled sensors in the experiment setup were multiplexed. For proper operation of the feedback control algorithm it is required to reconstruct the channel signals to make not only the converter conversion time transparent but also the delay associated with channel selection.

The following three pieces of information are required for reconstructing the five channels to *mimic* simultaneous sampling:

1) Adjacent channel delay - (Section D.1).

2) Sampling rate, Δt - (Section D.2).

3) Instantaneous magnitude time rate of change for each channel - (Section D.3).

They are individually addressed in the following sections and examples of the reconstructed channel signals are compared to their original counterparts.

D.1 Adjacent Channel Delay

The time delay between adjacent channel signal acquisition is predetermined. It consists of the time delay associated with channel selection and signal conversion. Both delays are very small and their evaluation requires a separate experiment from the main experiment. The methodology employed in estimating this time delay is indirect, however, extremely effective. All five channels of the Keithley 575, 0 through 4, are tied together and a 200Hz, 10v peak triangular reference signal connected to Channel 0. Channel 0 is the reference channel. It is assumed here that

sufficient delay is incorporated into the sampling rate to account for setup and hold times of the channel selection and A/D converter control vectors. Therefore, we know that the slope, S_{ref}, of the triangular wave's rising edge is :

$$S_{ref} = \frac{4 \times V_{peak}}{T} = \frac{4 \times 10}{0.005} = 8{,}000 V/\text{sec} \qquad \text{(D1)}$$

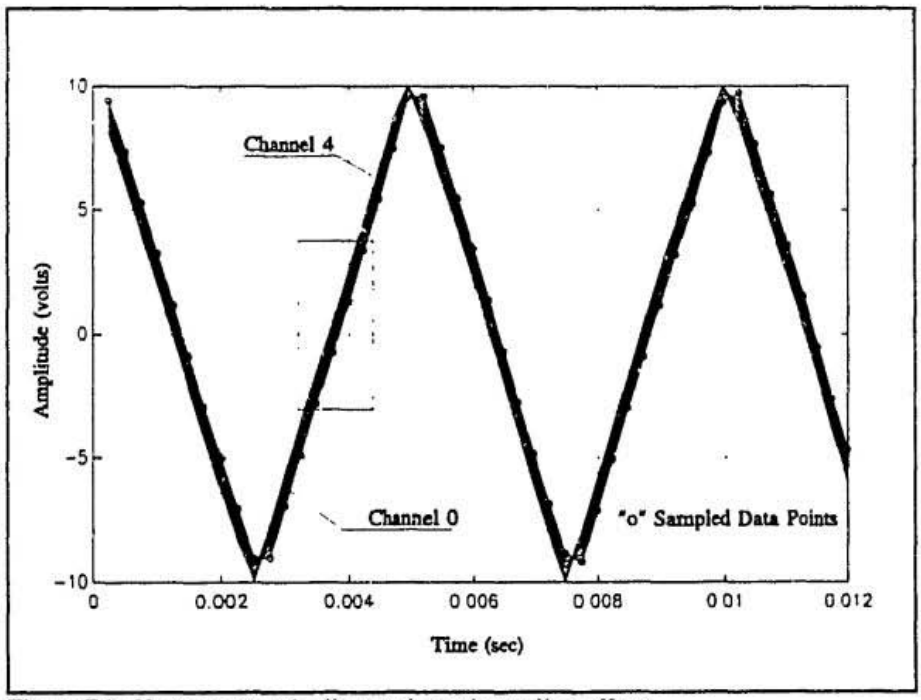

Figure D1: Uncompensated adjacent channel sampling effects.

The five channels are sampled sequentially and at T = 1/4004Hz intervals and stored in a 1000 element array. Figure D1 illustrates this point. The index data points, represented by "o", are sampled data points of Channel 0. These reference points indicate the beginning of the sample sequence and are T=1/4004 ≈ 0.00024975s apart. Figure D2 is an enlarge view of Figure D1. The reference channel is indicated along with the corresponding amplitude values of the remaining 4 channels. The vertical group of amplitude data points, "o", would coincide with

each other if there was no time delay associated with channel selection and A/D conversion. Since the reference signal slope is known, S_{ref}, and the voltage difference between adjacent channels can be determined by the general equation:

$$V_{diff}[i]=V[i]-V[i-1] \qquad \text{(D2)}$$

where i = 1, 2, 3, 4

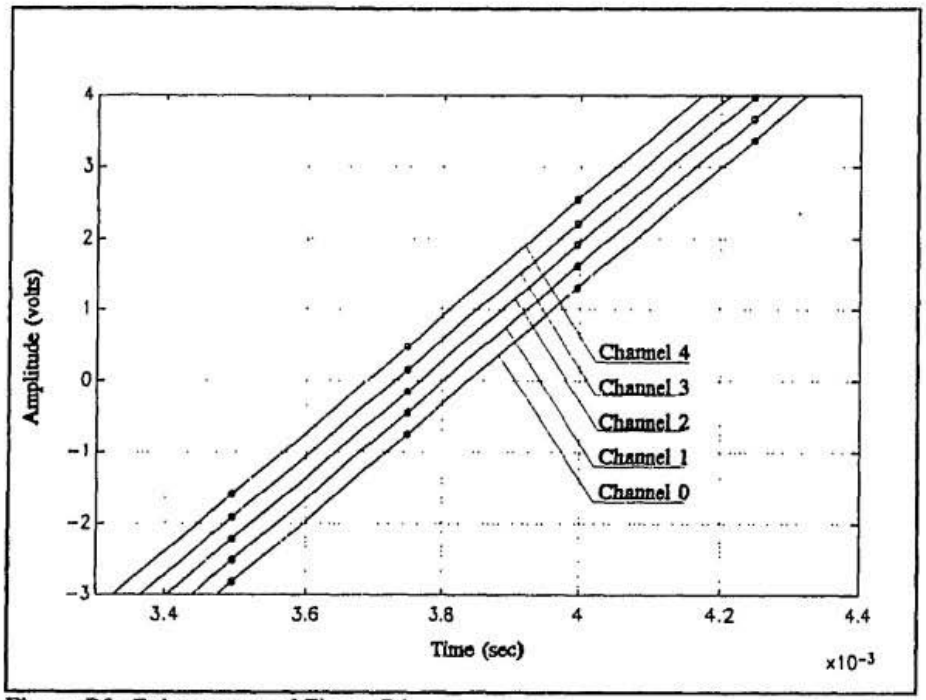

Figure D2: Enlargement of Figure D1.

Then the time delay between adjacent channels can be determined as:

$$Td[i]=\frac{V_{diff}[i]}{S_{ref}} \qquad \text{(D3)}$$

where i = 1, 2, 3, 4

From which the time delay between channel 0 and 1, Ch0 and Ch2, Ch0 and 3, etc.. can be evaluated.

Figure D3 illustrates the adjacent channel acquisition rate of the Keithley 575 data acquisition system $Td_{avg} \approx 36.43us => \approx 27450.0Hz$. Towards

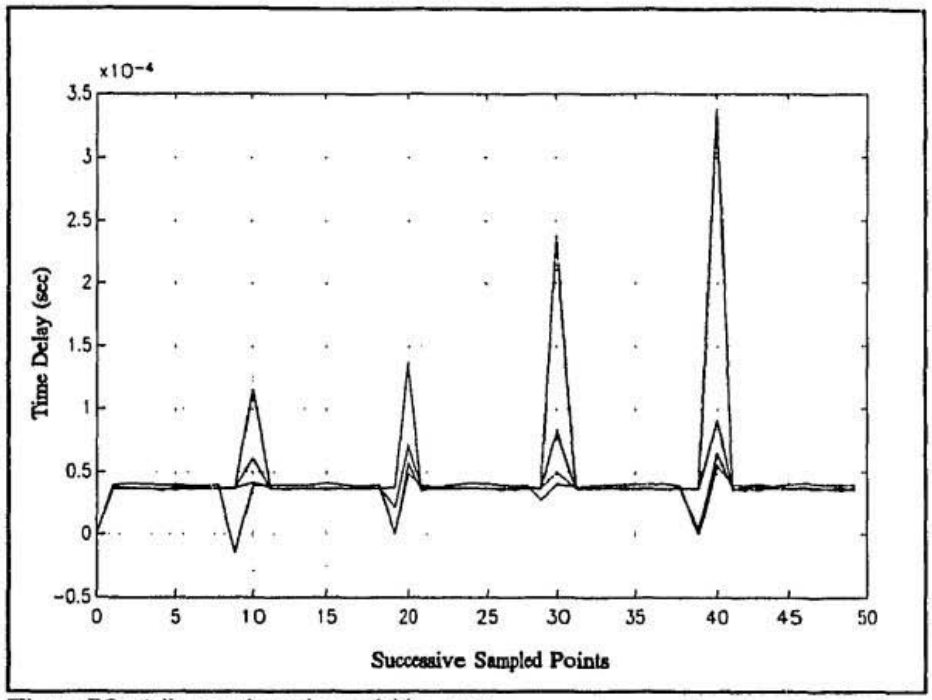

Figure D3: Adjacent channel acquisition rate.

the negative and positive peaks of the reference signal note the inability of the sampling rate, 4004Hz, to capture the high frequency components. In Figure D3 the triangular peaks are a result of under sampling. These peaks correspond to the reference signal's peaks of Figure D1.

D.2 Sampling Rate

The *Channel Sampling Rate* is essentially the time interval at which the feedback control system operates - Δt. A *Control Interrupt* vector is generated based upon this set sampling rate(1602Hz) and initiates a single acquisition cycle. This sampling rate is critical and chosen such that interrupt vectors do not overlap each other during both the five channel sampling sequence and control software execution. If violated the interrupts will overlap, halt the software execution and may cause

irrevokable dammage to the robot. Optimizing interrupt vector generation is based upon evaluating the time duration of each feedback control blocks. These times are summarized in table II of Section 3.4.2. Since we are conducting an experiment, the *Channel Sampling Rate* being used is 4004Hz. This increases the experiment resolution, hence the accuracy.

In summary, the *Channel Sampling Rate* is known prior to conducting the experiment.

D.3 Channel Time Rate of Change

Evaluating the instantaneous time rate of change, S_{inst}, for each of the five sensor inputs is based upon adjacent sample information of the same channel. Equation D4 describes the operation:

$$S_{inst}[i]=\frac{Ch[i](t)-Ch[i](t-\Delta t)}{\Delta t} \qquad \text{(D4)}$$

where i = 0,1,2,3,4

Therefore, instantaneous slopes for the individual channels are determined based upon the signal sampling frequency and successive channel samples.

D.4 Results

Mathematically, channel signal reconstruction is described by:

$$Ch_{reconstruct}[i]=Ch[i]-S_{inst}[i]*\sum_{1}^{n-i} T_d[n] \qquad \text{(D5)}$$

where i = 1,2,3,4

Figure D4 illustrates the channel reconstruction results and Figure 5D emphasises the methods accuracy. At the positive and negative peaks of the reconstructed signal, the reconstruction deteriorates due to the high frequency components. Dominant frequencies generated in the sensor signals during the actual robot arm are at least 10 times less than the sampling rate used (1602Hz). Therefore, aliasing effects are negligible.

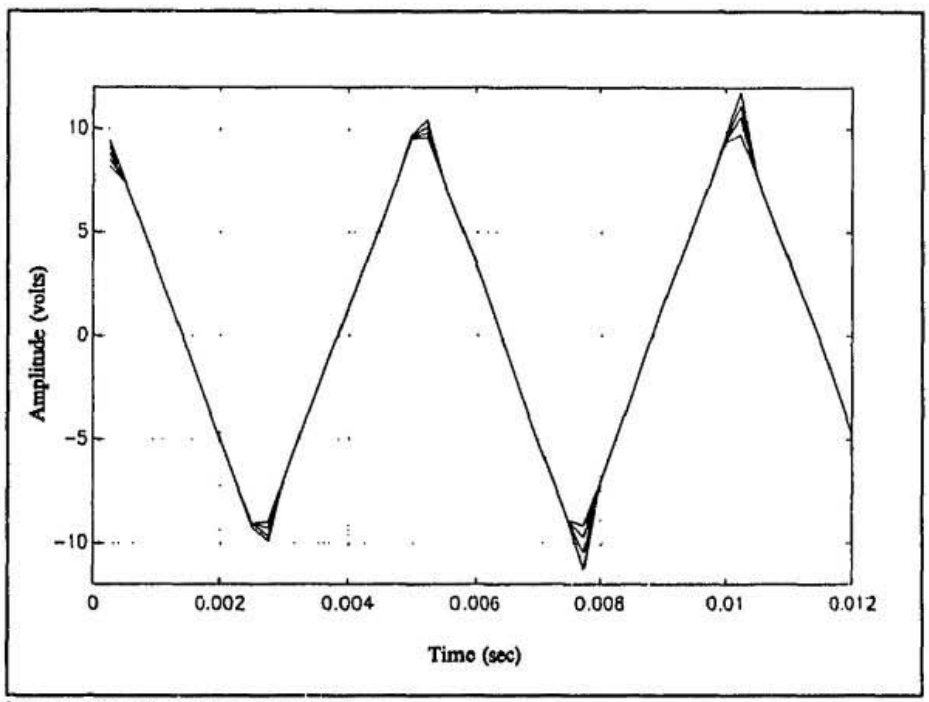

Figure D4: Channel reconstruction.

In summary, the instantaneous slope for each channel signal is determined based upon the current sample, its previous sample and the sampling rate. Because the time delay associated with channel selection and A/D conversion is known, referencing channels 1 through 5 to channel 0 is accomplished by multiplying the total time delay for each channel, with respect to channel 0, by its instantaneous slope and subtracting the result form the current sample.

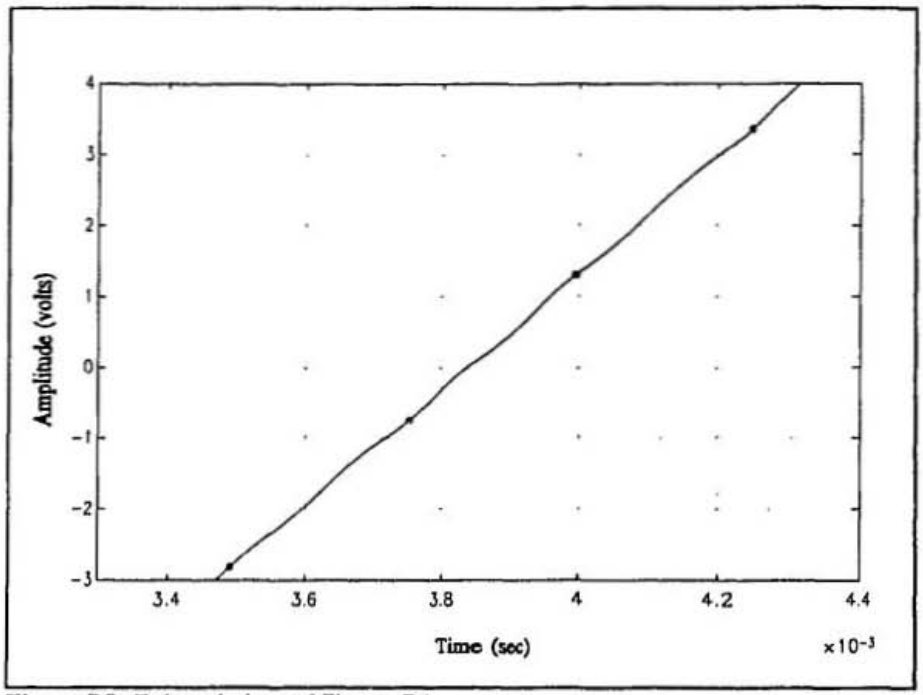

Figure D5: Enlarged view of Figure D4.